REPORT DOCUMENTATION PAGE

Form Approved
OMB No. 0704-0188

1. AGENCY USE ONLY (Leave blank)	2. REPORT DATE	3. REPORT TYPE AND DATES COVERED
	7.Jan.99	DISSERTATION

4. TITLE AND SUBTITLE
PERFORMANCE ANALYSIS OF A MULTISTATIC COHERENT DOPPLER LIDAR

5. FUNDING NUMBERS

6. AUTHOR(S)
CAPT MAGEE ERIC P

7. PERFORMING ORGANIZATION NAME(S) AND ADDRESS(ES)
PENNSLYVANIA STATE UNIVERSITY

8. PERFORMING ORGANIZATION REPORT NUMBER

9. SPONSORING/MONITORING AGENCY NAME(S) AND ADDRESS(ES)
THE DEPARTMENT OF THE AIR FORCE
AFIT/CIA, BLDG 125
2950 P STREET
WPAFB OH 45433

10. SPONSORING/MONITORING AGENCY REPORT NUMBER

FY99-24

11. SUPPLEMENTARY NOTES

12a. DISTRIBUTION AVAILABILITY STATEMENT
Unlimited distribution
In Accordance With AFI 35-205/AFIT Sup 1

12b. DISTRIBUTION CODE

13. ABSTRACT (Maximum 200 words)

14. SUBJECT TERMS

15. NUMBER OF PAGES
154

16. PRICE CODE

17. SECURITY CLASSIFICATION OF REPORT	18. SECURITY CLASSIFICATION OF THIS PAGE	19. SECURITY CLASSIFICATION OF ABSTRACT	20. LIMITATION OF ABSTRACT

The Pennsylvania State University

The Graduate School

Department of Electrical Engineering

PERFORMANCE ANALYSIS OF A MULTISTATIC

COHERENT DOPPLER LIDAR

A Thesis in

Electrical Engineering

by

Eric Parker Magee

Submitted in Partial Fulfillment
of the Requirements
for the Degree of

Doctor of Philosophy

August 1998

We approve the thesis of Eric Parker Magee.

Date of Signature

Timothy J. Kane
Assistant Professor of Electrical Engineering
Thesis Advisor; Chair of Committee

14 July 1998

Christopher S. Ruf
Associate Professor of Electrical Engineering

6/22/98

C. Russell Philbrick
Professor of Electrical Engineering

7/14/98
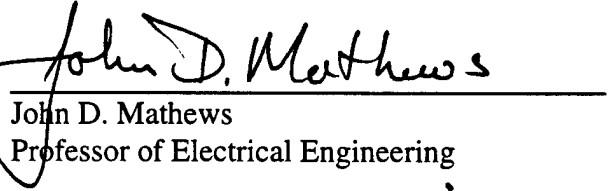
John D. Mathews
Professor of Electrical Engineering

6/22/98
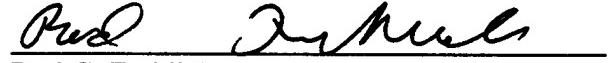
Rod G. Frehlich
Adjunct Professor of Electrical Engineering

6/22/98

Dennis W. Thomson
Professor of Meteorology
Head of the Department of Meteorology

3.7.98
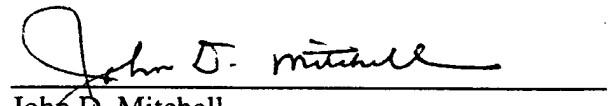
John D. Mitchell
Professor of Electrical Engineering
Interim Head of the Department of
    Electrical Engineering

7/14/98

ABSTRACT

Wind velocity can be obtained using a light detection and ranging (lidar) system by measuring the Doppler shift of the scattered return from aerosols and particulates in the atmosphere. Doppler lidar systems for wind velocity measurements can be classified into two categories, coherent detection and direct (or incoherent) detection. Under each category there are novel approaches to measuring the return signal frequency. Regardless of the measurement mode, the goal for both types is to measure the frequency difference between the transmitted laser pulse and the scattered signal. This frequency shift is proportional to the velocity of the scatterers. How accurately these systems can measure the frequency shift, and thus the velocity, is dependent upon the system characteristics. Existing Doppler lidar systems employ monostatic configurations which require scanning a volume to obtain wind velocity and direction. Range resolution in these systems is normally obtained by using a pulsed laser system. This places a fundamental limit on the range-velocity resolution product.

The purpose of this research is to investigate the feasibility of utilizing a multistatic configuration for measuring 3-dimensional vector winds. In the multistatic configuration, horizontal and vertical resolution are determined by the telescope field-of-view, laser divergence, and baseline separation distance between the laser and the telescope. This enables the use of a continuous-wave (CW) or long pulse laser transmitter (narrow spectral width) and eliminates the dependence between range and velocity resolution.

The results of this research show that a multistatic pulsed Doppler lidar system will provide estimates of wind velocity with errors less than 1 m/sec and spatial resolution between 10 and 100 cm^3 within the atmospheric boundary layer. Detailed signal-to-noise ratio calculations indicate that small transmit and local oscillator beams actually improve system performance. Therefore, a compact transmitter and receiver design can be used. The spatial resolution achievable with this multistatic system is better than previous lidar systems, yielding fine scale measurements of velocity fields.

TABLE OF CONTENTS

LIST OF FIGURES

LIST OF TABLES

ACKNOWLEDGMENTS

I would like to take this opportunity to say thank you first to my wife, Caryn, for her understanding and tolerance during my quest for a Ph.D. Without her love and support this thesis would not have been possible. I would also like to apologize to my daughter, Paige, for the times that I missed spending with her. I promise I will make it up to you. To my parents, a heartfelt thanks for instilling in me the belief that all things are possible if you apply yourself.

I would also like to thank my thesis committee for their guidance. Dr. Mathews, thank you for questioning my results and for making me "convince" you. Those discussion improved my understanding of the problem immensely. Dr. Frehlich, thank you for the long telephone discussions and for the two weeks you took me under your wing in Boulder. I would still be working on the SNR calculations if it were not for your help. And of course, Dr. Kane, your guidance and encouragement were essential to the completion of this project. I would also like to mention that the idea for this project came from Dr. Kane, and for that, I am grateful. My thanks also to Andy Gerrard, Dean Houck, Brent Grime and Dan Rafferty for helping me put it all together.

Lastly, I would like to thank the United States Air Force for giving me the opportunity to achieve this goal.

Chapter 1

INTRODUCTION

1.1 Doppler Lidar

One of the first applications of laser-Doppler velocimetry (LDV) was incorporated

by a group from Marshall Space Flight Center (NASA) in the late 1960's. NASA used

the technique for wind tunnel and jet-type flow studies [1]. Wind velocity can be

estimated by measuring the Doppler frequency shift, relative to the carrier frequency,

undergone by laser radiation scattered by particles suspended in the flow. This frequency

shift can be measured using either a coherent (heterodyne) or an incoherent (direct)

detection scheme. For a 1-dimensional coaxial system, the return signal is Doppler

shifted by an amount proportional to the velocity of the aerosols along the line of sight of

the transmitter. For sensing 3-dimensional vector winds, measurements from at least

three different directions are required. Typically for the monostatic case, a technique

called velocity azimuth display lidar or VAD is used to obtain the vector wind [2, 3].

This technique has to sacrifice spatial and temporal resolution in order to measure the

horizontal velocity. In effect, the horizontal velocity is averaged over a cross sectional

area on the order of 0.1 km^2 for a 1 km altitude and a 20 degree cone angle. To obtain

range resolution, most monostatic lidar systems use a pulsed laser. This imposes a fundamental limit for the range-velocity resolution product [3, 4].

1.2 Objectives

The spatial resolution, range resolution, and velocity resolution limitations can be addressed by implementing a bistatic configuration with a relatively long pulse or continuous-wave (CW) laser transmitter. In this configuration, the spectral width of the laser is narrow compared to a short pulse system, which results in improved velocity resolution without sacrificing range resolution. In a bistatic configuration the measured Doppler shift is proportional to the component of velocity along the bisector of the bistatic angle. The 3-dimensional velocity vector can be determined using a multistatic (multiple receivers) configuration. Knowledge of the 3-dimensional winds within a small volume can be useful in a number of research areas, such as aviation, weather prediction, meteorological modeling, and severe weather detection.

The main thrust of this research is to provide a theoretical basis for the design and implementation of a multistatic Doppler lidar system for measurement of 3-dimesional vector winds within the atmospheric boundary layer. Wind profiling within the boundary layer can be used to obtain estimates of the vertical diffusivity as a function of height and time [5]. With a multistatic system, high spatial resolution can be obtained with relatively long pulses or CW lasers because the scattering volume is defined by the overlap of the transmitter and receiver fields of view. This fine scale resolution can be

used to locate shear layers and localized wind turbulence that may have been spatially averaged in previous systems.

In this thesis, the general expressions for the predicted performance of a multistatic coherent Doppler lidar system are derived. A measurement model is presented that relates the Doppler shift of a scattered signal at each detector to the 3-dimensional velocity vector of the aerosols within the scattering volume. From this model, the velocity vector can be obtained by inverting the system of linear equations. The errors induced by this inversion are related to the specific geometry through a matrix that maps the 3-dimesional velocity to N-dimensional measured Doppler shifts, where N is the number of detectors.

This thesis also presents predicted results for estimating the Doppler shift from the scattered signal. The lower bound on the estimation errors is presented for the statistical model of the return signal. This lower bound is related to the transmitted pulse temporal profile and the ratio of the expected value of the return signal power to the average noise power, or signal-to-noise ratio (SNR). Derivation of the general expressions for SNR, including refractive turbulence effects, is also accomplished.

The general expressions are applied to three specific geometries and typical lidar system parameters. The three geometries examined are shown in *Figure 1-1*, *Figure 1-2*, and *Figure 1-3*. Case 1 is a multistatic system with a transmitter and three receivers. In this configuration, the receivers are located on a circle with radius equal to the baseline separation. The receivers and the transmitter can be scanned to probed a specific volume in space; however, the analysis for Case 1 assumes that the transmitter is always pointed
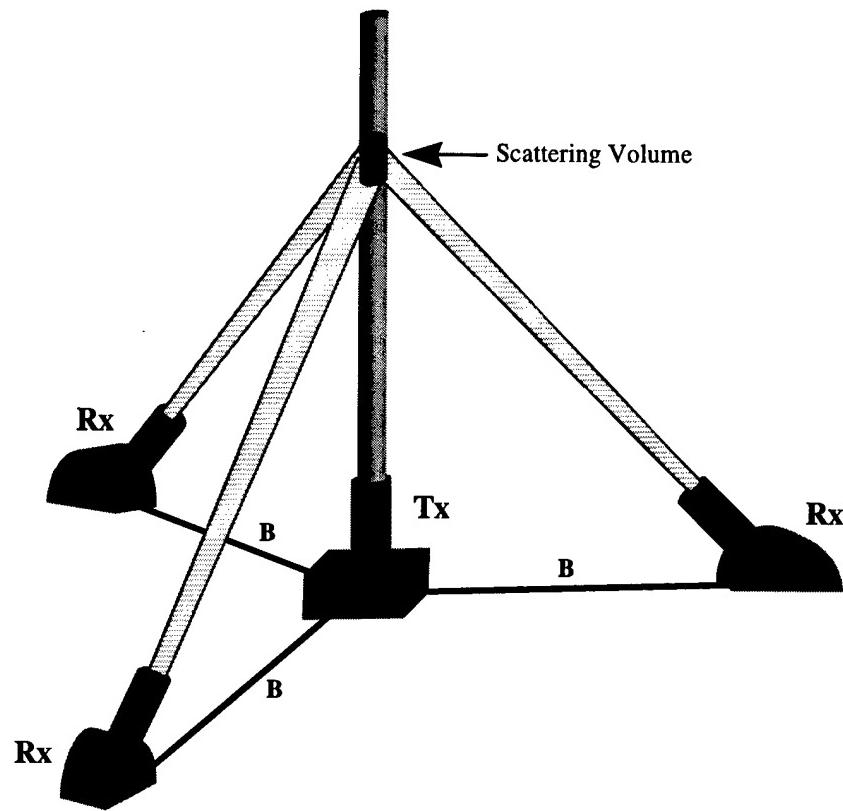
Figure 1-1: Case 1 configuration. A single transmitter (Tx) located in the center with three receivers (Rx). B is the baseline separation.
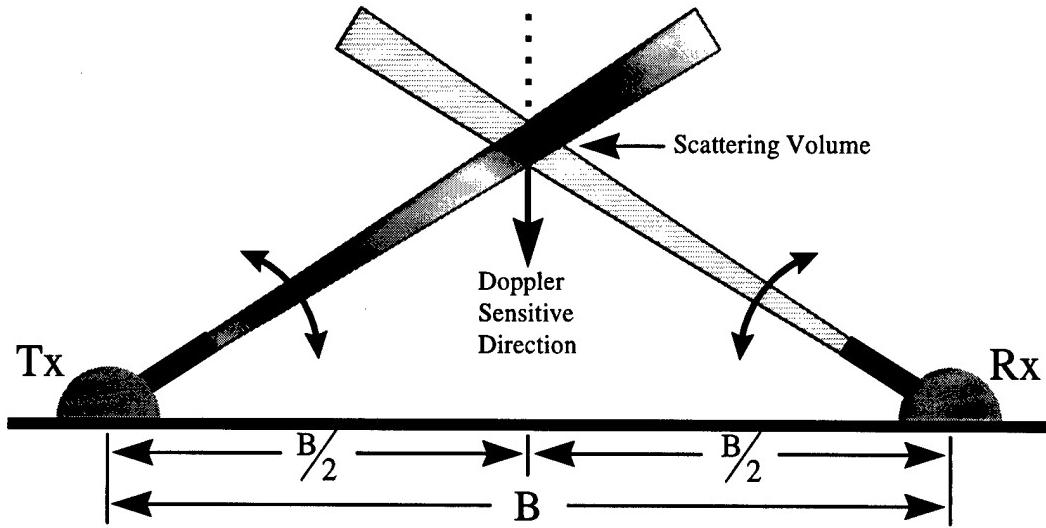
Figure 1-2: Case 2 configuration. Single transmitter (Tx) and single receiver (Rx) scanned along bisector of the baseline (B).
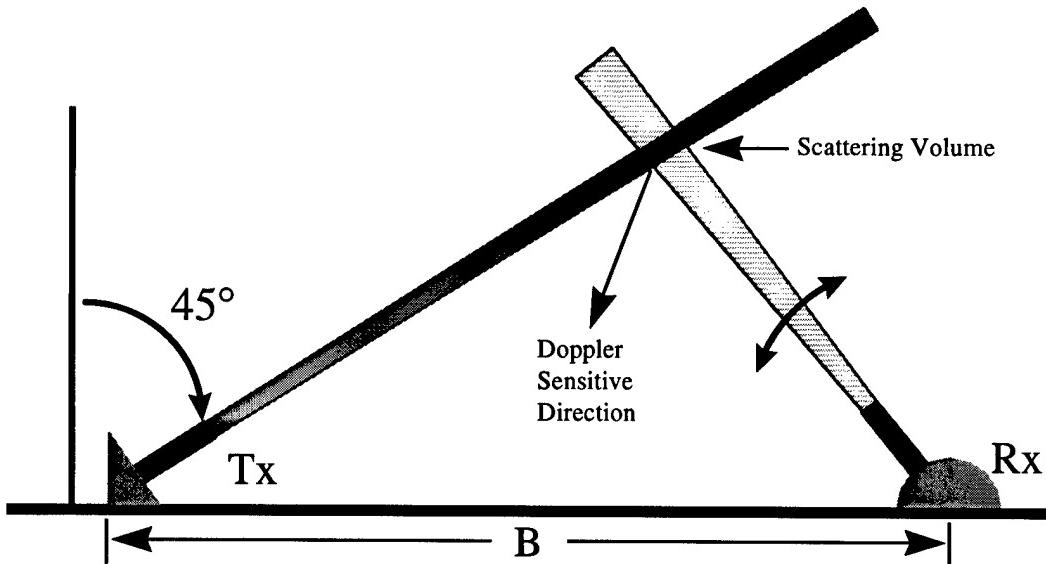
Figure 1-3: Case 3 configuration. Single transmitter (Tx) pointed at 45 degrees and a single receiver (Rx) scanned along the Tx beam.

vertically. As can be seen from the figure, the scattering plane will be different for each transmitter/receiver pair. This implies that the polarization with respect to the scattering plane will be different for each pair. One way to remedy this problem is to transmit circular polarization so there is always a component of polarization parallel and perpendicular to the scattering plane. For this case it is assumed that the transmit beam is circularly polarized and the SNR is evaluated for each polarization state.

Case 2 is a bistatic system that could be used to sense the vertical velocity along the bisector of the baseline separation. For this case, the scattering plane is fixed and either polarization can be used. For completeness, the SNR is evaluated for both polarization states. The geometry of Case 3 is included as a means of evaluating performance when the propagation directions are near horizontal, where effects of refractive turbulence are increased.

Implementation of a multistatic system (lidar or radar) presents many additional challenges over the conventional monostatic systems. These complexities arise, for the most part, from the geometry [6]. Challenges include, but are not limited to, frequency and timing synchronization, alignment, and expense [7, 8]. Other issues of concern are calibration, and refractive turbulence effects, especially for coherent detection.

The results of this research show that a multistatic pulsed Doppler lidar system will provide accurate estimates of particle velocity within the atmospheric boundary layer with high spatial resolution. Detailed signal-to-noise ratio calculations indicate that small transmit and local oscillator beams actually improve system performance. Therefore, a compact transmitter and receiver design can be used. The spatial resolution achievable

with this multistatic system is better than previous lidar systems (on the order of 10–100

cm^3), yielding fine scale measurements of velocity fields.

1.3 Thesis Organization

In Chapter 2, a brief description of past work in the area of Doppler lidar is given.

The first section gives an overview of past bistatic radar and lidar systems. The next

section reviews coherent lidar systems, including continuous wave and pulsed systems.

The last section in Chapter 2 discusses incoherent Doppler lidar systems.

Chapter 3 gives the basic theory for the performance of a bistatic coherent lidar

system. The first issue that is addressed in this chapter is the geometry. A measurement

model is developed to describe the relationship between the Doppler shift measured at

each detector and the actual wind velocity. Unless the velocity measurements are made

along three orthogonal directions, there will be error amplification introduced in the

inversion [9]. Once the measurement model for the relationship between the wind

velocity and the measured Doppler shifts is determined, the estimation errors due to the

randomness of the return signal are addressed. Regardless of how the return signal is

detected, the Doppler shift needs to be estimated from the measured signal. The

performance of the estimate is evaluated in terms of the Cramér-Rao lower bound. This

is a bound on the minimum variance of the estimation error for an unbiased estimator.

This error bound, together with the errors introduced by the geometry, will define the

lower performance bound of the velocity estimates. With the estimation errors taken into account, the next step is to calculate the signal-to-noise ratio.

After the theoretical expressions are developed in Chapter 3, they are applied to specific problems in Chapter 4. Three specific geometries are considered. The SNR is calculated for each geometry under different system conditions. The SNR expression for the monostatic limit is compared to expressions derived in previous work for verification. The effects of refractive turbulence are also addressed in this chapter. Then the detection and estimation performance is characterized for each case. The thesis is summarized in Chapter 5 with some comments and conclusions as well as recommendations for future research.

Chapter 2

BACKGROUND

In this chapter, a brief outline of past work in the area of Doppler lidar is presented. The first section highlights past bistatic radar and lidar systems. The next section reviews coherent lidar systems, including continuous wave and pulsed systems. The second section also gives an outline of the detection and estimation problem inherent in Doppler radar and lidar systems. The last section includes a brief discussion incoherent Doppler lidar system for completeness. Compared to incoherent detection, coherent detection lidar has the advantage of greater sensitivity at middle and infrared wavelengths [10]. The incoherent detection case for the multistatic system proposed is not addressed in this thesis.

2.1 Bistatic Radar/Lidar

Early radar systems in the United States and the United Kingdom were bistatic configurations, the earliest of which appears to be in 1937 by British Post Office engineers [7]. The use of Bistatic radar systems discontinued with the invention of the duplexer at the U.S. Naval Research Laboratory in 1936, providing a means for a shared transmit and receive antenna (monostatic) [11]. Since then, the majority of lidar systems have implemented monostatic configurations [12].

A multistatic configuration using a laser and the Doppler effect for measuring flow velocity was reported by Huffaker in 1970 [13]. This system utilized forward scatter of the laser radiation to three detectors spaced evenly in a cone-like configuration. Other bistatic lidar systems to obtain physical characteristics of aerosols are reported by Reagan and Herman [14], Menzies *et al.* [15], Parameswaran *et al.* [16], Devara and Raj [17, 18], and Stevens [12]. These systems were used for measuring aerosol scattering and concentration profiles. Bistatic imaging lidar systems are reported by Welsh and Gardner for profiling sodium densities at about 90 km [19] and Meki *et al.* for lower altitude aerosol properties [20]. A tristatic system using incoherent detection was investigated by Abreu *et al.* [5] but does not appear to have been implemented. This configuration utilized two transmitters and a single receiver to measure horizontal and vertical velocities.

2.2 Coherent Lidar

Coherent detection of Doppler lidar returns is the primary method of measuring the frequency offset incurred by the transmitted laser pulse due to the velocity of the scattering particles. Coherent Doppler lidar has several similarities to Doppler radar, particularly with regard to signal processing after down conversion. Most of the processing techniques used in Doppler lidar are adapted from those developed for Doppler radar. There is, however, one fundamental difference between Doppler lidar and Doppler radar signal processing. Radar systems measure the Doppler shift by observing

the phase of a signal over a sequence of pulses. Lidar systems measure Doppler shift from a single pulse [21]. For an excellent overview and history of coherent Doppler lidar systems, the reader is referred to a paper by Bilbro [22].

In heterodyne (or coherent) detection, the frequency shift of the return signal relative to the transmitted frequency is measured by mixing the return signal with a "single frequency" local oscillator (LO). The resulting signal will have a sinusoidal variation at the intermediate frequency, the frequency difference between the LO and the return signal. It is this frequency that is measured to get the velocity. Because a coherent receiver is sensitive to spatial phase distortions, a near diffraction limited receiver telescope is required. This fact will also limit the maximum size of the receiver telescope (due to atmospheric effects).

There have been several techniques used to characterize the effects of refractive turbulence on wave propagation and coherent lidar performance. They include, but are not limited to: Rytov theory [23], the extended Huygens-Fresnel theory [24-28]; the phase-only approximation of the extended Huygens-Fresnel theory [29, 30]; and the phase cancellation limit of the extended Huygens-Fresnel theory, which considers the log-amplitude scintillation as the dominant mechanism [31]. These theories are only valid for weak path-integrated refractive turbulence and have not been shown to be valid for general refractive turbulence.

Frehlich and Kavaya [32, 33] derive general expressions for the effects of refractive turbulence for a monostatic system using the path integral formulation (Fresnel

approximation) which is valid for any typical path integrated refractive turbulence. It is this path integral representation (applied to a multistatic system) that is used in this thesis.

2.2.1 Continuous-wave

The earliest Doppler lidar systems used to detect air motion from atmospheric backscatter were continuous-wave CW systems [1, 34]. In a monostatic CW lidar system range resolution is generally obtained by focusing. The range resolution achievable is roughly proportional to the inverse square of the beam diameter [21, 35]. Thus to improve spatial resolution at long ranges, a large telescope is required. In order to scan a focused CW system, the focal length of the optics must be varied, which increases the system complexity. A continuous-wave laser can be used in a bistatic configuration because the range resolution is obtained by the overlap between the transmitter divergence and the telescope field-of-view. This will inherently reduce the spectral content of the laser output and in turn, increase the velocity resolution.

CW lidar systems using coherent detection and aerosol backscatter have been very important to remote sensing. Applications include measurements of radial or line-of-sight (LOS) wind velocity, true airspeed of aircraft, transverse wind velocity, and atmospheric backscatter coefficients [22]. Churnside and Yura [36] investigated a CW system which utilizes a detector array, coherent detection, and the spatiotemporal correlation function of the signal currents from the heterodyne detector pairs. They show

that the time derivative of this function at zero lag is directly proportional to the velocity component parallel to the spatial separation of the detector pair.

2.2.2 Pulsed

Pulsed coherent Doppler lidar systems were developed in the early 1970's [21]. As mentioned in the introduction, the majority of monostatic lidar systems use a pulsed laser to obtain range resolution. In a pulsed system the range resolution is obtained from the finite time duration of the pulse. The range resolution for a pulsed monostatic system is $c\tau_p/2$, where c (m·sec^{-1}) is the speed of light and τ_p (sec) is the pulse length or length of sampling interval. The pulse length can be shortened to increase the range resolution; however, the resulting increase in signal bandwidth will degrade the velocity resolution of the system [21]. This phenomena can be characterized by the following: the minimum range resolution is given by $\Delta R = c\tau_p/2$ (m), and the corresponding spectral resolution Δf (Hz) is approximately $1/\tau_p$. The velocity resolution for a monostatic system is related to the frequency resolution by $\Delta v = \lambda \Delta f/2 = \lambda/2\tau_p$ (m·sec^{-1}). Therefore, the approximate range-velocity resolution product (m^2·sec^{-1}) is given as [3, 4]

$$\Delta v \Delta R \approx \frac{\lambda c}{4}. \tag{2.1}$$

This equation shows that there is a trade-off between velocity resolution and range resolution. Thus, in a pulsed Doppler system, care must be taken when selecting the pulse duration. It must be long enough to avoid spectral broadening of the signal and loss

of velocity resolution. However, it must be short enough to obtain the desired range resolution. It should be noted that this formulation of the range velocity resolution product is based on the assumption that the frequency resolution is the same as the frequency spread of the return signal.

Because the particles within the scattering volume move with respect to each other, the bandwidth of the optical return signal is broadened. The shape of the backscattered signal power spectrum is proportional to the distribution of small scale radial wind speeds within the scattering volume. The coherence time of the return signal due to wind turbulence is approximated by

$$t_c \approx \frac{\lambda}{\sigma_v} \tag{2.2}$$

where λ (m) is the wavelength and σ_v (m·sec^{-1}) is the standard deviation of the distribution of velocities within the scattering volume [21]. The overall power spectrum of the return signal is the convolution of the power spectrum resulting from the small scale velocities with the power spectrum of the laser transmit pulse. There may be other contributors to the spectral broadening of the return pulse which are also convoluted with the power spectra due to the effects mentioned above. If all broadening mechanisms are assumed to result in Gaussian power spectra (for simplicity), the resulting power spectrum is Gaussian with a variance equal to the sum of variances from each contributing factor.

2.2.3 Spectral Estimation

An estimate of the mean frequency of the return signal can be obtained with one of several methods. Most signal processing methods used in Doppler lidar systems are based on algorithms designed for Doppler radar systems. Estimation algorithms can be classified into two categories, parametric and nonparametric. Nonparametric methods obtain estimates directly from the data, via the complex correlogram or the periodogram. Parametric methods fit a specified model to the data and estimate parameters from the model coefficients [37, 38]. Typical models are the autoregressive (AR), the moving average (MA), or the autoregressive moving average (ARMA). Incoherent addition (or accumulation) of the periodogram, correlogram, or model coefficients can improve parameter estimates [39, 40]. This does not give the same results as averaging independent estimates from separate returns [39]. A summary of different estimation schemes is shown in *Figure 2-1*.

An important parameter used to gauge the performance of an estimator is the Cramér-Rao lower bound (CRLB) [41, 42]. The CRLB is the minimum variance of the estimation error for an ideal unbiased estimator. Maximum likelihood (ML) estimators are a class of estimators that achieve the minimum variance for a large number of samples. The ML estimates become quite complex if there is no apriori information about the statistics of the return signal and therefore may be impractical.
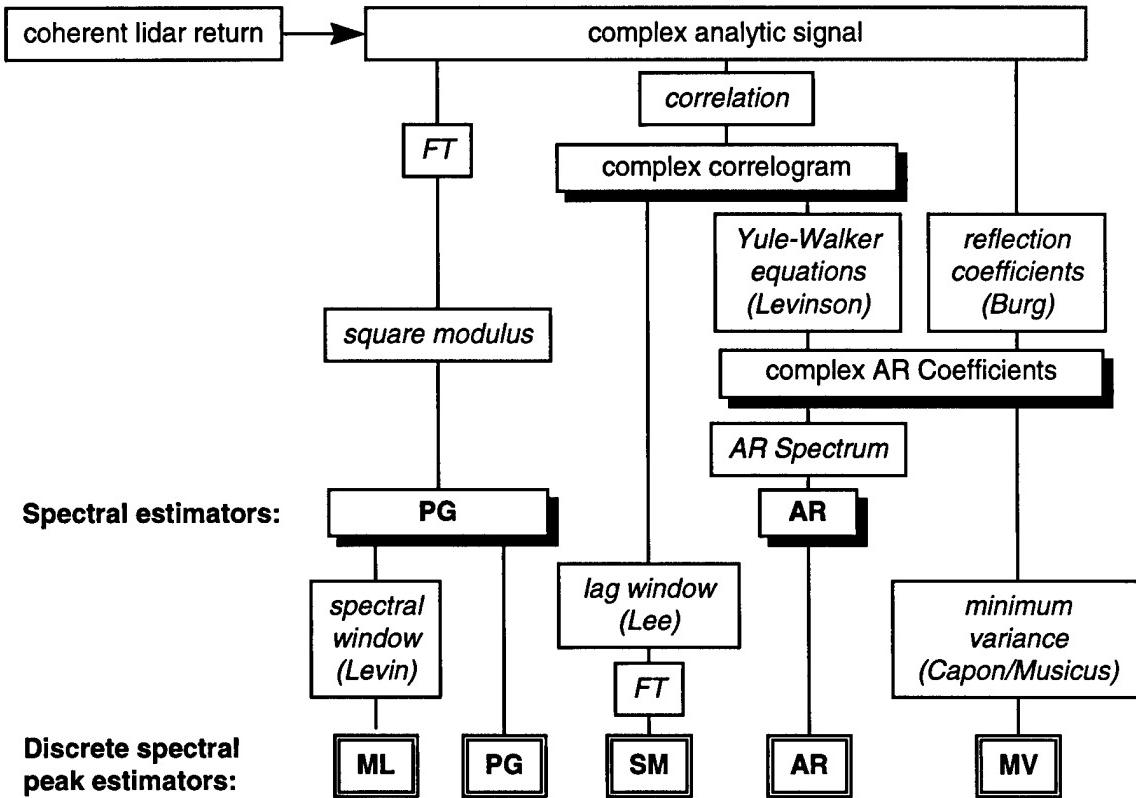
Figure 2-1: Flow chart showing methods for obtaining the discrete spectral peak estimates, divided into periodogram-based and correlogram-based techniques. Algorithms, together in some cases with their authors, are in italics. Shadowed boxes indicate where incoherent accumulation can take place. Notation: FT, Fourier transform; AR, autoregressive; PG, periodogram; ML, maximum likelihood; SM, signal matching; MV, minimum variance. Adapted from Rye and Hardesty [40].

Zrnic [43] gives the coherent Doppler mean frequency estimation approximate CRLB for high SNR as

$$\sigma_f^2 \geq \frac{1}{T_S^2 M} \frac{12(wT_s)^4}{[1-12(wT_s)^2]}, \qquad (2.3)$$

and low SNR as

$$\sigma_f^2 \geq \frac{1}{T_S^2} \frac{4\sqrt{\pi}(wT_S)^3}{M} \frac{N^2}{S^2}, \tag{2.4}$$

where S (W) is the signal power, N (W) is the average noise power per sample, σ_f^2

($\text{m}^2 \cdot \text{sec}^{-2}$) is the variance of the mean frequency estimate, w (Hz) is the spectral width of

the return signal, M is the total number of samples in the range gate, and T_S (sec) is the

sampling interval. Eqs. (2.3) and (2.4) are the asymptotic bounds for σ_f^2.

It has been shown that the high SNR limit of the CRLB given by Eq. (2.3) is a

poor estimate for the true CRLB [39, 44]. The exact CRLB derived by Frehlich [44] is

given as

$$\sigma_f^2 \geq \left[-4\pi^2 T_S^2 \sum_{l=0}^{M-1} \sum_{l=0}^{M-1} (l-k)^2 Q_{kl} \left(\underline{Q}^{-1} \right)_{lk} \right]^{-1}, \tag{2.5}$$

where Q_{kl} are the elements of the covariance matrix $\underline{Q}$, the covariance of $s_k + n_k$, and the

signal model used is given by

$$z_k = s_k \exp\left[j2\pi f k T_s \right] + n_k, \tag{2.6}$$

where s_k and n_k are complex Gaussian random processes, and f (Hz) is the mean

frequency. An example simulation of Doppler lidar signal and periodogram is shown in

Figure 2-2.

The top plot in this figure shows the pulse location as a function of time. The

middle plot of *Figure 2-2* shows the coherent lidar signal. The temporal scale of the

signal envelope corresponds to the time it takes the pulse to travel a distance Δr, after

which time, a new collection of independent atmospheric scatterers are illuminated by the

pulse. The bottom plot in the figure show the periodogram of the lidar signal. Frequency
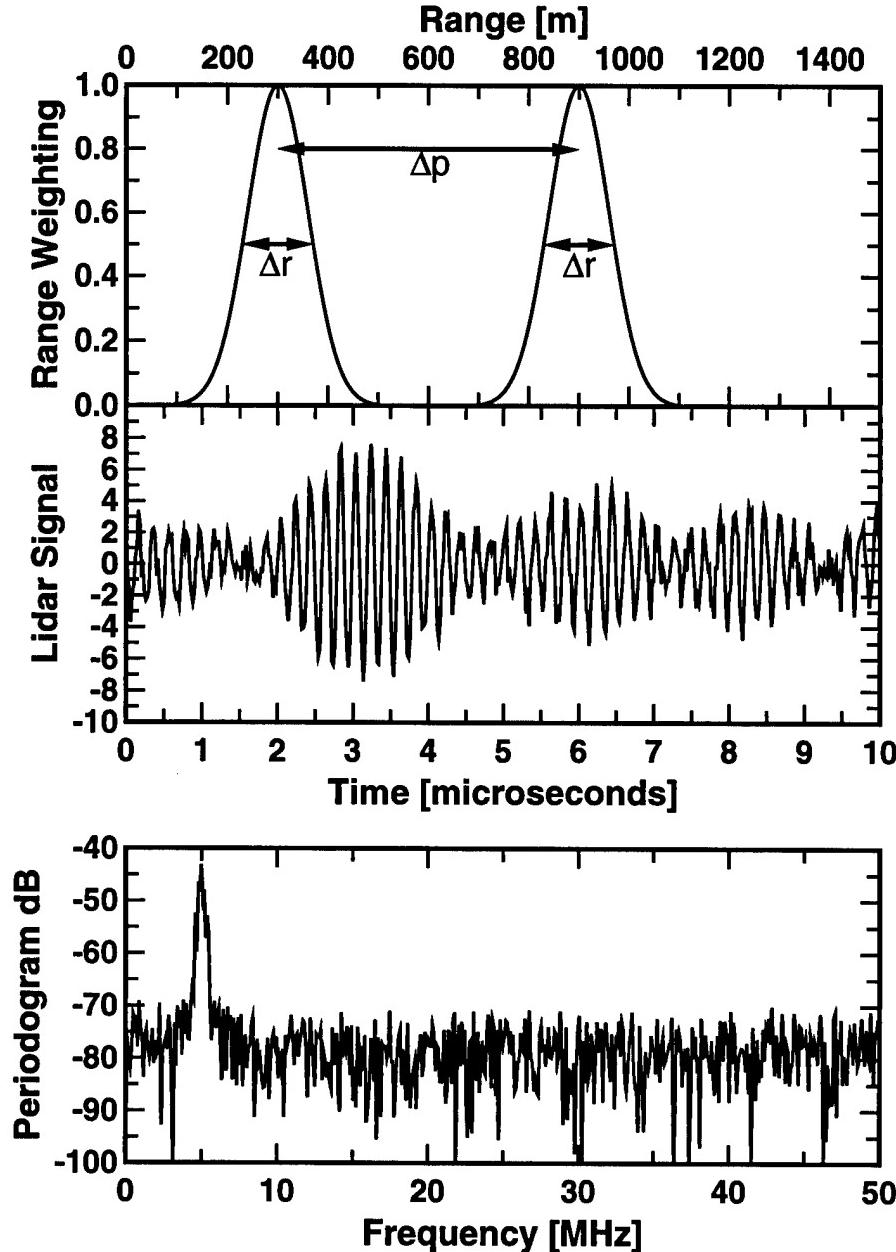
Figure 2-2: Simulation of Doppler lidar data for a 2-μm lidar [45] with a Gaussian pulse, SNR = 10, f = 5 MHz, w = 0.2 MHz, T_S = 20 ns. The pulse is shown at 2 μs and 6 μs. Δr is the FWHM of the sensing volume and Δp is the distance the pulse moves in 4 μs. The correlation time of the lidar signal is about 2 μs. Figure taken from Frehlich [44].

domain estimation of the mean frequency involves extracting the location of the spectral feature of the random periodogram coefficients in the presence of noise.

Typical numbers quoted in the literature for velocity accuracy (as compared to anemometers and balloon sondes) for coherent lidar systems are on the order of 1 m·sec^{-1}. Mayor *et al.* [46] report good agreement between lidar measurements and anemometer measurements. Under high SNR conditions they quote an accuracy of approximately 0.5 m·sec^{-1} and a correlation between anemometer data and lidar data of about 0.9. Köpp *et al.* [47] compare wind velocity measurements made using the velocity azimuth display (VAD) technique to anemometer and balloon sonde measurements. They report an accuracy on the order of 1.3 m·sec^{-1} with a correlation of approximately 0.8. They attribute the lower accuracy to the horizontal inhomogeneity in the wind field. Recall that the VAD technique averages the wind field over a large spatial volume. Single shot ML estimation performance within 30% of the ideal performance (based on simulation) is reported by Frehlich *et al.* [48]. They report standard deviations of 0.4–1.2 m·sec^{-1} for the velocity estimates. They also report systematic errors due to frequency drift of lasers, non-linear amplifiers, digitization errors, etc., of approximately 4 cm·sec^{-1}.

While the research in this thesis does not address the actual implementation of a specific mean frequency estimation algorithm, there has been a significant amount of research conducted in this area. Listed below are some of the references that are useful for the analysis of specific estimation algorithms. They are listed for convenience but have not been applied specifically to this research. Efficient estimators, such as those listed in *Figure 2-1*, include pulse pair (or single-lag autocovariance) [49-52], peak

frequency [53], spectral domain [39, 40, 49, 53-57], and maximum entropy [39, 40, 58].

Implementation of ML estimators has also been investigated [39, 40, 54, 55, 58-61].

2.3 Incoherent Doppler Lidar

Incoherent Doppler lidar systems use some type of filtering scheme to measure the

frequency shift relative to the transmitted laser. This filtering system is made up almost

exclusively of multiple étalon Fabry-Perot interferometers. One variation on the

traditional Fabry-Perot interferometer is called the edge technique [62]. A high resolution

spectral filter with a steep slope is utilized. The frequency of the laser and the filter are

chosen such that the frequency output of the laser is located on the steep slope of the

filter. Because of the steep slope, the filter produces large changes in transmission for a

small change in frequency. Both the laser output and the Doppler shifted return signal are

passed through the filter and the frequency difference between the two signals is

measured. By taking the difference, the frequency shift will be insensitive to both laser

and filter frequency jitter and drift. The error in the line of sight velocity at a given point

on the edge of the filter is given as

$$\varepsilon = \frac{N}{S} \frac{1}{\Theta},\tag{2.7}$$

where S (W) is the average signal power, N (W) is the average noise power, and

Θ (m^{-1}·sec) is the measurement sensitivity, given as

$$\Theta = \frac{1}{v} \frac{\Delta I_N}{I_N},$$

(2.8)

where v (m·sec^{-1}) is the velocity, ΔI_N (A) is the differential normalized signal, and I_N (A) is the normalized signal. Because this technique is insensitive to the laser spectral width (if the slope of the filter cutoff is linear) the pulse width can be decreased to improve the range resolution. Simulated results show vertical resolution on the order of 10 meters, with velocity resolution on the order of 0.5 m/s up to a 5 kilometer range.

Most other incoherent Doppler lidar systems use Fabry-Perot interferometers in a more conventional manner [63-65]. The Fabry-Perot interferometer, in its simplest form, consists of two plane, parallel, highly reflected surfaces separated by some distance. By taking advantage of the dependence of transmission characteristics on spacing, index of refraction, and angle of incidence, a very narrow bandpass filter can be designed [66]. The Doppler shift is determined by comparing the transmitted frequency to the Doppler shifted return frequency. A system reported by The Space Sciences Laboratory at the University of Michigan incorporates a high resolution étalon and a multi-ring anode detector to spatially scan the interference pattern generated [67-71].

Chapter 3

THEORY

In this chapter, the general expressions used in the analysis of a multistatic Doppler lidar system are derived. In the first section, the specific geometry and coordinate systems used throughout the thesis are defined. This section is important because the added complexity in a multistatic system is due primarily to the geometry. With coordinate systems established, a measurement model is derived for the relationship between the measured Doppler shift and the wind velocity vector. As shown in this section, the geometry can amplify the errors in estimating the Doppler shift. In Section 3.3, the errors associated with estimating the Doppler shift from the measured signal are addressed. With this estimation error and the error multiplication from the geometry, the overall accuracy of the velocity estimation can be determined. It is shown that the estimation error is related to the signal-to-noise ratio, which is addressed in Section 3.4. General expressions for the SNR in the detector, receiver and target plane are given for a point scatterer as well as a distributed aerosol target. In the next section, the SNR is given for an infinite uniform detector. In Section 3.6, the effects of refractive turbulence are examined.

3.1 Geometry

In this section the geometry used throughout the thesis is defined. The coordinate system used to locate the receiver, transmitter, and target is a fixed system centered at the transmitter. The z-axis of this coordinate system is in the vertical direction. The fixed coordinate system is also used to define pointing directions of the transmit and receive optics. The north referenced coordinate system [6, 7] is centered at the transmitter with its x-z plane in the scattering, or bistatic, plane. There will be a separate north referenced coordinate system associated with each transmitter/receiver pair. Transmitter and receiver referenced coordinate systems are also used. The orientation of the transmitter referenced coordinate system is determined by rotating the north referenced coordinate system so the z-axis is pointed at the target. The orientation of the receiver referenced coordinate system is determined by translating the north referenced coordinate system to the receiver and rotating the axes until the z-axis is pointed at the target. The target referenced coordinate system is the transmitter referenced coordinate system translated to the target and is used for performing target plane integrals. The coordinate systems used are summarized below.

(x, y, z)	$\Rightarrow$	Fixed coordinate system centered at transmitter
(x_n, y_n, z_n)	$\Rightarrow$	North referenced coordinate system
(x_t, y_t, z_t)	$\Rightarrow$	Transmitter referenced coordinate system
(x', y', z')	$\Rightarrow$	Fixed coordinate system centered at receiver
(x_r, y_r, z_r)	$\Rightarrow$	Receiver referenced coordinate system
(x_p, y_p, z_p)	$\Rightarrow$	Target referenced coordinate system.

Figure 3-1 shows the bistatic lidar geometry for an arbitrary receiver. The transmitter is located at the origin of the fixed coordinate system. Likewise, the receiver and target are located at the origins of their respective coordinate systems. The receiver and transmitter are separated by the baseline, $B = \sqrt{b_x^2 + b_y^2 + b_z^2}$ (m), where b_x, b_y, and b_z, are the coordinates of the receiver with respect to the fixed coordinate system. The center of the target is located at a point (p_x, p_y, p_z) with respect to the fixed coordinate system. Using *Figure 3-1*, the relationships between north referenced coordinates and the other coordinate systems can be derived [see ref. 72, pg. 160].

$$
\begin{bmatrix} x_t \\ y_t \\ z_t \end{bmatrix} = \begin{bmatrix} \cos\theta_{nt} & 0 & -\sin\theta_{nt} \\ 0 & 1 & 0 \\ \sin\theta_{nt} & 0 & \cos\theta_{nt} \end{bmatrix} \begin{bmatrix} x_n \\ y_n \\ z_n \end{bmatrix}
$$

$$
\begin{bmatrix} x_r \\ y_r \\ z_r \end{bmatrix} = \begin{bmatrix} \cos\theta_{nr} & 0 & -\sin\theta_{nr} \\ 0 & 1 & 0 \\ \sin\theta_{nr} & 0 & \cos\theta_{nr} \end{bmatrix} \begin{bmatrix} x_n - B \\ y_n \\ z_n \end{bmatrix}
$$

$$
\begin{bmatrix} x_p \\ y_p \\ z_p \end{bmatrix} = \begin{bmatrix} \cos\phi_t\cos\theta_t & \sin\phi_t\cos\theta_t & \sin\theta_t \\ -\sin\phi_t & \cos\phi_t & 0 \\ \cos\phi_t\sin\theta_t & \sin\phi_t\sin\theta_t & \cos\theta_t \end{bmatrix} \begin{bmatrix} x \\ y \\ z \end{bmatrix} - \begin{bmatrix} 0 \\ 0 \\ R_T \end{bmatrix} = \begin{bmatrix} x_t \\ y_t \\ z_t - R_T \end{bmatrix} \tag{3.1}
$$

where θ_{nt} and θ_{nr} are, respectively, the transmitter and receiver look angles with respect to the north referenced coordinate system, which are positive when measured clockwise from z_n, and

$$
\sin\theta_{nr} = \frac{R_T^2 - (B^2 + R_R^2)}{2BR_R}, \qquad \sin\theta_{nt} = \frac{(B^2 + R_T^2) - R_R^2}{2BR_T}. \tag{3.2}
$$
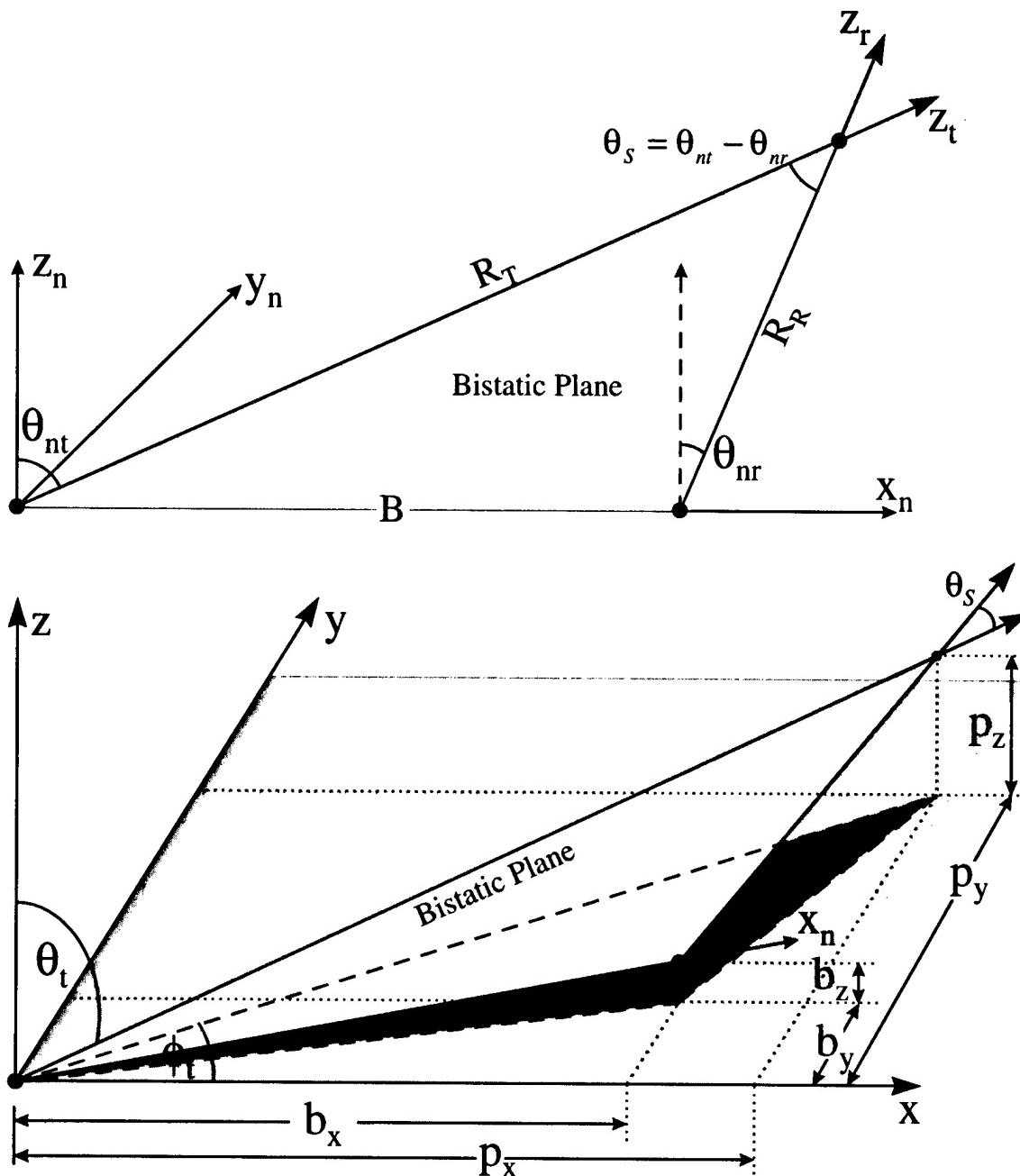
Figure 3-1: Geometry for single detector case of a bistatic lidar system.

The angles $\phi_{r,t}$ and $\theta_{r,t}$ are the standard spherical coordinate azimuth and elevation angles (t for the transmitter and r for the receiver). R_T (m) is the Euclidean distance to the target measured from the transmitter and R_R (m) is the Euclidean distance from the receiver to the target,

$$R_T^2 = \sqrt{p_x^2 + p_y^2 + p_z^2},$$
$$R_R^2 = \sqrt{(p_x - b_x)^2 + (p_y - b_y)^2 + (p_z - b_z)^2}.$$

(3.3)

Using Eq. (3.1), the relationship between the receiver and target coordinate systems is found to be

$$\begin{bmatrix} x_r \\ y_r \\ x_r \end{bmatrix} = \begin{bmatrix} \cos\theta_S & 0 & \sin\theta_S \\ 0 & 1 & 0 \\ -\sin\theta_S & 0 & \cos\theta_S \end{bmatrix} \begin{bmatrix} x_p \\ y_p \\ z_p \end{bmatrix} + \begin{bmatrix} 0 \\ 0 \\ R_R \end{bmatrix},$$

(3.4)

where $\theta_S = \theta_{nt} - \theta_{nr}$ is the bistatic angle. The relationships between the known observation point and the pointing directions of the laser and the ith receiver are

$$\cos\theta_S^i = \sin\theta_r^i \sin\theta_t \cos(\phi_t - \phi_r^i) + \cos\theta_r^i \cos\theta_t$$

$$\tan\phi_t = \frac{p_y}{p_x}$$

$$\cos\theta_t = \frac{p_z}{\left(p_x^2 + p_y^2 + p_z^2\right)^{1/2}}$$

$$\tan\phi_r^i = \frac{p_y - b_y^i}{p_x - b_x^i}$$

$$\cos\theta_r^i = \frac{p_z - b_z^i}{\left[\left(p_x - b_x^i\right)^2 + \left(p_y - b_y^i\right)^2 + \left(p_z - b_z^i\right)^2\right]^{1/2}},$$

(3.5)

and for the special cases:

$$p_x = 0 \Rightarrow \phi_r = 0 \text{ and } \theta_r \rightarrow \text{ undefined,}$$

$$p_x = b_x^i \Rightarrow \phi_r^i = 0 \text{ and } \theta_r^i \rightarrow \text{ undefined.} \tag{3.6}$$

3.2 Multistatic Doppler Lidar Measurement Model

In this section, the defined geometry is used to derive the relationship between the measured Doppler shift at each detector and the 3-dimensional vector wind for a general multistatic system. The results of this section are used to determine the effects of receiver and target location on the noise multiplication induced by the mathematical inversion.

An electromagnetic wave with radian frequency, ω (rad·sec^{-1}), and wavelength λ (m) propagating in a direction defined by the vector $\mathbf{k}_L$ (rad·m^{-1}) $\left(\left| \mathbf{k}_L \right| = k = \omega/c \right.$ $= 2\pi/\lambda \right)$ scattered by a moving particle with non-relativistic velocity $\mathbf{v}_p$ (m·sec^{-1}) into a direction $\mathbf{k}_{sc}$ (rad·m^{-1}) $\left(\left| \mathbf{k}_{sc} \right| = k = 2\pi/\lambda \right)$ will undergo a shift in frequency ω_D (rad·sec^{-1}) given by

$$\omega_D = \left(\mathbf{k}_{sc} - \mathbf{k}_L \right) \cdot \mathbf{v}_p. \tag{3.7}$$

Therefore, a measure of the particle velocity can be determined by measuring the Doppler shifted frequency of the scattered radiation. The vector $\mathbf{k}_{sc} - \mathbf{k}_L$ is the Doppler sensitive direction determined by the bistatic geometry. This Doppler sensitive direction is along the bisector of the bistatic angle, θ_S. For example, in a monostatic system, $\mathbf{k}_{sc} = -\mathbf{k}_L$, and the Doppler shift is equal to $-2k\,v_r$, where v_r is the component of $\mathbf{v}_p$ in the radial direction.

The signals scattered from these particles bear information on their movements due to the wind. In order to obtain all three components of the vector velocity $\mathbf{v}_p$, three measurements are required. Optimally, one would measure the velocity with three orthogonal Doppler sensitive directions. However, this is not possible with a purely ground based system. In a multistatic configuration with N detectors, each detector will realize a different Doppler shifted frequency as described in Eq. (3.7). In this case, the direction of $\mathbf{k}_{sc}$ will be defined for each detector as the unit vector from the observation point to the detector of interest.

Using the bistatic geometry described by *Figure 3-2*, the observation coordinates (with respect to the fixed coordinate system) are given as (p_x, p_y, p_z), and the coordinates of the detector as (b_x, b_y, b_z). With these definitions, the propagation vector of the scattered radiation for each detector can be written as

$$\mathbf{k}_{sc} = \frac{2\pi}{\lambda R_R}\left[(b_x - p_x)\hat{x} + (b_y - p_y)\hat{y} + (b_z - p_z)\hat{z}\right] \tag{3.8}$$

or

$$\mathbf{k}_{sc} = \frac{2\pi}{\lambda R_R}\big[(b_x - R_T\cos\phi_t\,\sin\theta_t)\hat{x} + (b_y - R_T\sin\phi_t\,\sin\theta_t)\hat{y}$$
$$+ (b_z - R_T\cos\theta_t)\hat{z}\big] \tag{3.9}$$

where $\hat{x}$, $\hat{y}$, and $\hat{z}$, are unit vectors in the fixed coordinate system, R_T is the Euclidean distance from the origin (the laser) to the observation point, and R_R is the Euclidean distance from the detector to the observation point.
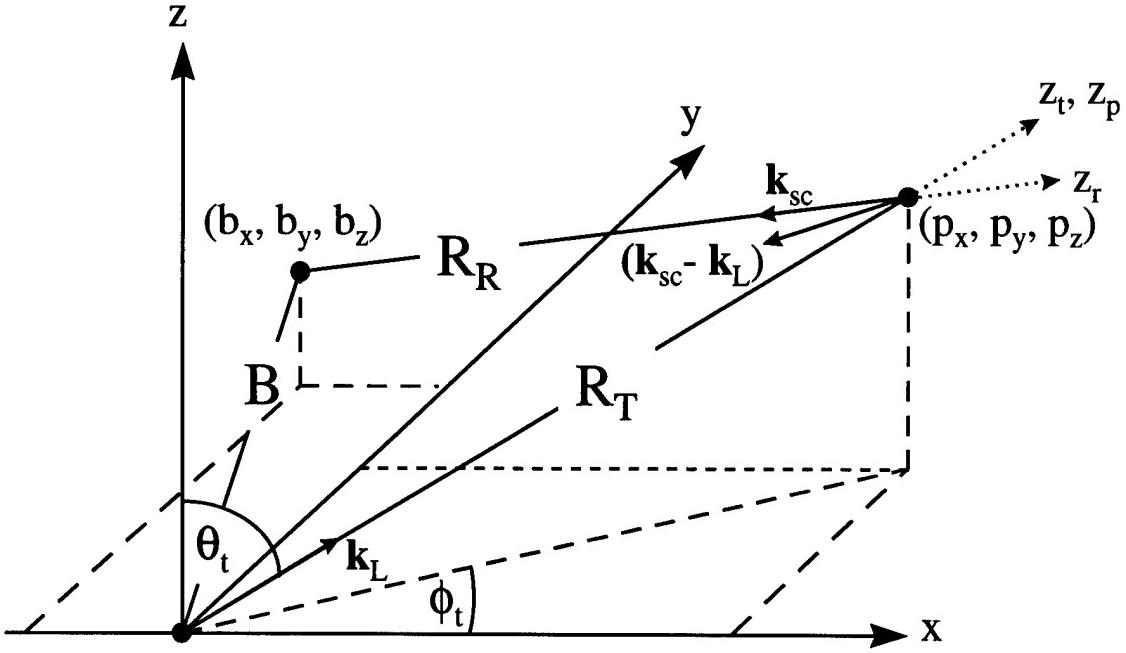
Figure 3-2: Geometry for derivation of measurement model.

Recall that the transmitter, a laser in this case, is located at the origin of the fixed coordinate system. Now the propagation vector, $\mathbf{k}_L$, can be written as

$$\mathbf{k}_L = \frac{2\pi}{\lambda R_T}\left[p_x\hat{x} + p_y\hat{y} + p_z\hat{z}\right].$$

(3.10)

Using Eqs. (3.7), (3.8), and (3.10), the Doppler shift at the detector can be written as

$$\omega_D = \frac{2\pi}{\lambda R_T}\left[\left(\frac{R_T b_x - p_x(R_T + R_R)}{R_R}\right)\hat{x} + \left(\frac{R_T b_y - p_y(R_T + R_R)}{R_R}\right)\hat{y}\right.$$
$$\left. + \left(\frac{R_T b_z - p_z(R_T + R_R)}{R_R}\right)\hat{z}\right]\cdot\mathbf{v}_p.$$

(3.11)

With multiple detectors ($i = 1 \rightarrow N$) and in matrix form, the Doppler shift at each detector becomes

$$
\begin{bmatrix} \omega_D^1 \\ \vdots \\ \omega_D^N \end{bmatrix} = \frac{2\pi}{\lambda} \left[\begin{array}{cc} \dfrac{R_T b_x^1 - p_x^1 \left(R_T + R_R^1\right)}{R_T R_R^1} & \dfrac{R_T b_y^1 - p_y^1 \left(R_T + R_R^1\right)}{R_T R_R^1} \\ \vdots & \vdots \\ \dfrac{R_T b_x^N - p_x^N \left(R_T + R_R^N\right)}{R_T R_R^N} & \dfrac{R_T b_y^N - p_y^N \left(R_T + R_R^N\right)}{R_T R_R^N} \end{array} \right.
$$

$$
\left. \begin{array}{c} \dfrac{R_T b_z^1 - p_z^1 \left(R_T + R_R^1\right)}{R_T R_R^1} \\ \vdots \\ \dfrac{R_T b_z^N - p_z^N \left(R_T + R_R^N\right)}{R_T R_R^N} \end{array} \right] \begin{bmatrix} v_p^x \\ v_p^y \\ v_p^z \end{bmatrix} \tag{3.12}
$$

where $\mathbf{v}_p = v_p^x \hat{x} + v_p^y \hat{y} + v_p^z \hat{z}$ is the particle velocity. The result of Eq. (3.12) matches that given by Huffaker [13] (with some minor modifications) for the case of three detectors evenly spaced around a circle of some radius.

Eq. (3.12) can be written in a more compact form as,

$$
\boldsymbol{\omega}_D = k\, \mathbf{A}\, \mathbf{v}_p
$$

or

$$
\mathbf{f}_D = \frac{1}{\lambda} \mathbf{A}\, \mathbf{v}_p \tag{3.13}
$$

where

$$
\mathbf{A} = \begin{bmatrix} \dfrac{b_x^1}{R_R^1} & \dfrac{b_y^1}{R_R^1} & \dfrac{b_z^1}{R_R^1} \\ \vdots & \vdots & \vdots \\ \dfrac{b_x^N}{R_R^N} & \dfrac{b_y^N}{R_R^N} & \dfrac{b_z^{N1}}{R_R^N} \end{bmatrix} - \begin{bmatrix} \dfrac{R_T + R_R^1}{R_T R_R^1} \\ \vdots \\ \dfrac{R_T + R_R^N}{R_T R_R^N} \end{bmatrix} \begin{bmatrix} p_x & p_y & p_z \end{bmatrix}, \tag{3.14}
$$

$\mathbf{f}_D$ (Hz) and $\mathbf{\omega}_D$ are column vectors whose elements are the measured Doppler shift at each of the N detectors, k is the wavenumber, and $\mathbf{A}$ (an $N \times 3$ matrix) is a mapping from a 3-dimensional space, $\Re^3$, to an N-dimensional space, $\Re^N$, where N is the number of detectors. As a check, Eq. (3.13) is evaluated for the monostatic case ($b_x^1 = b_y^1 = b_z^1 = 0$) and an observation point on the z-axis ($p_x = p_y = 0$). For this case $\mathbf{A}$ is

$$\mathbf{A} = \begin{bmatrix} 0 & 0 & 0 \end{bmatrix} - \left[\frac{2}{R_T}\right]\begin{bmatrix} 0 & 0 & R_T \end{bmatrix}$$
$$= \begin{bmatrix} 0 & 0 & -2 \end{bmatrix} \tag{3.15}$$

and $\mathbf{f}_D$ is

$$\mathbf{f}_D = \frac{1}{\lambda}\begin{bmatrix} 0 & 0 & -2 \end{bmatrix}\begin{bmatrix} v_x \\ v_y \\ v_z \end{bmatrix}$$
$$= -\frac{2}{\lambda}v_z. \tag{3.16}$$

In other words, for this configuration, the system can only measure the line-of-site (LOS) velocity. This is in agreement with standard monostatic results.

Eq. (3.13) can be inverted to find the velocity vector, $\mathbf{v}_p$, as a function of the measured Doppler shift, $\mathbf{\omega}_D$,

$$\mathbf{v}_p = \frac{1}{k}\left(\mathbf{A}^T\mathbf{A}\right)^{-1}\mathbf{A}^T\mathbf{\omega}_D. \tag{3.17}$$

If the estimates of the Doppler shift $\mathbf{\omega}_D$ at each detector are maximum likelihood estimates, then, in the limit of infinite samples, the estimation errors are unbiased and

jointly Gaussian [41]. These errors can be described by the covariance matrix $\underline{\mathbf{\Lambda}}_\varepsilon$

($\text{rad}^2 \cdot \text{sec}^{-2}$), and the error in estimating the velocity vector, $\mathbf{v}_p$, is given by

$$\underline{\mathbf{\Lambda}}_{\mathbf{v}_p} = \frac{1}{k^2}\left(\mathbf{A}^T\mathbf{A}\right)^{-1}\mathbf{A}^T\underline{\mathbf{\Lambda}}_\varepsilon\mathbf{A}\left(\mathbf{A}^T\mathbf{A}\right)^{-1}. \tag{3.18}$$

The diagonals of the matrix $\underline{\mathbf{\Lambda}}_\varepsilon$ are the measurement error variance at each

detector, σ_ω^2. This error variance will depend on the estimation scheme incorporated. In

the next section, the performance bounds on σ_ω^2 are addressed in terms of the Cramér-

Rao lower bound.

3.3 Detection and Estimation

In this section, the performance of estimating the mean frequency of the return

signal is evaluated in terms of the Cramér-Rao lower bound (CRLB). Because of the

unique geometry in this problem, the example signal model shown in *Figure 2-2* does not

apply. The signal model for this problem simplifies somewhat due to the fact that the

observation time will typically be much less than the correlation time of the return signal.

Under this condition, the problem becomes one of estimating the frequency of a signal

that has a Rayleigh amplitude and uniform phase. This problem has been treated by

van Trees [73] and is summarized here for convenience. First, the signal model is given

for the system at hand. Using this signal model, the estimation of the mean frequency is

addressed.

3.3.1 Signal Model

Assume a signal of the form

$$s_t(t) = \sqrt{2}\,\mathrm{Re}\left\{\sqrt{P_T(t)}\,\exp[i\omega_c t]\right\} \qquad -\infty < t < \infty, \tag{3.19}$$

where $i = \sqrt{-1}$, ω_c (rad·sec^{-1}) is the carrier frequency, and $P_T(t)$ (W) is the transmitted

power, which for a pulsed system includes the pulse shape. Now assume that there are K

scatterers within some illuminated volume. The return signal, for zero Doppler shift, is

thus given by

$$s_r(t) = \sqrt{2}\,\mathrm{Re}\left\{\sqrt{P_T(t)}\sum_{i=1}^{K} g_i\,\exp[i\omega_c(t-\tau)+\theta_i]\right\}. \tag{3.20}$$

The attenuation factor g_i includes the effects of transmit and receiver aperture sizes, two

way path loss, and scattering cross section of each particle. The random phase angle θ_i is

included to account for the random position of the particles within the volume, as well as

any phase effects in the scattering process. The time delay, τ (sec), is the mean round trip

propagation time over the scattering volume, and in our case is considered to be a known

parameter given by

$$\tau = \frac{R_T + R_R}{c}. \tag{3.21}$$

Assume that the θ_i are statistically independent and K is large. Under the central

limit theorem [74], the return signal can then be written as

$$s_r(t) = \sqrt{2}\,\mathrm{Re}\left\{\sqrt{P_T(t-\tau)}\,\tilde{b}\,\exp[i\omega_c(t-\tau)]\right\}, \tag{3.22}$$

where $\tilde{b}$ is a complex Gaussian random variable. The envelope of $\tilde{b}$ is a Rayleigh random variable whose moments are

$$\mathrm{E}\left\{\left|\tilde{b}\right|\right\} = \sqrt{\frac{\pi}{2}}\sigma_b \quad \text{and} \quad \mathrm{E}\left\{\left|\tilde{b}\right|^2\right\} = 2\sigma_b^2 \,, \tag{3.23}$$

where $\mathrm{E}\{\cdot\}$ denotes the expected value. The phase of $\tilde{b}$ is uniform. The value of σ_b includes system and path losses as well as the scattering cross section of the target. In practice, the number of scatterers does not have to be very large for the Gaussian approximation to be valid [73].

Including the effects of target velocity, the return signal is given by

$$s_r(t) = \sqrt{2}\,\mathrm{Re}\left\{\sqrt{E_t}\,\tilde{b}\,\tilde{f}(t-\tau)\exp\left[i(\omega_c + \omega_D)t\right]\right\}, \tag{3.24}$$

where ω_D is the Doppler shift, $\tilde{f}(t)$ (sec$^{-\frac{1}{2}}$) is the complex envelop of the transmitted signal, and the transmitted power is written as the product of the transmitted energy, E_t (J), and the squared magnitude of the complex envelope

$$P_T(t) = E_t\left|\tilde{f}(t)\right|^2. \tag{3.25}$$

The complex envelope is normalized such that

$$\int_{-\infty}^{\infty}\left|\tilde{f}(t)\right|^2 dt = 1. \tag{3.26}$$

In Eq. (3.24), the phase term $\omega_c\tau$ can be absorbed into the random phase of $\tilde{b}$ because the phase of $\tilde{b}$ is uniform.

Gaussian noise $n(t)$ that has a bandpass spectrum can be represented as

$$n(t) = \sqrt{2} \operatorname{Re}\left\{\tilde{n}(t) \exp\left[i\omega_c t\right]\right\}, \tag{3.27}$$

where $\tilde{n}(t)$ is the complex envelope of the noise. With the addition of noise, the return signal is

$$r(t) = \sqrt{2E_t} \operatorname{Re}\left\{\tilde{b} \tilde{f}(t-\tau) \exp\left[i(\omega_c + \omega_D)t\right]\right\} + \sqrt{2} \operatorname{Re}\left\{\tilde{n}(t) \exp\left[i\omega_c t\right]\right\}, \tag{3.28}$$

or in complex notation

$$r(t) = \sqrt{2} \operatorname{Re}\left\{\tilde{r}(t) \exp\left[i\omega_c t\right]\right\}, \tag{3.29}$$

where

$$\begin{aligned}
\tilde{r}(t) &\equiv \tilde{b}\sqrt{E_t}\tilde{f}(t-\tau) \exp\left[i\omega_D t\right] + \tilde{n}(t) \\
&= \tilde{s}(t) \exp\left[i\omega_D t\right] + \tilde{n}(t).
\end{aligned} \tag{3.30}$$

Assume that the additive noise is white bandpass Gaussian noise, $\tilde{w}(t)$, with spectral height $N_0/2$, and drop the subscript D from the frequency shift for simplicity. Then the complex envelope of the received signal is

$$\tilde{r}(t) = \tilde{b}\sqrt{E_r}\tilde{f}(t-\tau) \exp\left[i\omega t\right] + \tilde{w}(t), \qquad -\infty < t < \infty. \tag{3.31}$$

The average received signal energy is

$$\begin{aligned}
\overline{E}_r &\equiv \operatorname{E}\left\{\int_{-\infty}^{\infty} \left|s_r(t)\right|^2 dt\right\} \\
&= 2\sigma_b^2 E_t,
\end{aligned} \tag{3.32}$$

and the complex white noise has covariance function

$$\tilde{K}_{\tilde{w}}(t,u) = N_0\delta(t-u), \qquad -\infty < t, u < \infty. \tag{3.33}$$

The parameter ω is an unknown parameter whose value will be estimated.

Maximum likelihood estimation of ω is obtained by adjusting the estimated value of ω until the likelihood function Λ is maximized [41]. For the model described in Eq. (3.31), the logarithm of the likelihood function is [73]

$$\ln \Lambda_1(\tau,\omega) = \frac{1}{N_0} \frac{\overline{E}_r}{N_0 + \overline{E}_r} \left| \tilde{L}(\tau,\omega) \right|^2 , \tag{3.34}$$

where $\tilde{L}(\tau,\omega)$ is the sufficient statistic and is given by

$$\tilde{L}(\tau,\omega) = \int_{-\infty}^{\infty} \tilde{r}(t)\tilde{f}^*(t-\tau)\exp[-i\omega t]\,dt . \tag{3.35}$$

Recall that τ is assumed to be known and does not need to be estimated from the return signal.

Because the coefficient in Eq. (3.34) is not a function of τ or ω, it will have no effect on the minimization, and thus can be dropped for determining the maximum likelihood estimator. However, the coefficient is important when calculating the bounds on the performance of the estimator, for example, when calculating the CRLB. Thus, the estimator is reduced to the maximization of the function

$$\ln \Lambda(\tau,\omega) = \left| \tilde{L}(\tau,\omega) \right|^2 \tag{3.36}$$

with respect to ω. The value of ω that maximizes this function will be denoted $\hat{\omega}_{ml}$, and because only maximum likelihood estimators are being considered here, the subscript ml will be dropped in subsequent expressions.

Substituting Eq. (3.31) into Eq. (3.35), the log-likelihood ratio becomes [73]

$$\Lambda(\tau,\omega) = E_t |\tilde{b}|^2 \left\{ \left| \int_{-\infty}^{\infty} \tilde{f}(t-\tau)\tilde{f}^*(t-\tau+\tau')e^{i\omega't}dt \right|^2 \right\}$$

$$+ 2\,\text{Re}\left\{ \sqrt{E_t}\tilde{b}\left[\int_{-\infty}^{\infty} \tilde{f}^*(t-\tau)\tilde{f}(t-\tau+\tau')e^{-i\omega't}dt \right]\tilde{n}^*(\tau,\omega) \right\}$$

$$+ |\tilde{n}(\tau,\omega)|^2, \tag{3.37}$$

where

$$\tilde{n}(\tau,\omega) = \int_{-\infty}^{\infty} \tilde{w}(t)\tilde{f}^*(t-\tau)e^{-i\omega t}dt, \tag{3.38}$$

$\tau' = \tau - \tau_a$, $\omega' = \omega - \omega_a$, ω and τ are variables in the likelihood function, and ω_a and τ_a are the actual Doppler shift and time delay, respectively. Make the substitution

$$z = t - \tau + \frac{\tau'}{2}, \tag{3.39}$$

and designate the first term in Eq. (3.37) as $\theta(\tau', \omega')$, then

$$\theta(\tau',\omega') \equiv \left| \int_{-\infty}^{\infty} \tilde{f}\left(z-\frac{\tau'}{2}\right)\tilde{f}^*\left(z+\frac{\tau'}{2}\right)e^{i\omega'z}dz \right|^2$$

$$= |\phi(\tau',\omega')|^2, \tag{3.40}$$

where $\phi(\tau', \omega')$ is the time-frequency autocorrelation function of $\tilde{f}(t)$, defined by

$$\phi(\tau',\omega') \equiv \int_{-\infty}^{\infty} \tilde{f}\left(t-\frac{\tau'}{2}\right)\tilde{f}^*\left(t+\frac{\tau'}{2}\right)e^{i\omega't}dt. \tag{3.41}$$

The function $\theta(\tau', \omega')$ is referred to as the ambiguity function.

In the next section, the lower bound on the variance of the estimation errors is given in terms of the signal model presented. For this signal model, the parameters to be estimated are τ and ω. Once the general expression for estimation of these two

parameters is given, the estimation of τ will be ignored because this parameter can be assumed to be known for a given geometry.

3.3.2 Cramér-Rao Lower Bound (CRLB)

The variance of any unbiased estimate is bounded by the diagonal elements of the Fisher information matrix $\underline{\mathbf{J}}$ and is called the Cramér-Rao lower bound [41, 42]. The elements of the Fisher information matrix are given by

$$J_{ij} = -E\left[\frac{\partial^2 \ln \Lambda(\mathbf{A})}{\partial A_i \partial A_j}\right],\tag{3.42}$$

where $\mathbf{A}$ are the parameters to be estimated and Λ is the likelihood function. Let the estimated parameters be τ and ω, $\mathbf{A} = [\tau, \omega]$, even though τ will not be estimated from the return signal. Then the elements of $\underline{\mathbf{J}}$ are

$$J_{11} = -E\left[\frac{\partial^2 \ln \Lambda_1(\tau,\omega)}{\partial \tau^2}\right],$$

$$J_{22} = -E\left[\frac{\partial^2 \ln \Lambda_1(\tau,\omega)}{\partial \omega^2}\right],$$

$$J_{12} = J_{21} = -E\left[\frac{\partial^2 \ln \Lambda_1(\tau,\omega)}{\partial \tau \partial \omega}\right].\tag{3.43}$$

Substituting the log-likelihood function from Eq. (3.37) into Eq. (3.43) the matrix elements become

$$J_{11} = \frac{2\overline{E}_r}{N_0}\left(\frac{\overline{E}_r}{N_0 + \overline{E}_r}\right)\left(\overline{\omega^2} - \overline{\omega}^2\right),$$

$$J_{12} = \frac{2\overline{E}_r}{N_0}\left(\frac{\overline{E}_r}{N_0 + \overline{E}_r}\right)\left(\overline{\omega t} - \overline{\omega}\,\overline{t}\right),$$

$$J_{22} = \frac{2\overline{E}_r}{N_0}\left(\frac{\overline{E}_r}{N_0 + \overline{E}_r}\right)\left(\overline{t^2} - \overline{t}^2\right), \tag{3.44}$$

where

$$\overline{\omega^2} = \frac{1}{2\pi}\int_{-\infty}^{\infty}\omega^2\left|\tilde{F}(j\omega)\right|^2 d\omega,$$

$$\overline{\omega t} \equiv \mathrm{Im}\int_{-\infty}^{\infty} u\,\tilde{f}(u)\frac{\partial \tilde{f}^*(u)}{\partial u}du,$$

$$\overline{t^2} = \int_{-\infty}^{\infty} u^2\left|\tilde{f}(u)\right|^2 du. \tag{3.45}$$

The mean-square bandwidth $\left(\overline{\omega^2} - \overline{\omega}^2\right)$ is an approximate measure of the frequency

spread of the signal. The mean-square duration, $\left(\overline{t^2} - \overline{t}^2\right)$, is an approximate measure of

the time spread of the signal. The quantity $\left(\overline{\omega t} - \overline{\omega}\,\overline{t}\right)$ is a measure of the frequency

modulation of the complex envelope.

The mean frequency of the envelope, $\overline{\omega}$, is defined as the first moment of the

energy spectrum of the complex envelope

$$\overline{\omega} \equiv \frac{1}{2\pi}\int_{-\infty}^{\infty}\omega\left|\tilde{F}(j\omega)\right|^2 d\omega, \tag{3.46}$$

where $\tilde{F}(j\omega)$ is the Fourier transform of $\tilde{f}(t)$,

$$\tilde{F}(j\omega) = \int_{-\infty}^{\infty} \tilde{f}(t)e^{-j\omega t}dt . \tag{3.47}$$

The mean time of the envelope, $\bar{t}$, is defined as the first moment of the squared magnitude of the complex envelope,

$$\bar{t} \equiv \int_{-\infty}^{\infty} t\left|\tilde{f}(t)\right|^2 dt . \tag{3.48}$$

Since the time origin is arbitrary, it can always be chosen so that $\bar{t} = 0$. Likewise, since the carrier frequency is arbitrary, it may also be chosen so that $\overline{\omega} = 0$.

The Fisher information matrix can then be given as

$$\underline{J} = \frac{2\overline{E}_r}{N_0}\left(\frac{\overline{E}_r}{N_0 + \overline{E}_r}\right)\left[\begin{array}{cc} \overline{\omega^2} & \overline{\omega t} \\ \overline{\omega t} & \overline{t^2} \end{array}\right], \tag{3.49}$$

and the variance on the estimation errors are given by

$$\mathrm{Var}[\hat{\tau} - \tau] = \sigma_\tau^2 \geq \left[\frac{2\overline{E}_r}{N_0}\left(\frac{\overline{E}_r}{N_0 + \overline{E}_r}\right)\right]^{-1}\left[\frac{\overline{t^2}}{\overline{\omega^2}\,\overline{t^2} - \left(\overline{\omega t}\right)^2}\right], \tag{3.50}$$

and

$$\mathrm{Var}[\hat{\omega} - \omega] = \sigma_\omega^2 \geq \left[\frac{2\overline{E}_r}{N_0}\left(\frac{\overline{E}_r}{N_0 + \overline{E}_r}\right)\right]^{-1}\left[\frac{\overline{\omega^2}}{\overline{\omega^2}\,\overline{t^2} - \left(\overline{\omega t}\right)^2}\right]. \tag{3.51}$$

As can be seen from Eq. (3.45), a sufficient condition for the bounds on the estimation errors to be uncoupled is that the complex envelope be real. In this case

$$\sigma_\tau^2 \geq \left[\frac{2\overline{E}_r}{N_0}\left(\frac{\overline{E}_r}{N_0 + \overline{E}_r}\right)\right]^{-1}\left[\frac{1}{\overline{\omega^2}}\right], \tag{3.52}$$

and

$$\sigma_\omega^2 \geq \left[\frac{2\overline{E}_r}{N_0} \left(\frac{\overline{E}_r}{N_0 + \overline{E}_r} \right) \right]^{-1} \left[\frac{1}{\overline{t^2}} \right], \tag{3.53}$$

for all unbiased estimates with $\overline{\omega t} = 0$. It should be noted that Eqs. (3.52) and (3.53) are bounds even when $\overline{\omega t} \neq 0$, but they are not as tight as Eqs. (3.50) and (3.51).

It is interesting to note that if the return amplitude is modeled as a known parameter or an unknown nonrandom parameter, the coefficient in Eq. (3.49) is changed, i.e.,

$$\frac{2\overline{E}_r}{N_0} \left(\frac{\overline{E}_r}{N_0 + \overline{E}_r} \right) \to \frac{2\overline{E}_r}{N_0}. \tag{3.54}$$

Therefore, the term in parenthesis in Eq. (3.54) is due to the random nature of the return amplitude, or the speckle contribution.

The term $\overline{E}_r / N_0$ is the energy to noise ratio. Because the lidar community typically works with a power signal to noise ratio, a relationship between the two quantities is needed. The expected value of the received energy can be written as

$$\overline{E}_r = \int_{-\infty}^{\infty} \text{SNR}(t) N \, dt, \tag{3.55}$$

where N is the noise power,

$$N = N_0 B_w, \tag{3.56}$$

and B_w (Hz) is the system bandwidth. Assume that the SNR has a form given by

$$\text{SNR}(t) = \text{SNR}_{\max} g(t), \tag{3.57}$$

where $g(t)$ is defined by

$$\int_{-\infty}^{\infty} g(t)\mathrm{d}t = T_g,$$

$$\max[g(t)] = 1. \tag{3.58}$$

Then the energy to noise ratio becomes

$$\frac{\overline{E_r}}{N_0} = \mathrm{SNR}_{\max}T_g B_w. \tag{3.59}$$

The parameter T_g (sec) is a measure of the time duration of the observation interval. For a CW system, the function $g(t)$ represents the time weighting function, or time gate. For a pulsed system, $g(t)$ is the pulse shape convolved with the profile of the scattering volume along the propagation direction.

A more useful parameter than the SNR to describe the signal power for frequency estimation with coherent lidar systems is the effective number of photoelectrons coherently detected per observation interval, also called the number of "coherent photoelectrons" by Kavaya [54]. This parameter has been used by Menzies [75] and by Frehlich [54]. The number of coherent photoelectrons in the differential time interval $\mathrm{d}t$ is

$$\mathrm{d}\Phi = \mathrm{SNR}(t)\, B_w \mathrm{d}t. \tag{3.60}$$

The total number of coherent photoelectrons over the entire observation time is

$$\Phi = \int_{-\infty}^{\infty} \mathrm{SNR}(t) B_w \mathrm{d}t$$

$$= \mathrm{SNR}_{\max} T_g B_w = \frac{\overline{E_R}}{N_0}. \tag{3.61}$$

Therefore, the energy-to-noise ratio in Eq. (3.54) is equivalent to the number of coherent photoelectrons for a heterodyne detection system. Now the CRLB for the variance of the estimation error for ω can be expressed in terms of Φ as

$$\sigma_\omega^2 \geq \frac{\Phi+1}{2\Phi^2}\frac{1}{\overline{t^2}}. \tag{3.62}$$

Now that the dependence of the estimation error on Φ has been determined, the next step is to determine Φ by calculating the SNR. The next section gives general expressions for the signal-to-noise ratio. The number of coherent photoelectrons is system specific and will be determined in Chapter 4.

3.4 Signal-to-Noise Ratio: General

In this section, the generalized coherent lidar signal-to-noise (SNR) expressions are given. The derivations closely follow the derivations of Frehlich and Kavaya [32] with the generalization for a bistatic geometry with baselines much greater than the aperture sizes used. The geometry for a bistatic coherent lidar system is shown in *Figure 3-3*. The transmitter lens is located in the plane defined by $z_t = 0$ and the position vector $\mathbf{u}$ (m), and the receiver lens is located in the plane defined $z_r = 0$ and by position vector $\mathbf{v}$ (m). The position vector $\mathbf{p}$ (m) defines the transverse plane ($z_t = R_T$) at the target location. The detector is located at transverse coordinate $\mathbf{w}$ (m) and distance L (m) from the receiver plane (a positive L implies a negative z_r). The receiver and transmitter lenses are described by dimensionless response functions $W_R(\mathbf{v})$ and $W_T(\mathbf{u})$ respectively.
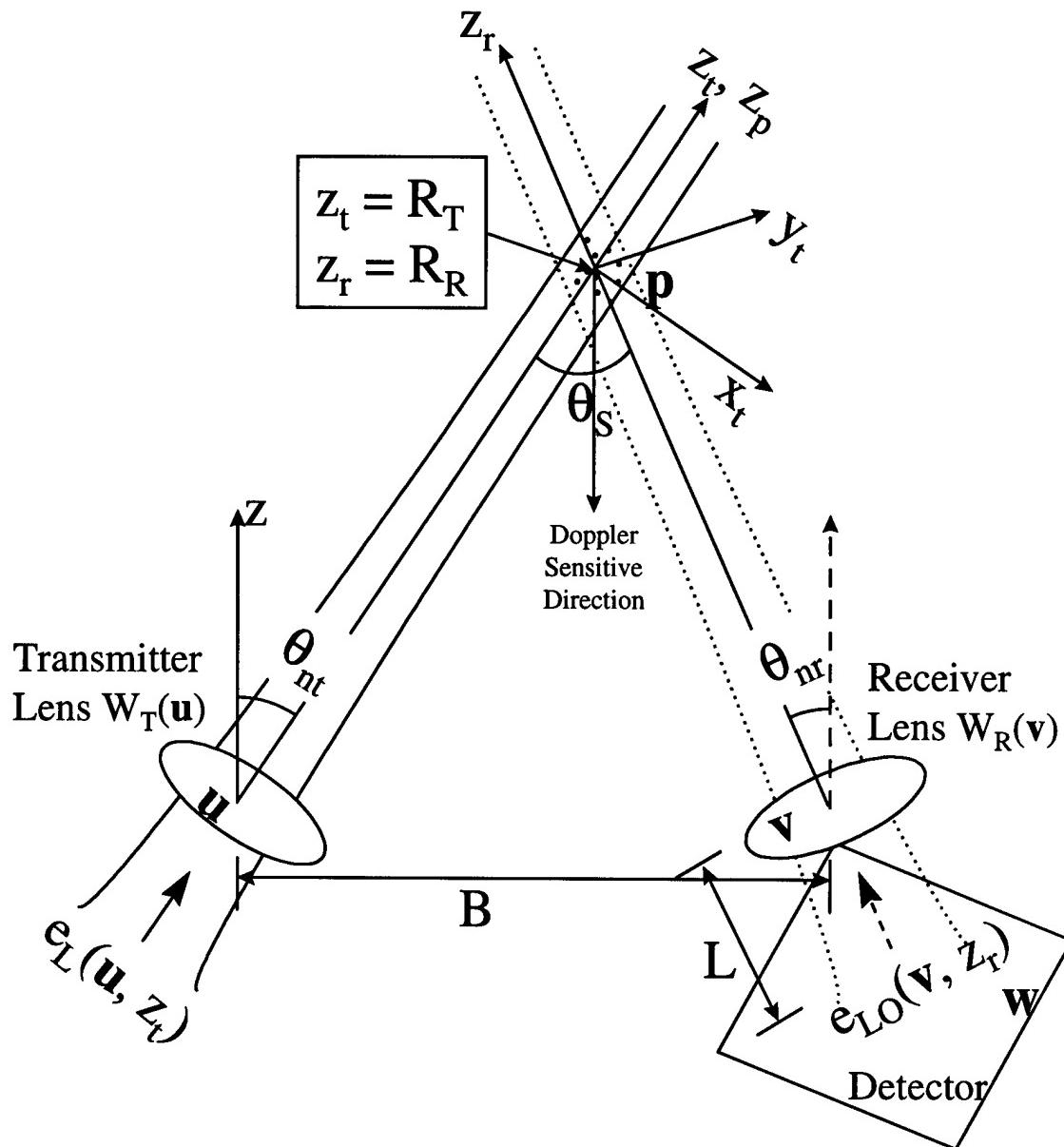
Figure 3-3: Geometry for a bistatic coherent lidar system (drawn in the bistatic plane).

3.4.1 Detector Plane

The optical scalar field, $\Psi_T(\mathbf{u}, z_t, t)$ ($W^{1/2} \cdot m^{-1}$) of the transmitted laser pulse in a homogeneous medium is

$$\Psi_T(\mathbf{u}, z_t, t) = E_T(\mathbf{u}, z_t, t) \exp(ikz_t - \omega t), \tag{3.63}$$

where t is time (sec), $i = \sqrt{-1}$, $k = 2\pi/\lambda$ (rad$\cdot$m^{-1}) is the wave number, λ (m) is the wavelength, $\omega = 2\pi\nu$ (rad$\cdot$sec^{-1}) is the angular frequency, ν (Hz) is the optical frequency, and $E_T(\mathbf{u}, z_t, t)$ ($W^{1/2} \cdot m^{-1}$) is the scalar field amplitude. In the absence of extinction,

$$\int_{-\infty}^{\infty} |\Psi_T(\mathbf{u}, z, t)|^2 d^2\mathbf{u} = \int_{-\infty}^{\infty} |E_T(\mathbf{u}, z, t)|^2 d^2\mathbf{u} = P_T(t - z/c) \tag{3.64}$$

where $|\cdot|$ denotes absolute value, $P_T(t)$ (W) is the transmitted laser power as a function of time, c (m$\cdot$sec^{-1}) is the speed of light, and $d^2\mathbf{u}$ denotes a two-dimensional integration over the plane defined by z_t. It is also assumed that the pulse profile varies slowly compared to the period $1/\nu$. The scattered field $\Psi_S(\mathbf{v}, z_r, t)$ ($W^{1/2} \cdot m^{-1}$) is collected by the receiver and mixed with a local oscillator (LO) field on the surface of the detector at transverse coordinate $\mathbf{w}$. It is assumed that the scattered field and the LO field have identical polarization. If this is not the case (i.e. the scattered field is depolarized by the target), there will be a decrease in the SNR proportional to the degree of depolarization.

The field incident on the detector $\Psi_D(\mathbf{w}, L, t)$ is given by

$$\Psi_D(\mathbf{w}, L, t) = E_S(\mathbf{w}, L, t) \exp\left[i\left(kL - \omega t + \phi_S\right)\right]$$
$$+ E_{LO}(\mathbf{w}, L, t) \exp\left[i\left(kL - \omega_{LO}t\right)\right], \tag{3.65}$$

where $E_S(\mathbf{w}, L, t)$ is the scattered field amplitude in the detector plane, $E_{LO}(\mathbf{w}, L, t)$ is the LO field amplitude in the detector plane, ω_{LO} is the angular frequency of the LO, and ϕ_S (rad) is the random phase of the scattered field with respect to the LO field. The signal current for an ideal square law detector (photomultiplier or photodiode, for example) is given by

$$I(t) = \frac{G_D e}{h\nu} \int_D \eta_Q(\mathbf{w}) \left|\Psi_D(\mathbf{w}, L, t)\right|^2 d^2\mathbf{w}, \tag{3.66}$$

where $\eta_Q(\mathbf{w})$ (electrons/photon) is the detector quantum efficiency as a function of location on the detector, G_D is the amplifier gain, $e = 1.602 \times 10^{-19}$ (C/electron) is the electronic charge, $h = 6.626 \times 10^{-19}$ (J·sec) is Planck's constant, and $\int_D \cdot$ denotes integration over the detector surface.

Substitution of Eq. (3.65) into Eq. (3.66) yields

$$I(t) = \frac{G_D e}{h\nu} \int_D \eta_Q(\mathbf{w}) \left|E_{LO}(\mathbf{w}, L, t)\right|^2 d^2\mathbf{w} +$$
$$\frac{G_D e}{h\nu} \int_D \eta_Q(\mathbf{w}) \left|E_S(\mathbf{w}, L, t)\right|^2 d^2\mathbf{w} +$$
$$\frac{2 G_D e}{h\nu} \mathrm{Re} \int_D \eta_Q(\mathbf{w}) E_S(\mathbf{w}, L, t) E_{LO}^*(\mathbf{w}, L, t) \exp(i\Delta\omega t + i\phi_S) d^2\mathbf{w}, \tag{3.67}$$

where Re($\cdot$) denotes the real part. The first term in Eq. (3.67) is the direct current, $I_{dc}(t)$, caused by the LO, the second term is the direct detection signal current, $I_S(t)$, from the scattered field, and the last term is the intermediate-frequency (i.f.) signal current, $i_s(t)$, at frequency $\Delta\omega = \omega_{LO} - \omega \ll \omega$.

The direct current caused by the LO can be simplified by noting that the effective LO power (W) is given by

$$P_{LOD}(t) = \int_D \eta_Q(\mathbf{w}) |E_{LO}(\mathbf{w}, L, t)|^2 d^2\mathbf{w}.$$ (3.68)

Likewise, the direct detection signal current can be simplified by noting that the effective direct detection power measured by the detector is given by

$$P_D(t) = \int_D \eta_Q(\mathbf{w}) |E_S(\mathbf{w}, L, t)|^2 d^2\mathbf{w}.$$ (3.69)

The i.f. signal current, $i_s(t)$, is obtained by bandpass filtering the total signal to remove the dc and direct detection portions as well as unnecessary noise. The i.f. signal current is then converted to power with a squaring circuit and a low-pass filter with bandwidth B_w (Hz). The average i.f. signal power is then given by [32]

$$\langle i_s^2(t) \rangle = 2\left(\frac{G_D e}{h\nu}\right)^2 \int_D \int_D \eta_Q(\mathbf{w}_1)\eta_Q(\mathbf{w}_2) M_S(\mathbf{w}_1, \mathbf{w}_2, L, t)$$
$$\times M_{LO}^*(\mathbf{w}_1, \mathbf{w}_2, L) d^2\mathbf{w}_1 d^2\mathbf{w}_2$$ (3.70)

where $\langle \cdot \rangle$ denotes the ensemble average, or time average for an ergodic process,

$$M_S(\mathbf{w}_1, \mathbf{w}_2, L, t) = \langle E_S(\mathbf{w}_1, L, t) E_S^*(\mathbf{w}_2, L, t) \rangle$$ (3.71)

is the mutual coherence function (W·m^{-2}) of the scattered field in the detector plane. $M_{LO}(\mathbf{w}_1, \mathbf{w}_2, L)$ is the mutual coherence function of the LO field, where it is assumed that the LO field is stationary, thus independent of time. It is also assumed that the LO field and the scattered field are statistically independent, and the random phase, ϕ_S, is uniformly distributed over $(0, 2\pi)$.

If the noise is dominated by the LO shot noise [76], the average noise power (A^2) caused by the Poisson statistics of shot noise is given by

$$\langle i_N^2 \rangle = 2 G_D e B_w \langle I_{dc} \rangle,$$ (3.72)

where I_{dc} is the average dc signal current, which is also independent of time since the LO field is stationary. The signal-to-noise ratio (SNR) is then given as

$$\begin{aligned} \text{SNR}(t) &= \frac{\langle i_s^2(t) \rangle}{\langle i_N^2 \rangle} \\ &= \frac{1}{h\nu B_w \langle P_{LOD} \rangle} \int_D \int_D \eta_Q(\mathbf{w}_1) \eta_Q(\mathbf{w}_2) M_S(\mathbf{w}_1, \mathbf{w}_2, L, t) M_{LO}^*(\mathbf{w}_1, \mathbf{w}_2, L) \\ &\quad \times d^2\mathbf{w}_1 d^2\mathbf{w}_2, \end{aligned}$$ (3.73)

where $\langle P_{LOD} \rangle$ is the average effective LO power measured by the detector [Eq. (3.68)].

It is also useful to describe the performance of a coherent lidar using the heterodyne efficiency, η_H, which is a measure of the loss in coherent power when the received field and LO field are not perfectly matched [77, 78]. For random fields, the heterodyne efficiency is given by [32]

$$\begin{aligned} \eta_H(t) &= \frac{\langle i_S^2(t) \rangle}{2 \langle I_{dc} \rangle \langle I_S(t) \rangle} \\ &= \frac{\int_D \int_D \eta_Q(\mathbf{w}_1) \eta_Q(\mathbf{w}_2) M_S(\mathbf{w}_1, \mathbf{w}_2, L, t) M_{LO}^*(\mathbf{w}_1, \mathbf{w}_2, L) d^2\mathbf{w}_1 d^2\mathbf{w}_2}{\langle P_D(t) \rangle \langle P_{LOD} \rangle}. \end{aligned}$$ (3.74)

The heterodyne efficiency has a maximum value of 1.0 when the scattered field is proportional to the LO field, $E_S(\mathbf{w}, L, t) \propto E_{LO}(\mathbf{w}, L)$. This can be shown by using the Schwartz inequality [see ref. 79]. Using the equations for SNR and heterodyne efficiency [Eqs. (3.73) and (3.74)] the SNR can be expressed as

$$\text{SNR}(t) = \frac{\langle P_D(t) \rangle}{h \nu B_w} \eta_H(t) .\tag{3.75}$$

This form shows that the SNR is dependent on two physical quantities: the average direct detection power $\langle P_D(t) \rangle$ and the heterodyne efficiency $\eta_H(t)$.

3.4.2 Receiver Plane

It is often convenient to perform the above calculations in a plane other than the detector plane. These calculations can be constructed using a technique first described by Siegman [80]. This technique involves the back-propagation of the local oscillator field to the plane where the calculations are to be performed. The back-propagated local oscillator (BPLO) calculations were formalized by Rye [81, 82].

The scattered field incident on the detector is related to the scattered field incident on the receiver by

$$E_S(\mathbf{w}, L, t) = \int_{-\infty}^{\infty} E_S(\mathbf{v}, 0, t) W_R(\mathbf{v}) G^f(\mathbf{w}; \mathbf{v}, L) d^2 \mathbf{v} \tag{3.76}$$

where

$$G^f(\mathbf{w}; \mathbf{v}, L) = \frac{k}{2\pi i L} \exp\left[\frac{ik}{2L} (\mathbf{w} - \mathbf{v})^2 \right] \tag{3.77}$$

is the Fresnel approximation form of the free space Green's function (m^{-2}).

Frehlich and Kavaya [32] show that the SNR in the receiver plane (defined by the plane $z_r = 0$) is given by

$$\text{SNR}(t) = \frac{1}{h\nu B_w \langle P_{LOD} \rangle} \int_{-\infty}^{\infty}\int_{-\infty}^{\infty} M_S(\mathbf{v}_1,\mathbf{v}_2,0,t) M_{BPLO}(\mathbf{v}_1,\mathbf{v}_2,0)d^2\mathbf{v}_1 d^2\mathbf{v}_2 \qquad (3.78)$$

where

$$E_{BPLO}(\mathbf{v},0) = W_R(\mathbf{v})\frac{k^2}{L^2}\int_{-\infty}^{\infty} E_{LO}^*(\mathbf{w},0)\, Y\left[(\mathbf{v}-\mathbf{w})\frac{k}{L}\right]\exp\left[\frac{ik}{2L}(v^2-w^2)\right]d^2\mathbf{w} \qquad (3.79)$$

is the field of the BPLO on the target side of the receiver aperture, which can also be

regarded as the field of the reciprocal receiver [83], $v^2 = \mathbf{v}\cdot\mathbf{v}$, $w^2 = \mathbf{w}\cdot\mathbf{w}$,

$$Y(\kappa) = \int_{-\infty}^{\infty} \eta_Q(\mathbf{w})\exp(-i\kappa\cdot\mathbf{w})d^2\mathbf{w} \qquad (3.80)$$

is the 2-d Fourier transform (m^2) of the detector quantum efficiency spatial response

function $\eta_Q(\mathbf{w})$, and κ (rad $\cdot$ m^{-1}) is the 2-d spatial wave vector. $E_{LO}(\mathbf{v}, 0)$ is the LO field

at the receiver plane ($z_r = 0$), $M_S(\mathbf{v}_1, \mathbf{v}_2, 0, t)$ is the mutual coherence function [see Eq.

(3.71)] of the scattered field $E_S(\mathbf{v}, 0, t)$ incident on the receiver aperture, and

$M_{BPLO}(\mathbf{v}_1, \mathbf{v}_2, 0)$ is the mutual coherence function of $E_{BPLO}(\mathbf{v}, 0)$. Eq. (3.78) is identical

to Eq. (3.73) except that the calculations are performed in the receiver plane instead of the

detector plane. While performing the calculations in the detector plane can provide

useful insight, calculations in the receiver plane remove the complexity of propagating

the random scattered field through the receiver optics.

3.4.3 Target Plane

In a very similar manner to that described in Section 3.4.2, the target plane

expression for the SNR can be found. The transmitted field incident on a target with

transverse target coordinates $\mathbf{p}$ and range $z_t = R_T$ is given as (ignoring extinction, for now)

$$E_T(\mathbf{p}, R_T, t) = \int_{-\infty}^{\infty} E_L(\mathbf{u}, 0, t - R_T/c) W_T(\mathbf{u}) G(\mathbf{p}; \mathbf{u}, R_T) d^2\mathbf{u}, \qquad (3.81)$$

where $G(\mathbf{p}; \mathbf{u}, R_T)$ is the Green's function for wave propagation in a turbulent medium

and $E_L(\mathbf{u}, z_t, t)$ is the field of the laser. In the absence of refractive turbulence, the

Green's function is the free-space Green's function, $G(\mathbf{p}; \mathbf{u}, R_T) = G^f(\mathbf{p}; \mathbf{u}, R_T)$ [see Eq.

(3.77)].

The scattered field at the target can be expressed as [84]

$$E_S(\mathbf{p}, R_T, t) = \int_{-\infty}^{\infty} E_T(\mathbf{q}, R_T, t) V(\mathbf{q}, \mathbf{p}) d^2\mathbf{q} \qquad (3.82)$$

where $V(\mathbf{q}, \mathbf{p})$ $(\text{m}^{-2} \cdot \text{sr}^{-\frac{1}{2}})$ is the scattering coefficient of the target. The scattered field at

the receiver becomes

$$E_S(\mathbf{v}, 0, t) = \int_{-\infty}^{\infty} \int_{-\infty}^{\infty} E_T(\mathbf{q}, R_T, t - R_T/c) V(\mathbf{q}, \mathbf{p}) G(\mathbf{p}; \mathbf{v}, R_R) d^2\mathbf{q} \, d^2\mathbf{p} \qquad (3.83)$$

where the reciprocity theorem for the Green's function [85], $G(\mathbf{v}; \mathbf{p}, R) = G(\mathbf{p}; \mathbf{v}, R)$, has

been applied. Then the target plane SNR is expressed as

$$\text{SNR}(t) = \frac{K_T(R_T)K_R(R_R)}{h\nu B_w \langle P_{LOD} \rangle} \int_{-\infty}^{\infty}\int_{-\infty}^{\infty}\int_{-\infty}^{\infty}\int_{-\infty}^{\infty} B(\mathbf{q}_1,\mathbf{q}_2,\mathbf{p}_1,\mathbf{p}_2)$$

$$\times \left\langle E_T(\mathbf{q}_1,R_T,t-R_T/c)E_T^*(\mathbf{q}_2,R_T,t-R_T/c) \right.$$

$$\times \left. E_{BPLO}(\mathbf{p}_1,R_R)E_{BPLO}(\mathbf{p}_2,R_R) \right\rangle d^2\mathbf{q}_1\, d^2\mathbf{q}_2\, d^2\mathbf{p}_1\, d^2\mathbf{p}_2 \qquad (3.84)$$

where

$$B(\mathbf{q}_1,\mathbf{q}_2,\mathbf{p}_1,\mathbf{p}_2) = \left\langle V(\mathbf{q}_1,\mathbf{p}_1)V^*(\mathbf{q}_2,\mathbf{p}_2) \right\rangle \qquad (3.85)$$

is the target scattering function ($\text{m}^{-4}\cdot\text{sr}^{-1}$) and

$$K(R) = \exp\left[-\int_0^R \alpha(z)dz \right] \qquad (3.86)$$

is the dimensionless irradiance extinction, and $\alpha(z)$ (m^{-1}) is the linear extinction coefficient along the propagation paths. In writing Eq. (3.84) it is assumed that in each propagation path (transmit and BPLO) the Fresnel approximation is valid.

3.4.3.1 Point Scatterer

The scattering coefficient for a point scatterer (simple glint) at location $\mathbf{p}$ is given by [84]

$$V(\mathbf{p}_1,\mathbf{q}_1) = \lambda\sqrt{\sigma_s}\,\exp(i\theta)\delta(\mathbf{q}_1-\mathbf{p})\delta(\mathbf{p}_1-\mathbf{p}) \qquad (3.87)$$

and the target scattering function is

$$B(\mathbf{q}_1,\mathbf{q}_2,\mathbf{p}_1,\mathbf{p}_2) = \lambda^2\sigma_s\delta(\mathbf{p}_1-\mathbf{p})\delta(\mathbf{p}_2-\mathbf{p})\delta(\mathbf{q}_1-\mathbf{p})\delta(\mathbf{q}_2-\mathbf{p}) \qquad (3.88)$$

where θ is the phase of the scattered field, σ_S (m²·sr⁻¹) is the scattering cross section of the point scatterer, and $\delta(\mathbf{p})$ (m⁻²) is the 2-d vector delta function. Inserting Eq. (3.88) into Eq. (3.84), the target plane SNR becomes

$$\text{SNR}(\mathbf{p},t) = \frac{\lambda^2 \sigma_S \, \text{K}(R_T) \, \text{K}(R_R)}{h\nu B_w \langle P_{LOD} \rangle} \big\langle J_T(\mathbf{p}, R_T, t - R_T/c) \, J_{BPLO}(\mathbf{p}, R_R) \big\rangle \qquad (3.89)$$

where

$$J_T(\mathbf{p}, R_T, t) = \big| E_T(\mathbf{p}, R_T, t) \big|^2 \quad \text{and} \quad J_{BPLO}(\mathbf{p}, R_R) = \big| E_{BPLO}(\mathbf{p}, R_R) \big|^2 \qquad (3.90)$$

are the irradiance profiles (W·m⁻²) of the transmitted and back-propagated LO fields in the absence of extinction.

3.4.3.2 Distributed Aerosol

For a distributed aerosol target, the phase of the scattered field for each particle is random and the mutual coherence function [Eq. (3.71)] of the total scattered field is the sum of the mutual coherence functions from each particle. The target scattering function for a single aerosol particle is the same as the scattering function for a point scatterer. The SNR for a distributed aerosol target is obtained by integrating Eq. (3.89) over all of the scattering aerosols,

$$\text{SNR}(t) = \frac{\lambda^2}{h\nu B_w \langle P_{LOD} \rangle} \int_{-R_T}^{\infty} \int_{-\infty}^{\infty} \text{K}^2(z_p) \beta(\mathbf{p}, z_p, \theta_S)$$

$$\times \big\langle J_T(\mathbf{p}, z_t, t - z_t/c) J_{BPLO}(\mathbf{p}, z_r) \big\rangle d^2\mathbf{p}\, dz_p \qquad (3.91)$$

where $K^2(z_p)$ represents the atmospheric extinction along each path (which is normally considered to be constant over the scattering volume), z_p is range along the z-axis of the target coordinate system ($z_p = 0$ implies $z_t = R_T$), z_t and z_r are functions of z_p, as defined in Eqs. (3.1) and (3.4),

$$\beta(\mathbf{p}, z_p, \theta_S) = \int_0^\infty \sigma_S(\theta_S) N(\sigma_S; \mathbf{p}, z_p) d\sigma_S \qquad (3.92)$$

is the total volume scattering coefficient ($m^{-1} \cdot sr^{-1}$) at wavelength λ, $N(\sigma_S; \mathbf{p}, z_p)$ ($m^{-5} \cdot sr$) is the number density of aerosols per unit volume per unit σ_s at location ($\mathbf{p}, z_p$), and θ_S is the bistatic angle [see *Figure 3-3*]. For laser beams with relatively small transverse extent and typical atmospheric conditions, $\beta(\mathbf{p}, z_p, \theta_S)$ and $N(\sigma_S; \mathbf{p}, z_p)$ may be assumed to be functions of range only. In Equation(3.91) it should be noted that R_T and R_R are both functions of z_p, the range measured with respect to the target coordinate system [see Eq. (3.1)].

In the next section, the general results given above are applied to the specific case of an infinite uniform detector. The infinite uniform detector case will be valid when the detector is large compared to the LO field.

3.5 Signal-to-Noise Ratio: Infinite Uniform Detector

From this section on, the coherent lidar performance will be expressed in terms of the normalized fields defined by

$$E_L(\mathbf{u},z,t) = \sqrt{\langle P_L(t) \rangle} e_L(\mathbf{u},z,t)$$

and

$$E_{LO}(\mathbf{v},z) = \sqrt{\langle P_{LO} \rangle} e_{LO}(\mathbf{v},z) \qquad (3.93)$$

where P_{LO} (W) is the LO total power and $e_L(\mathbf{u}, z, t)$ (m^{-1}) and $e_{LO}(\mathbf{v}, z)$ (m^{-1}) are the

normalized fields for the transmitter and the LO field respectively. This normalization is

used because the coherent lidar performance can now be referenced to the average laser

power, $\langle P_L(t) \rangle$, instead of the average transmitted power, $\langle P_T(t) \rangle$. It should be noted

that the time dependence indicated in $e_L(\mathbf{u}, z, t)$ is the spatial variation of the laser field as

a function of time. Such a variation could be manifested by the interference of spatial

modes. It is generally assumed that the spatial characteristics of the laser field do not

vary with time, or change slowly with respect to the observation time.

For a uniform detector (η_Q constant over surface) that collects all energy from the

LO and the scattered field, the Fourier transform of the detector response is [see Eq.

(3.80)]

$$Y(\mathbf{\kappa}) = \eta_Q \delta(\mathbf{\kappa}). \qquad (3.94)$$

Substitution of Eq. (3.94) into Eq. (3.79) yields

$$E_{BPLO} = \eta_Q E_{LO}^*(\mathbf{v},0) W_R(\mathbf{v}) \qquad (3.95)$$

and the average LO power detected [Eq. (3.68)] becomes

$$\langle P_{LOD} \rangle = \eta_Q \langle P_{LO} \rangle. \qquad (3.96)$$

At the exit of the transmitter and receiver, respectively, the normalized fields are defined

as

$$e_T(\mathbf{u},0,t) = e_L(\mathbf{u},0,t) W_T(\mathbf{u})$$

and

$$e_{BPLO}(\mathbf{v},0) = e_{LO}^*(\mathbf{v},0) W_R(\mathbf{v}). \tag{3.97}$$

3.5.1 Point Scatterer

Using the normalized fields defined above as well as Eq. (3.89), the target plane

representation of the SNR for a point scatterer at $(\mathbf{p}, z_p)$ can be written as

$$\text{SNR}(\mathbf{p}, z_p, t) = \frac{\eta_Q \left\langle P_L(t - z_t/c) \right\rangle K^2(z_p) \sigma_s}{h\nu B_w} c(\mathbf{p}, z_p, t) \tag{3.98}$$

where

$$c(\mathbf{p}, z_p, t) = \lambda^2 \left\langle j_T(\mathbf{p}, z_t, t - z_t/c) j_{BPLO}(\mathbf{p}, z_r) \right\rangle \tag{3.99}$$

is the target plane representation of the coherent responsivity density (m^{-2}) and

$$j_T(\mathbf{p}, z_t, t) = |e_T(\mathbf{p}, z_t, t)|^2, \text{ and } \quad j_{BPLO}(\mathbf{p}, z_r) = |e_{BPLO}(\mathbf{p}, z_r)|^2 \tag{3.100}$$

are the random irradiance profiles (m^{-2}) of the normalized transmitter and BPLO fields at

the target. Again, note that the z_t and z_r are functions of z_p, repeated here for

convenience:

$$z_t = z_p + R_T \quad \text{and} \quad z_r = -x_p \sin\theta_S + z_p \cos\theta_S + R_R. \tag{3.101}$$

The average fraction of the power transmitted through the transmit aperture defined by

$W_L(\mathbf{u})$ is given by

$$T_T(t) = \int_{-\infty}^{\infty} \left\langle j_T(\mathbf{u},0,t) \right\rangle d^2\mathbf{u} = \left\langle \frac{P_T(t)}{P_L(t)} \right\rangle. \tag{3.102}$$

Likewise, for an infinite, uniform detector, the average fraction of LO power that would

be transmitted through the reciprocal receiver defined by $W_R(\mathbf{v})$ is

$$T_R = \int_{-\infty}^{\infty} \langle j_{BPLO}(\mathbf{v},0) \rangle d^2\mathbf{v} . \tag{3.103}$$

Recall from Eq. (3.75) that the SNR can be expressed in terms of the average

power collected by the detector and the heterodyne efficiency. The average direct

detection power for a point scatterer [see Eq. (3.69)] is given by

$$\langle P_D(t) \rangle = \eta_Q \langle P_L(t - z_t/c) \rangle K^2(z_p)\sigma_s d(\mathbf{p},z_p,t) \tag{3.104}$$

where

$$d(\mathbf{p},z_p,t) = \lambda^2 \langle j_T(\mathbf{p},z_t,t - z_t/c) j_R(\mathbf{p},z_r) \rangle \tag{3.105}$$

is the target plane representation of the direct responsivity density (m^{-2}) and

$$j_R(\mathbf{p},z_r) = \int_{-\infty}^{\infty} |W_R(\mathbf{v})|^2 G(\mathbf{p};\mathbf{v},z_r) G^*(\mathbf{p};\mathbf{v},z_r) d^2\mathbf{v} \tag{3.106}$$

is the random irradiance profile (m^{-2}) of a normalized spatially incoherent source defined

by the receiver aperture $|W_R(\mathbf{v})|^2$. The heterodyne efficiency [Eq. (3.74)] for a point

scatterer is

$$\eta_Q(\mathbf{p},z_p,t) = \frac{c(\mathbf{p},z_p,t)}{d(\mathbf{p},z_p,t)} \tag{3.107}$$

or in words, the fraction of direct (incoherent) detection power converted to coherent

(heterodyne) detection power.

It should be noted that this representation of direct responsivity density (and

therefore, heterodyne efficiency) will only be valid in the matched monostatic limit. The

direct responsivity density is a measure of the direct detection power. The total scattering volume in a matched monostatic system is defined by either the transmit beam profile or the imagined BPLO profile; therefore, the direct detection power can be found by integrating over the BPLO profile. In the bistatic configuration, the direct detection power is defined as the overlap of the scattering volume (in this case a column), with the target plane image of the detector surface. Thus, in order to compute the direct detection power for a bistatic system, the specific receiver design characteristics (detector size, focal length, etc.) must be known. For this reason, the heterodyne efficiency will only be computed for the monostatic for comparison with previous results.

3.5.2 Infinite Uniform Aerosol

For an infinite uniform aerosol target, the volume scattering coefficient will be a function of range only; over the transverse dimensions of the transmit beam, β is considered to be uniform and $\beta(\mathbf{p}, z_p, \theta_S) = \beta(z_p, \theta_S)$. The range dependence of $\beta(z_p, \theta_S)$ is due to the dependence of aerosol properties, such as density, index of refraction, and size distribution, on altitude. Similar to the expression in Section 3.4.3.2, the SNR for an infinite uniform aerosol is the sum of the SNR for each individual aerosol particle (all point scatterers),

$$\text{SNR}(t) = \frac{\eta_Q}{h\nu B_w} \int_{-R_T}^{\infty} K^2(z_p) \left\langle P_L\left(t - z_t/c\right)\right\rangle \beta(z_p, \theta_S) C(z_p, t) dz_p \qquad (3.108)$$

where

$$C(z_p, t) = \lambda^2 \int_{-\infty}^{\infty} \langle j_T(\mathbf{p}, z_t, t - z_t/c) j_{BPLO}(\mathbf{p}, z_r) \rangle \mathrm{d}^2 \mathbf{p} \qquad (3.109)$$

is the target plane representation of the dimensionless coherent responsivity (integrate $c(\mathbf{p}, z_p, t)$ over $\mathbf{p}$), and the explicit dependence of z_t and z_r on z_p is again, omitted.

The average direct detection power is

$$\langle P_D(t) \rangle = \eta_Q \int_{-R_T}^{\infty} K^2(z_p) \langle P_L(t - z_t/c) \rangle \beta(z_p) D(z_p, t) \mathrm{d}z_p \qquad (3.110)$$

where

$$D(z_p, t) = \lambda^2 \int_{-\infty}^{\infty} \langle j_T(\mathbf{p}, z_t, t - z_t/c) j_R(\mathbf{p}, z_r) \rangle \mathrm{d}^2 \mathbf{p} \qquad (3.111)$$

is the target plane representation of the dimensionless direct responsivity (integrate $d(\mathbf{p}, z_p, t)$ over $\mathbf{p}$). The heterodyne efficiency is given as

$$\eta_H(t) = \frac{\displaystyle\int_{-R_T}^{\infty} K^2(z_p) \langle P_L(t - z_t/c) \rangle \beta(z_p) C(z_p, t) \mathrm{d}z_p}{\displaystyle\int_{-R_T}^{\infty} K^2(z_p) \langle P_L(t - z_t/c) \rangle \beta(z_p) D(z_p, t) \mathrm{d}z_p}. \qquad (3.112)$$

Again, for the bistatic case, the integral in the denominator must be evaluated over the extent of the target plane image of the detector and not the area defined by the BPLO. This fact makes the evaluation of the heterodyne efficiency a system specific problem, but does not change the analysis of coherent responsivity or SNR.

In the next section, the effects of refractive turbulence are considered. The refractive turbulence effects are accounted for with the transverse field coherence length,

ρ_0. The results presented in the next section have been published extensively are presented for completeness.

3.6 Refractive Turbulence Effects

The primary effect of refractive turbulence is a degradation of the spatial correlation of the transmitted and scattered waves. This spatial decorrelation of the waves results in an overall reduction in the coherent signal power, which has been experimentally demonstrated by Chan *et. al.* [86].

The refractive turbulence effects are accounted for by the fourth moment of the Green's function for propagation in inhomogeneous media,

$$\Gamma_4(\mathbf{p};\mathbf{u}_1,\mathbf{u}_2,\mathbf{v}_1,\mathbf{v}_2,z_t,z_r) = \left\langle G(\mathbf{p};\mathbf{u}_1,z_t)G^*(\mathbf{p};\mathbf{u}_2,z_t)G(\mathbf{p};\mathbf{v}_1,z_r)G^*(\mathbf{p};\mathbf{v}_2,z_r)\right\rangle. \quad (3.113)$$

When the angular deviation of propagating waves due to refractive turbulence is small, the Green's function is given by a Feynman path integral [32, 87, 88]. If the temporal variations of the fields with propagation distance is slow, the Markov approximation is valid [89]. Under the Markov approximation, refractive turbulence behaves as an uncorrelated process in the propagation direction for the moment of interest. Under the above conditions, the fourth moment Green's function may be expressed as a series [87]. In the bistatic case, the fourth moment Green's function reduces to two second moment Green's function because of independent paths. With the above conditions the fourth moment of the Green's function is given by

$$\Gamma_4 = \left\langle G(\mathbf{p};\mathbf{u}_1,z_t)G^*(\mathbf{p};\mathbf{u}_2,z_t) \right\rangle \left\langle G(\mathbf{p};\mathbf{v}_1,z_r)G^*(\mathbf{p};\mathbf{v}_2,z_r) \right\rangle \qquad (3.114)$$

with

$$\left\langle G(\mathbf{p}_1;\mathbf{u}_1,R)G^*(\mathbf{p}_2;\mathbf{u}_2,R) \right\rangle = \frac{k^2}{(2\pi R)^2} \exp\left\{ \frac{ik}{2R} \left[(\mathbf{p}_1 - \mathbf{u}_1)^2 - (\mathbf{p}_2 - \mathbf{u}_2)^2 \right] \right\}$$

$$\times \exp\left\{ -\frac{1}{2} \int_0^R D'\left[(\mathbf{u}_1 - \mathbf{u}_2)\left(1 - \frac{z}{R} \right) + (\mathbf{p}_1 - \mathbf{p}_2)\frac{z}{R}, z \right] dz \right\}, \qquad (3.115)$$

where

$$D'[\mathbf{x},z] = 4\pi k^2 \int_{-\infty}^{\infty} [1 - \cos(\mathbf{\kappa} \cdot \mathbf{x})] \Phi_n(\mathbf{\kappa},\kappa_z = 0, z) d^2\kappa \qquad (3.116)$$

is the structure function density (m^{-1}), $\Phi_n(\mathbf{\kappa}, \kappa_z, z)$ (m^3) is the local 3-dimensional

spectrum of the refractive index fluctuations at range z, an $\mathbf{\kappa}$ (rad·m^{-1}) is the spatial wave

vector.

The atmospheric refractive index fluctuations can be modeled with the

Kolmogorov spectrum [84] in which case [90]

$$\int_0^R D'\left[(\mathbf{u}_1 - \mathbf{u}_2)(1 - z/R), z \right] dz = \left(\frac{|\mathbf{u}_1 - \mathbf{u}_2|}{\rho_o(R)} \right)^{5/3}, \qquad (3.117)$$

where

$$\rho_o(R) = \left[2.91438 k^2 \int_0^R C_n^2(z)(1 - z/R)^{5/3} dz \right]^{-3/5} \qquad (3.118)$$

is the transverse field coherence length (m) of a point source located at a range R, and

$C_n^2(z)$ ($m^{-2/3}$) is the refractive index structure constant at range z. Replacing the 5/3

power with 2 in Eq. (3.117) is a useful approximation that produces little error [25]. This

square law structure function approximation is equivalent to assuming the refractive

turbulence effects are characterized by random wedges that produce only wavefront tilt

[91]. In the limit of small apertures, this approximation is very precise.

Chapter 4

RESULTS

The signal-to-noise ratio (SNR) results presented in Chapter 3 are completely general for any multistatic or bistatic coherent lidar system. In this section the results of applying specific system parameters to the performance equations derived in Chapter 3 are presented. In order to obtain closed form expressions, a lidar system with untruncated Gaussian fields and apertures is assumed. With the general expressions derived for a Gaussian lidar system, the scattering coefficient is calculated using Mie theory. Next, the refractive turbulence effects are presented. The general Gaussian lidar expressions are then applied to specific geometry configurations. The chapter concludes with a look at the estimation performance.

4.1 Gaussian Lidar System

To determine the performance of a coherent lidar system, analytic expressions for the SNR, as well as other parameters, are desired. This is best accomplished by describing the main components of the coherent lidar as untruncated complex Gaussian functions. This representation allows analytic solutions and contains all of the physics of the system. In the following calculations, we have also assumed that the transmitter and local oscillator (LO) fields are deterministic, the detector response is uniform

$[\eta_Q(\mathbf{w}) = \eta_Q]$, the detector collects all of the incident LO and scattered power (infinite detector), and the transmitted and scattered fields propagate along independent paths. It has been shown that the independent path assumption is valid when the baseline separation is larger than the aperture size [33], which is the case for a practical multistatic system. The results that follow are a generalization to those presented by Frehlich [32] to include large angle bistatic coherent lidar systems.

The laser field at a plane defined by $z_t = 0$ (just prior to the lens) is described as an untruncated Gaussian

$$e_L(\mathbf{u},0,t) = \frac{1}{\sigma_L\sqrt{\pi}} \exp\left[-\frac{u^2}{2\sigma_L^2} - \frac{iku^2}{2F_L} \right], \tag{4.1}$$

where u^2 is $\mathbf{u}\cdot\mathbf{u}$, σ_L (m) is the $1/e$ intensity radius of the laser beam, and F_L (m) is the phase curvature of the laser beam ($F_L > 0$ if focused at positive distance z). The $1/e^2$ intensity radius is given by $2\sqrt{2}\,\sigma_L$. The truncation effects by an aperture may be neglected if the physical aperture size is greater than $4\sqrt{2}\,\sigma_L$ [92]. If the aperture size is equal to σ_L, 63% of the beam power is transmitted; if the aperture size is equal to $1.5\sqrt{2}\,\sigma_L$, 99% of the laser beam power is transmitted.

The transmitter lens response for a scalar field is also described with an untruncated Gaussian function. This lens function is given by

$$W_T(\mathbf{u}) = \exp\left[-\frac{u^2}{2\sigma_T^2} - \frac{iku^2}{2F_T} \right], \tag{4.2}$$

where σ_T (m) is the $1/e$ intensity radius of the transmitter lens and F_T (m) is the phase curvature of the transmit lens ($F_T > 0$ for focusing lens). While this representation is not

realistic for a circular aperture, it allows analytic solutions while preserving a size parameter for the lens. Using Eqs. (4.1) and (4.2), the normalized field at the exit of the lens can be written as [see Eq. (3.97)]

$$e_T(\mathbf{u},0) = \frac{1}{\sigma_L\sqrt{\pi}}\exp\left[-\frac{u^2}{2\sigma_{TE}^2} - \frac{iku^2}{2F_{TE}}\right],$$ (4.3)

with

$$\frac{1}{\sigma_{TE}^2} = \frac{1}{\sigma_L^2} + \frac{1}{\sigma_T^2},$$ (4.4)

where σ_{TE} (m) is the $1/e$ intensity radius of the transmitted field, and with

$$\frac{1}{F_{TE}} = \frac{1}{F_L} + \frac{1}{F_T},$$ (4.5)

where F_{TE} (m) is the phase curvature of the transmitted beam. Inserting Eq. (4.3) into Eq. (3.100), the average irradiance of the normalized transmitter field (with respect to the transmitter referenced coordinate system) at the target plane becomes

$$\langle j_T(x_t, y_t, z_t) \rangle = \frac{\sigma_{TE}^2}{\pi\sigma_L^2\sigma_{BT}^2(z_t)}\exp\left[\frac{x_t^2 + y_t^2}{\sigma_{BT}^2(z_t)}\right],$$ (4.6)

where

$$\sigma_{BT}^2(z_t) = \sigma_{TE}^2\left(1 - \frac{z_t}{F_{TE}}\right)^2 + \frac{z_t^2}{k^2\sigma_{TE}^2} + \frac{2z_t^2}{k^2\rho_o^2(z_t)}.$$ (4.7)

In words, the average normalized irradiance of the transmitted field in the target plane has a Gaussian profile with a $1/e$ radius of σ_{BT} (m). In deriving Eq. (4.6), a square law structure function is used, replacing 5/3 with 2 in Eq. (3.117). The derivation of Eq. (4.6) is included in Appendix A.

The receiver lens and LO fields are described in a manner very similar to that of the transmitter lens and transmitted field. The receiver lens response function for the scalar field is given by

$$W_R(\mathbf{v}) = \exp\left[-\frac{v^2}{2\sigma_R^2} - \frac{ikv^2}{2F_R}\right], \tag{4.8}$$

where σ_R (m) is the $1/e$ intensity radius of the receiver lens, and F_R (m) is the focal length of the receiver lens or telescope. It is important to note that although actual lidar systems usually use a rectangular top hat receiver function (circular aperture), the Gaussian assumption allows analytically tractable results without ignoring the physical size parameters of the receiver. Gaussian profile truncation by the receiver is included unless we let $\sigma_R \rightarrow \infty$, in which case there is no receiver truncation. The same comments apply to the transmitter lens function.

The LO at the receiver plane ($z_R = 0$) is given by (untruncated Gaussian)

$$e_{LO}(\mathbf{v},0) = \frac{1}{\sigma_{LO}\sqrt{\pi}}\exp\left[-\frac{v^2}{2\sigma_{LO}^2} - \frac{ikv^2}{2F_{LO}}\right] \tag{4.9}$$

where σ_{LO} (m) is the $1/e$ intensity radius of the LO beam, and F_{LO} (m) is the phase curvature of the LO beam ($F_{LO} > 0$ indicates a beam waist on the detector side of the receiver). The normalized field of the back-propagated local oscillator (BPLO) beam is [see Eq. (3.97)]

$$e_{BPLO}(\mathbf{v},0) = \frac{1}{\sigma_{LO}\sqrt{\pi}}\exp\left[-\frac{v^2}{2\sigma_{RE}^2} - \frac{ikv^2}{2F_{RE}}\right] \tag{4.10}$$

where

$$\frac{1}{\sigma_{RE}^2} = \frac{1}{\sigma_R^2} + \frac{1}{\sigma_{LO}^2}, \tag{4.11}$$

and

$$\frac{1}{F_{RE}} = \frac{1}{F_R} - \frac{1}{F_{LO}}. \tag{4.12}$$

Inserting Eq. (4.10) into Eq. (3.100), the ensemble average of the normalized BPLO

irradiance (with respect to the receiver referenced coordinate system) in the target plane

becomes

$$\left\langle j_{BPLO}(x_r, y_r, z_r) \right\rangle = \frac{\sigma_{RE}^2}{\pi \sigma_{LO}^2 \sigma_{BR}^2(z_r)} \exp\left[\frac{x_r^2 + y_r^2}{\sigma_{BR}^2(z_r)}\right], \tag{4.13}$$

where

$$\sigma_{BR}^2(z_r) = \sigma_{RE}^2 \left(1 - \frac{z_r}{F_{RE}}\right)^2 + \frac{z_r^2}{k^2 \sigma_{RE}^2} + \frac{2z_r^2}{k^2 \rho_o^2(z_r)}, \tag{4.14}$$

and σ_{BR} (m) is the $1/e$ intensity radius of the virtual BPLO in the target plane. The

transmitter and reciprocal receiver truncation ratios are [see Eqs. (3.102) and (3.103)]

$$T_T = \frac{\sigma_{TE}^2}{\sigma_L^2}, \quad \text{and} \quad T_R = \frac{\sigma_{RE}^2}{\sigma_{LO}^2}. \tag{4.15}$$

In order to perform the target plane integration, the transmitter and receiver

referenced coordinates must be transformed to the target plane coordinates. Inserting

Eqs. (3.1) and (3.4) into Eqs. (4.6) and (4.13), the target plane representation of the

normalized transmitter and BPLO irradiance profiles (with respect to the target referenced

coordinate system) are

$$\langle j_T(x_p, y_p, z_p, R_T) \rangle = \frac{T_T}{\pi \sigma_{BT}^2(z_p, R_T)} \exp\left[-\frac{x_p^2 + y_p^2}{\sigma_{BT}^2(z_p, R_T)}\right] \qquad (4.16)$$

and

$$\langle j_{BPLO}(x_p, y_p, z_p, R_R) \rangle = \frac{T_R}{\pi \sigma_{BR}^2(x_p, z_p, R_R)}$$

$$\times \exp\left[-\frac{\left(x_p \cos\theta_S + z_p \sin\theta_S\right)^2 + y_p^2}{\sigma_{BR}^2(x_p, z_p, R_R)}\right], \qquad (4.17)$$

where

$$\sigma_{BT}^2(z_p, R_T) = \sigma_{TE}^2\left(1 - \frac{z_p + R_T}{F_{TE}}\right)^2 + \frac{\left(z_p + R_T\right)^2}{k^2\sigma_{TE}^2} + \frac{2\left(z_p + R_T\right)^2}{k^2\rho_{oT}^2}$$

$$\approx \sigma_{TE}^2\left(1 - \frac{R_T}{F_{TE}}\right)^2 + \frac{R_T^2}{k^2\sigma_{TE}^2} + \frac{2R_T^2}{k^2\rho_o^2(R_T)}, \qquad (4.18)$$

and

$$\sigma_{BR}^2(x_p, z_p, R_R) = \sigma_{RE}^2\left(1 - \frac{-x_p \sin\theta_S + z_p \cos\theta_S + R_R}{F_{RE}}\right)^2$$

$$+ \frac{\left(-x_p \sin\theta_S + z_p \cos\theta_S + R_R\right)^2}{k^2\sigma_{RE}^2}$$

$$+ \frac{2\left(-x_p \sin\theta_S + z_p \cos\theta_S + R_R\right)^2}{k^2\rho_{oR}^2}$$

$$\approx \sigma_{RE}^2\left(1 - \frac{R_R}{F_{RE}}\right)^2 + \frac{R_R^2}{k^2\sigma_{RE}^2} + \frac{2R_R^2}{k^2\rho_o^2(R_R)}, \qquad (4.19)$$

and ρ_{oR} and ρ_{oT} are the transverse field coherence lengths as viewed by the receiver and transmitter, respectively. The approximate expressions in Eqs. (4.18) and (4.19) are the zero order terms in a Taylor series expansion about $x_p = y_p = z_p = 0$. This approximation

is equivalent to assuming that the 1/e radii do not change significantly within the overlap of the transmit beam and imagined BPLO beam. This is valid for small scattering volumes, which is shown to be the case for this problem.

Inserting Eqs. (4.15) – (4.17) into Eq. (3.109), and using the first order approximations in Eqs. (4.18) and (4.19), the coherent responsivity becomes

$$C(z_p,R_T,R_R) = \frac{\lambda^2 T_T T_R}{\pi\sqrt{\left[\sigma^2_{BRo}(R_T)+\sigma^2_{BTo}(R_R)\right]\left[\sigma^2_{BRo}(R_R)+\sigma^2_{BTo}(R_T)\cos^2\theta_S\right]}}$$

$$\times\exp\left[-z_p^2\left(\frac{\sin^2\theta_S}{\sigma^2_{BRo}(R_R)+\sigma^2_{BTo}(R_T)\cos^2\theta_S}\right)\right] \tag{4.20}$$

where σ_{BTo} and σ_{BRo} indicate the zero order term in the Taylor series expansions [see Eqs. (4.18) and (4.19)]. For the monostatic case, $(R_T = R_R = R$ and $\theta_S = 0)$, Eq. (4.20) reduces to

$$C(R) = \frac{\lambda^2 T_T T_R}{\pi\left[\sigma^2_{BT}(R)+\sigma^2_{BR}(R)\right]}, \tag{4.21}$$

which is identical to the independent path calculation obtained by Frehlich and Kavaya [32].

The temporal pulse profile of the transmitted laser pulse is modeled as an untruncated Gaussian,

$$\langle P_L(t)\rangle = \frac{U_L}{\tau_p\sqrt{\pi}}\exp\left[-\frac{t^2}{\tau_p^2}\right], \tag{4.22}$$

where τ_p (sec) is the $1/e$ pulse width, and U_L (J) is the laser pulse energy. Inserting Eqs. (4.20) and (4.22) into Eq. (3.108) with the assumptions that β and K do not change significantly over the scattering volume i.e.,

$$K^2(z_p) = K(R_T)K(R_R) \text{ and } \beta(z_p, \theta_s) = \beta(R_T, \theta_s), \tag{4.23}$$

the target plane SNR becomes

$$\mathrm{SNR}(R_T, R_R, t) = \frac{U_L \eta_Q K^2(R_T, R_R)\beta(R_T, \theta_s)\lambda^3 T_T T_R}{\pi h B_w \sigma_{eff}^2(R_T, R_R)}$$
$$\times \exp\left[-\frac{(t - R_T/c)^2}{\tau_p^2}\left[1 - \varepsilon(R_T, R_R)\right]\right], \tag{4.24}$$

where

$$\sigma_{eff}^2(R_T, R_R) = \left\{\left[\sigma_{BR}^2(R_R) + \sigma_{BT}^2(R_T)\right]\right.$$
$$\left.\times \left[\tau_p^2 c^2 \sin^2 \theta_s + \sigma_{BR}^2(R_R) + \sigma_{BT}^2(R_T)\cos^2 \theta_s\right]\right\}^{1/2}, \tag{4.25}$$

and

$$\varepsilon(R_T, R_R) = \frac{\sigma_{BR}^2(R_R) + \sigma_{BT}^2(R_T)\cos^2 \theta_s}{\tau_p^2 c^2 \sin^2 \theta_s + \sigma_{BR}^2(R_R) + \sigma_{BT}^2(R_T)\cos^2 \theta_s}. \tag{4.26}$$

For the case of a continuous wave (CW) laser transmitter ($\tau_p \to \infty$), the SNR simplifies to

$$\mathrm{SNR}(R_T, R_R) = \frac{\langle P_L \rangle \eta_Q K^2(R_T, R_R)\beta(R_T, \theta_s)\lambda^2 T_T T_R}{h\nu B_w \sin \theta_S \sqrt{\pi\left[\sigma_{BR}^2(R_R) + \sigma_{BT}^2(R_T)\right]}}, \tag{4.27}$$

where $\langle P_L \rangle$ is the average output power of the CW laser transmitter.

Now that the general expressions for the SNR have been applied to a Gaussian system, the scattering properties of the target (aerosol particles in this case) need to be determined. This is addressed in the next section using Mie scattering theory.

4.2 Volume Scattering Coefficient

Before we can calculate the SNR, the functionality of the volume scattering coefficient, $\beta(z_p, \theta_S)$, must be determined. This is accomplished by assuming spherical scattering particles and using the well known Mie scattering formulas [93, 94]. While the spherical particle assumption may not be well founded, it serves as a good first order approximation for the scattering from aerosol particles. The effects of nonspherical particles on the scattering function is studied by Koepke and Hess [95] and they concluded that; "the scattering functions of the aerosol types continental and urban can be sufficiently calculated with Mie theory." The process of calculating the scattering properties of spherical particles using Mie theory is widely used and is summarized in this section.

For a single spherical particle, the complex scattering amplitudes for the two orthogonal directions of incident polarization are

$$S_1(\mu) = \sum_{n=1}^{\infty} \frac{2n+1}{n(n+1)}\left[a_n \pi_n(\mu) + b_n \tau_n(\mu)\right],$$

$$S_2(\mu) = \sum_{n=1}^{\infty} \frac{2n+1}{n(n+1)}\left[a_n \tau_n(\mu) + b_n \pi_n(\mu)\right], \tag{4.28}$$

where a_n and b_n are the complex valued Mie coefficients, π_n and τ_n are the angular eigenfunctions, and μ is the cosine of the scattering angle (relative to the forward direction), θ. The subscript 1 corresponds to the component of polarization perpendicular to the scattering (or bistatic) plane (s-pol). The subscript 2 corresponds to the component

of polarization parallel to the scattering plane (p-pol). The size parameter, x, is the

particles radius, r (m), times the wavenumber, $x = kr$.

The Mie coefficients depend on the size parameter and the complex index of

refraction, $m = m_{Re} - im_{Im}$, and are given by

$$a_n = \frac{m\psi_n(mx)\psi_n'(x) - \psi_n(x)\psi_n'(mx)}{m\psi_n(mx)\xi_n'(x) - \xi_n(x)\psi_n'(mx)},$$

$$b_n = \frac{\psi_n(mx)\psi_n'(x) - m\psi_n(x)\psi_n'(mx)}{\psi_n(mx)\xi_n'(x) - m\xi_n(x)\psi_n'(mx)}, \qquad (4.29)$$

where $\psi_n(\rho)$ and $\xi_n(\rho)$ are the Riccati-Bessel functions,

$$\psi_n(\rho) = \rho j_n(\rho), \qquad \xi_n(\rho) = \rho h_n^{(1)}(\rho), \qquad (4.30)$$

$j_n(\rho)$ is the spherical Bessel function of the first kind of order n, $h_n^{(1)}(\rho)$ is the spherical

Hankel function of the first kind of order n, and the prime indicates the first derivative

with respect to the argument. The angular eigenfunctions are

$$\pi_n(\mu) = \frac{P_n^1(\mu)}{\sin\theta} = P_n'(\mu),$$

$$\tau_n(\mu) = \frac{dP_n^1(\mu)}{d\theta} = \mu\pi_n(\mu) - (1-\mu^2)\pi_n'(\mu), \qquad (4.31)$$

where P_n^m is the associated Legendre function, which is related to the mth derivative of

the corresponding Legendre polynomial P_n, and the prime again indicates the derivative

with respect to the argument. Care should be taken in evaluating Eq. (4.31) since

definitions for the associated Legendre function and its relationship to the Legendre

polynomial may vary. We have used the same relationship used by Bohren and Huffman

[94, Eq. 4.25], van de Hulst [93, pg. 124], and Ishimaru [96, pg. 338], namely,

$$P_n^m(\mu) = (1-\mu)^{m/2} \frac{d^m P_n(\mu)}{d\mu^m}. \tag{4.32}$$

This relationship varies from that presented by Gradshteyn *et al.* [97, pg. 1025] and Abramowitz *et al.* [98, pg. 334].

The recursion relationships for the angular eigenfunctions are given by

$$\pi_n = \frac{2n-1}{n-1} \mu \pi_{n-1} - \frac{n}{n-1} \pi_{n-2},$$
$$\tau_n = n\mu\pi_n - (n+1)\pi_{n-1}, \tag{4.33}$$

starting with $\pi_0 = 0$ and $\pi_1 = 1$. The scattered intensities (per unit irradiance) are given by

$$i_\perp(\mu) = |S_1(\mu)|^2$$
$$i_\parallel(\mu) = |S_2(\mu)|^2, \tag{4.34}$$

where $\perp$ (perpendicular to scattering plane) corresponds to s-polarized and $\parallel$ (parallel to scattering plane) corresponds to p-polarized incident radiation. There are several algorithms of the above equations for calculating the intensities of Eq. (4.34). For this analysis, the vectorized FORTRAN code developed by Wiscombe [99, 100] is used. *Figure 4-1* is an example plot of the scattering intensities calculated using Mie scattering. The complex index chosen in this example plot represents an approximate index for rural aerosol particles at 80% relative humidity and a wavelength of 1.06 μm [101].

If the number of dielectric spheres with refractive index m and radius in the interval $(r, r + dr)$ is given as $N(r)\, dr$, then the volume scattering coefficients are [102]

$$\beta_{\perp,\parallel}(\theta_s) = \frac{1}{k^2} \int_{r_1}^{r_2} i_{\perp,\parallel}(\theta_s) N(r) dr. \tag{4.35}$$
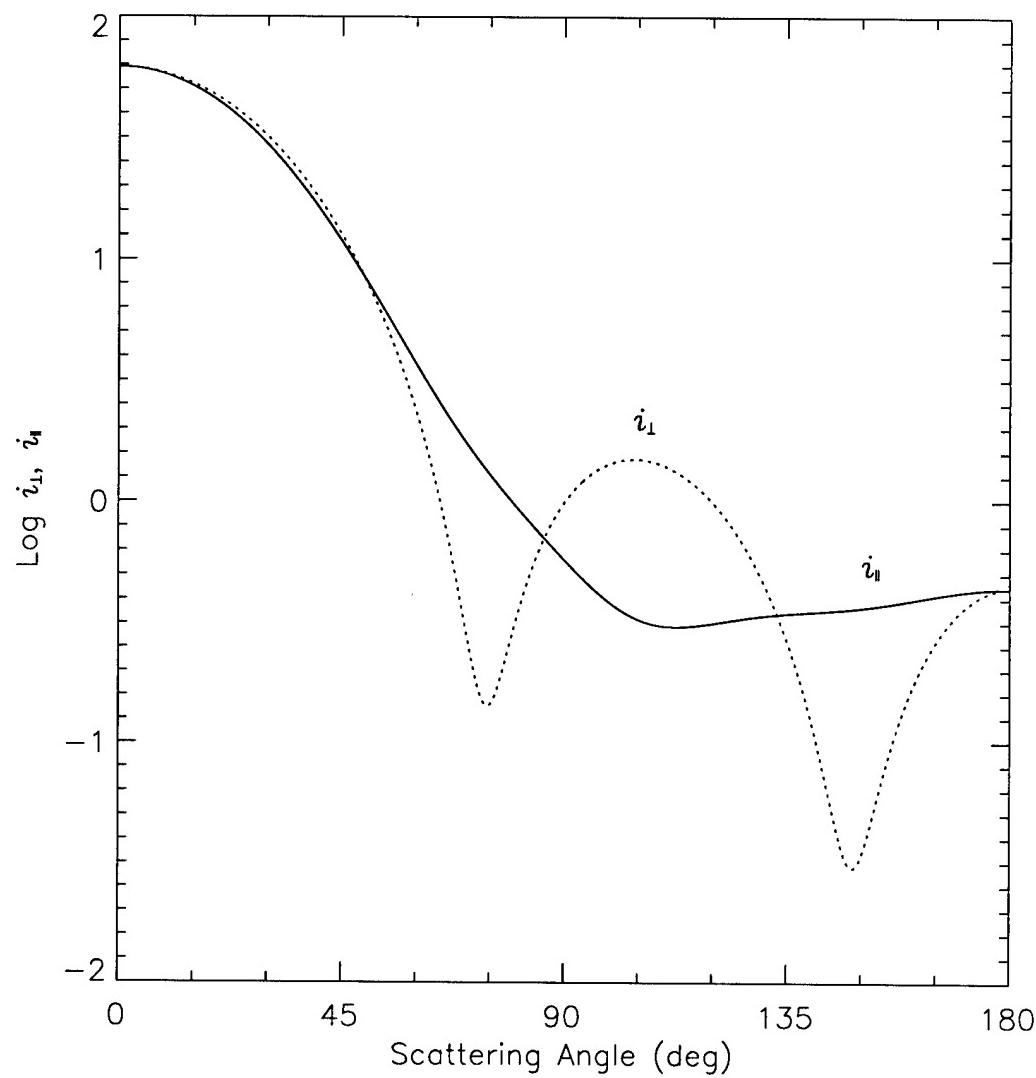
Figure 4-1: Example of scattering intensities calculated using Mie scattering. The size parameter is $x = 3.0$, and the complex index of refraction is $m = 1.42 - i\,0.00692$. The solid line is the p-polarization; the dotted line is the s-polarization.

It is important to note that the scattered intensities have an implicit dependence on wavelength, size parameter, and index of refraction. Also important to note is the difference between the scattering angle, θ, which is measured with respect to the forward direction, and the bistatic angle, θ_S. From *Figure 3-1* it can be seen that $\theta + \theta_S = 180$ degrees [$\mu = \cos(\theta) = -\cos(\theta_S)$].

While this model for β is not entirely accurate, it does provide a good approximation to the angular dependence of aerosol scattering. By using Eq. (4.35), as opposed to Eq. (3.92), we have assumed that the refractive index of all the contributing aerosols is an average effective index of all the scattering particles. A more detailed approach would be to calculate a scattering coefficient for several size distributions (and the respective complex index) and use Eq. (3.92). It is important to note that β is the important engineering parameter for determination of the SNR. In an actual fielded system, an effective β can be estimated from the return signal power. The operation of this system does not require knowledge of the actual aerosol density, scattering cross section, or size distribution.

For most calculations in this thesis, we will use a rural aerosol model (henceforth referred to as model SF-1) described by Shettle and Fenn [101]. Other models considered include a tropospheric model described again by Shettle and Fenn (SF-2), as well as a tropospheric model used by Srivastava *et al.* (SR-1) [103]. Tropospheric aerosol densities can be represented by the sum of log-normal distributions

$$\frac{dN(r)}{dr} = \sum_i \frac{N_i}{r\,\sigma_i \sqrt{2\pi}\,\ln(10)} \exp\left[-\left(\frac{\log r - \log r_i}{\sqrt{2}\,\sigma_i}\right)^2\right] \qquad (4.36)$$

where N_i is the number density of aerosols with mode radius, r_i, and standard deviation

σ_i. The log-normal distribution is also expressed as [95, 103]

$$\frac{dN(r)}{dr} = \sum_i \frac{N_i}{r\,\ln(\overline{\sigma}_i)\sqrt{2\pi}} \exp\left[-\left(\frac{\log r - \log r_i}{\sqrt{2}\,\log(\overline{\sigma}_i)}\right)^2\right], \qquad (4.37)$$

where $\overline{\sigma}_i = \log(\sigma_i)$ is the geometric standard deviation. *Table 4-1* lists the parameters

for the three models discussed above (normalized to 1 particle per unit volume).

Table 4-1: Parameters for the Different Aerosol Distribution Models Considered.

Aerosol Model	Size Distribution		
	N_i	r_i (μm)	σ_i or $\overline{\sigma}_i$
RURAL (SF-1)	0.999875	0.03	$\sigma_i = 0.35$
	0.000125	0.5	$\sigma_i = 0.4$
TROPOSPHERIC (SF-2)	1.0	0.03	$\sigma_i = 0.35$
TROPOSPHERIC (SR-1)	1.0	0.15	$\overline{\sigma}_i = 1.5$

The distributions, normalized to 1 particle per cubic centimeter, are plotted in

Figure 4-2. When calculating the volume scattering coefficient, the limit of integration

over radius will be 0.02 μm to 16.87 μm, this corresponds to size parameters ranging

from 0.1 to 100 for a 1.06 μm wavelength.

The complex refractive index used to calculate the scattered intensities for each

radius ($m = 1.42 - i\,0.00692$) is taken from Shettle and Fenn [101, Table 4] for 80%
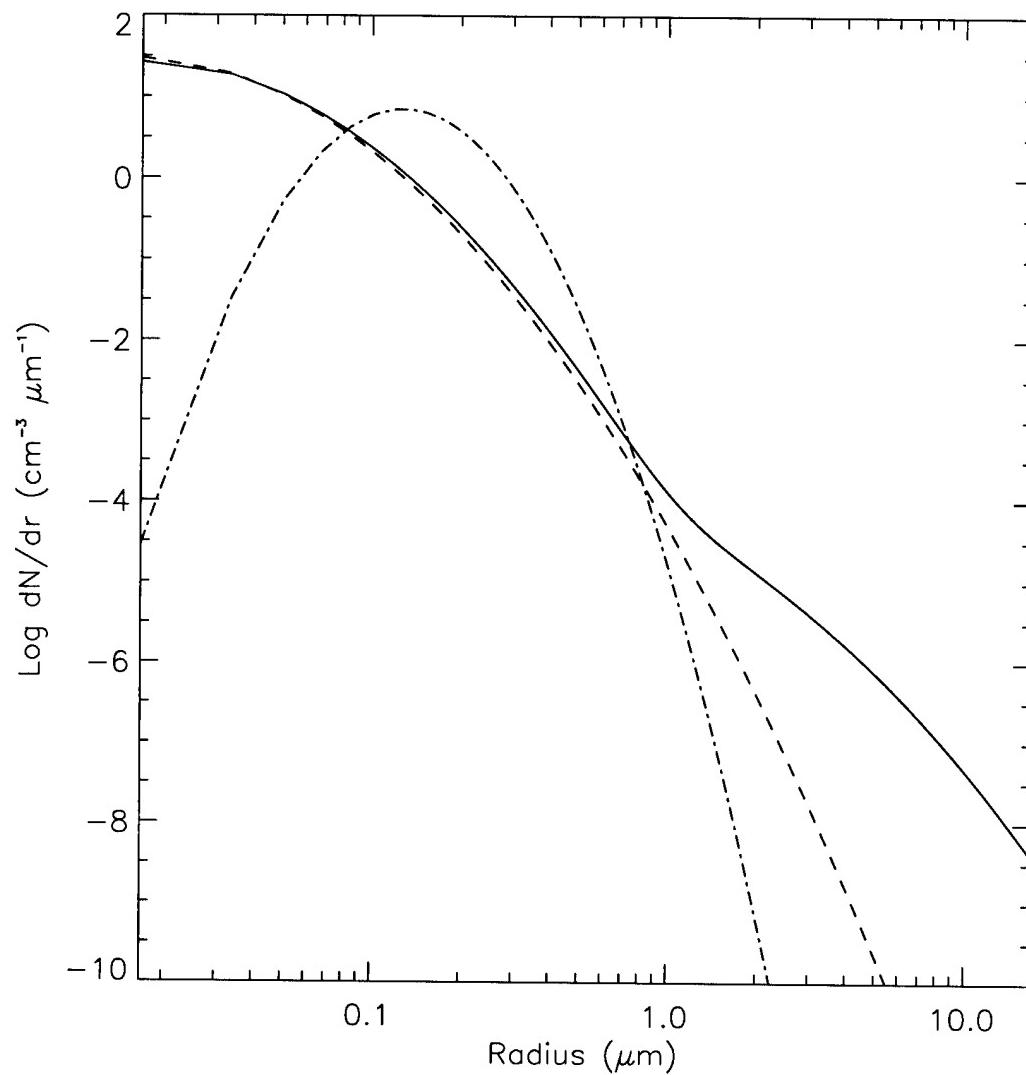
Figure 4-2: Aerosol distribution models used. Rural aerosol model SF-1 (solid); tropospheric aerosol model SF-2 (dashed); tropospheric model from SR-1 (dash-dot). Parameters are as defined in *Table 4-1* and normalized to 1 particle per cm^3.

relative humidity, large rural aerosols, and $\lambda = 1.06 \, \mu m$. The resulting volume scattering

coefficients (for 1 particle per cubic meter) are shown in *Figure 4-3*. The actual volume

scattering coefficient used in the SNR calculations will be the coefficient plotted in

Figure 4-3 multiplied by the aerosol density. As can be seen from this figure, the major

difference in scattering between the three models is approximately a constant scale factor,

aside from the strong forward scattering exhibited by model SF-1. The SF-1 model will

be used as the test case throughout the remainder of this thesis.

The variation of aerosol density with altitude, in reality, will exhibit spatial and

temporal variations, the modeling of which will not be included in this thesis. An

average profile, represented by an exponential, will be used in this analysis. This profile

is given by

$$N_z(z) = N_o \exp\left[-\frac{z}{h}\right], \qquad (4.38)$$

where N_z (cm^{-3}) is the particle concentration, N_o (cm^{-3}) is the concentration at ground

level, z (m) is altitude, and h (m) is the characteristic scale height [104]. Typical values

of h range from 1 km to 1.4 km [16]. An example plot of the aerosol concentration

($h = 1.3$ km) and the resulting volume backscatter coefficient ($\theta = 180°$) is shown in

Figure 4-4.

The next step in applying the SNR expressions to specific configurations is to

determine the refractive turbulence effects. A common way to do this is to compare the

calculated SNR without refractive turbulence to that with refractive turbulence. In the

next section, the analysis of ρ_o is given for a specific C_n^2 model. Because ρ_o depends on
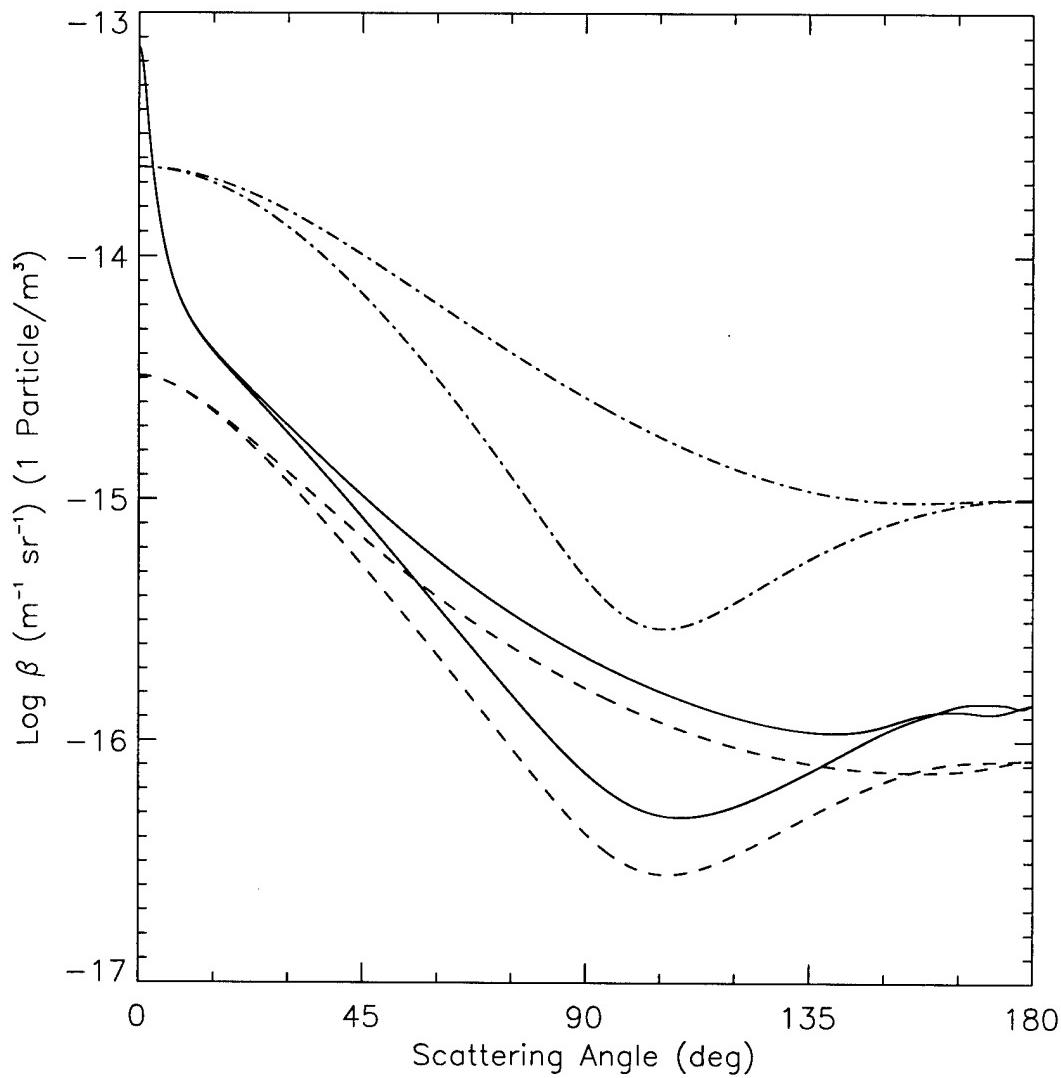
Figure 4-3: Scattering functions for the aerosol distributions used. Rural aerosol model SF-1 (solid); tropospheric aerosol model SF-2 (dashed); tropospheric model SR-1 (dash-dot). Assumes spherical particles with complex refractive index $1.42 - i\,0.00692$. Both the p- and s-polarization components are shown for each model (p-pol shows a dip near 100 degrees).
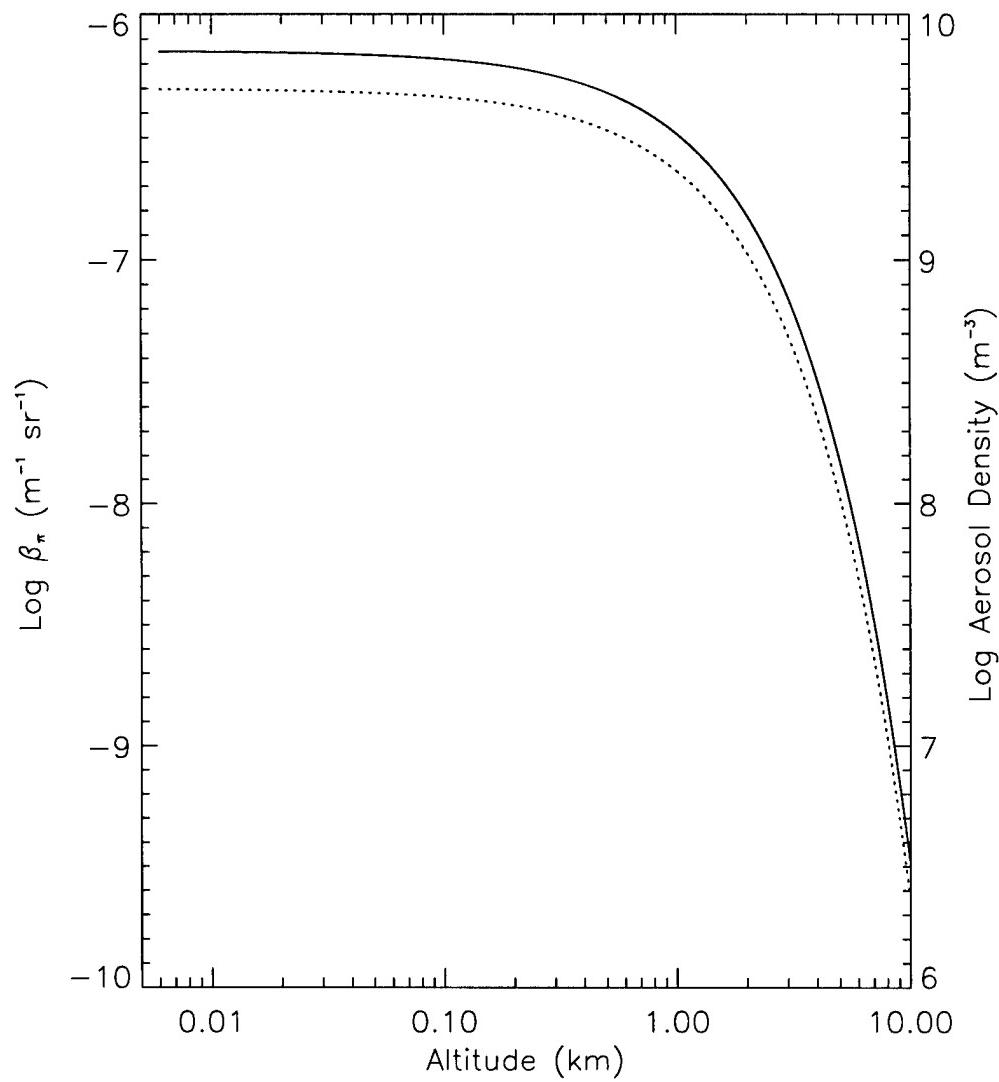
Figure 4-4: Volume backscatter coefficient (solid), and aerosol number density (dotted). Tropospheric size distribution model SF-1; exponential aerosol density profile with $N_o = 5000 \text{ cm}^{-3}$ and $h = 1.3$ km.

the actual propagation path, there will, in general, be different values of ρ_o for each receiver and transmitter. Once ρ_o is calculated, the reduction in SNR due to refractive turbulence is addressed.

4.3 Refractive Turbulence Effects

The general expressions for refractive turbulence effects are detailed in Section 3.6, and are accounted for in the coherent responsivity and SNR with the transverse field coherence length, ρ_o, given by

$$\rho_o(R) = \left[2.91438 k^2 \int_0^R C_n^2(z)(1-z/R)^{5/3} dz \right]^{-3/5}, \qquad (4.39)$$

where $C_n^2(z)$ is the variation of the refractive index structure constant along the path. Since Eq. (4.39) is a path dependent integral, the value of ρ_o will, in general, be different for the transmitter and the receiver paths. If we model the refractive index variations with altitude as

$$C_n^2(z) = C_n^2(z = 1m)z^{-4/3}, \qquad (4.40)$$

then the transverse field coherence length, as viewed from the transmitter is given by

$$\rho_o(R_T) = \left[2.91438 k^2 C_n^2(z = 1m) \int_0^{R_T} \left(z_t \cos\theta_{nt} + 5 \right)^{-4/3} \left(1 - z_t/R_t \right)^{\frac{5}{3}} dz_t \right]^{-3/5}, \qquad (4.41)$$

where the transmitter is arbitrarily placed 5 meters above the ground in order to evaluate the integral in Eq. (4.39). Similarly, for the receiver,

$$\rho_o(R_R) = \left[2.91438\,k^2 C_n^2(z=1\text{m})\int_0^{R_R} \left(z_r \cos\theta_{nr} + 5\right)^{-4/3}\left(1 - z_r/R_r\right)^{5/3} dz_r\right]^{-3/5}, \quad (4.42)$$

and again, the receiver is located 5 meters above the ground. This integral is evaluated

numerically with example results shown in *Figure 4-5* for a vertical path ($\theta_{nt} = 0$) and

different values of $C_n^2(z = 1\text{m})$. *Figure 4-6* shows the effects of propagating along a slant

path defined by the angle θ_{nt}. Typical values of C_n^2 range from 10^{-17} m$^{-2/3}$ for weak

refractive turbulence to 10^{-13} m$^{-2/3}$ for strong refractive turbulence, with 10^{-15} m$^{-2/3}$ often

quoted as a "typical" value [105].

The overall effect of refractive turbulence is a reduction in the SNR. This effect is

quantified by taking the ratio of the SNR with refractive turbulence effects included,

designated SNR_{ρ_o}, to the SNR without refractive turbulence effects, designated

$\text{SNR}_{\rho_o \to \infty}$. The peak SNR, including refractive turbulence effects, can be written as

$$\text{SNR}_{\rho_o} \propto \frac{1}{\sigma_{\text{eff}}^2(R_T, R_R)}, \quad (4.43)$$

where $\sigma_{\text{eff}}^2(R_T, R_R)$ is defined in Eq. (4.25) (with the zero order approximations of σ_{BR}^2

and σ_{BT}^2) and includes the refractive turbulence effects. Define $\hat{\sigma}_{BR}^2(R_R)$ and $\hat{\sigma}_{BT}^2(R_T)$

as the $1/e$ intensity radii of the transmitted and virtual BPLO beams in the target plane

neglecting the effects of refractive turbulence, i.e.

$$\hat{\sigma}_{BR}^2(R_R) \equiv \sigma_{RE}^2\left(1 - \frac{R_R}{F_{RE}}\right)^2 + \frac{R_R^2}{k^2\sigma_{RE}^2},$$

$$\hat{\sigma}_{BT}^2(R_T) \equiv \sigma_{TE}^2\left(1 - \frac{R_T}{F_{TE}}\right)^2 + \frac{R_T^2}{k^2\sigma_{TE}^2}. \quad (4.44)$$
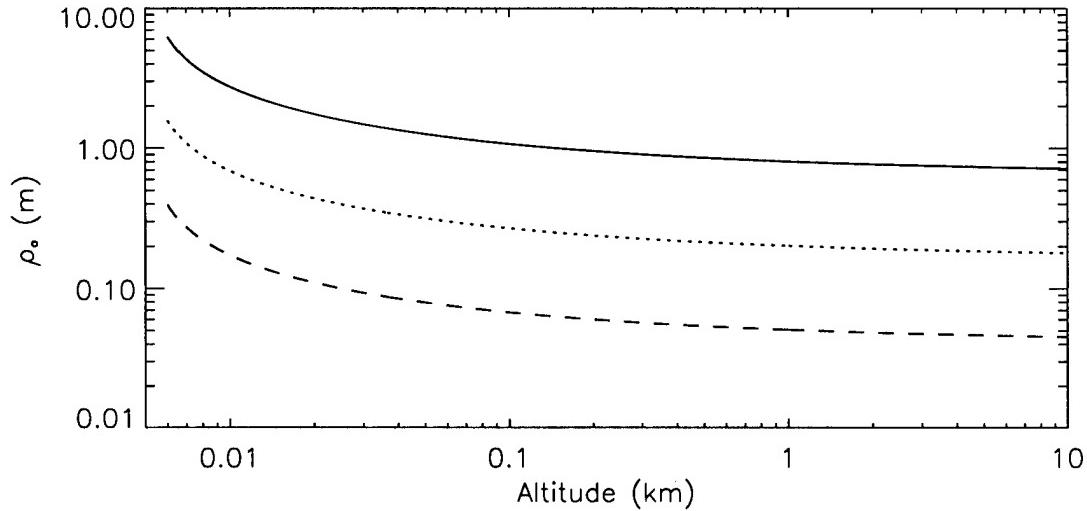
Figure 4-5: Transverse field coherence length for different values of $C_n^2(z = 1\text{m})$ along a vertical path. $C_n^2(z = 1\text{m}) = 1 \times 10^{-14} \text{ m}^{-2/3}$ (solid); $C_n^2(z = 1\text{m}) = 1 \times 10^{-13} \text{ m}^{-2/3}$ (dotted); $C_n^2(z = 1\text{m}) = 1 \times 10^{-12} \text{ m}^{-2/3}$ (dashed).
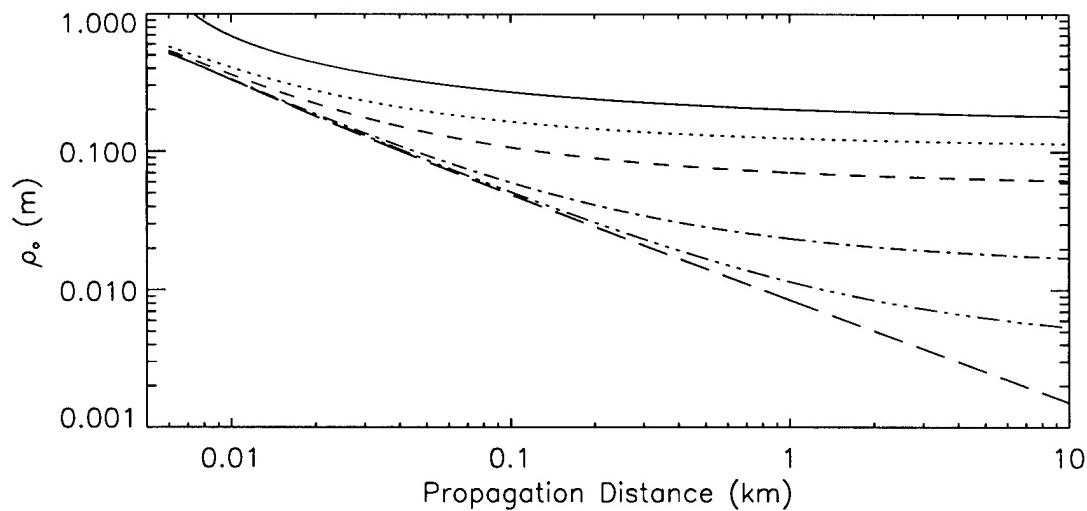
Figure 4-6: Effects of slant path on the transverse field coherence length. Slant angle, θ_{nt}, is measured from vertical and $C_n^2(z = 1\text{m}) = 1 \times 10^{-13} \text{ m}^{-2/3}$. $\theta_{nt} = 0°$ (solid); $\theta_{nt} = 60°$ (dotted); $\theta_{nt} = 80°$ (dashed); $\theta_{nt} = 89°$ (dash-dot); $\theta_{nt} = 89.9°$ (dash-triple dot); $\theta_{nt} = 90°$ (long dash).

Then the SNR reduction factor, F, is given by

$$F_P = \frac{\text{SNR}_{\rho_0}}{\text{SNR}_{\rho_o \to \infty}}$$

$$= \left\{ \frac{\left(\hat{\sigma}_{BR}^2 + \hat{\sigma}_{BT}^2\right)\left[\tau_p^2 c^2 \sin^2 \theta_s + \hat{\sigma}_{BR}^2 + \hat{\sigma}_{BT}^2 \cos^2 \theta_s\right]}{\left(\sigma_{BR}^2 + \sigma_{BT}^2\right)\left[\tau_p^2 c^2 \sin^2 \theta_s + \sigma_{BR}^2 + \sigma_{BT}^2 \cos^2 \theta_s\right]} \right\}^{1/2} \qquad (4.45)$$

for the pulsed case. For the CW case ($\tau_p \to \infty$), the SNR reduction can be expressed as

$$F_{\text{CW}} = \left\{ \frac{\hat{\sigma}_{BR}^2 + \hat{\sigma}_{BT}^2}{\sigma_{BR}^2 + \sigma_{BT}^2} \right\}^{1/2} . \qquad (4.46)$$

The dependencies on R_T and R_R have been omitted for simplicity. Now the SNR including the effects of refractive turbulence, SNR_{ρ_o}, can be expressed as

$$\text{SNR}_{\rho_o} = F_{P,CW} \, \text{SNR}_{\rho_o \to \infty} . \qquad (4.47)$$

If the refractive turbulence effects are small, $F_{P,CW} \approx 1$, and the refractive turbulence will have little effect on the SNR.

Now that all of the specific parameters (other than geometry) have been addressed, the SNR expression can be applied to specific cases. In the next section, the results obtained above are applied to three specific cases as well as the monostatic case for comparison with past results. The only difference between the cases is the geometry.

4.4 Specific Geometry Configurations

The results derived above can be applied to any bistatic (independent path) Gaussian lidar system. In the next section these results are applied to specific geometry

configurations and system parameters. The SNR and the coherent responsivity are evaluated for four different alignments: transmit laser directed vertical and receiver scanned along the beam; transmitter and receiver scanned along a vertical line halfway between the transmitter and receiver; transmit laser directed at 45° from vertical (toward the receiver) and receiver scanned along the beam; and monostatic with transmitter directed vertically, for comparison with previous results. *Table 4-2* gives a description of the test configurations used. Plots of the bistatic angle, θ_S, and β for the three cases, excluding the monostatic case, are shown in *Figure 4-7* and *Figure 4-8*.

Table 4-2: Description of Geometry for Test Cases.

	θ_{nt} (degrees)	θ_{nr} (degrees)	ϕ_t (degrees)	ϕ_r (degrees)
Case 1	0	$-90 \rightarrow 0$ scan	0	0
Case 2	$-\theta_{nr}$	$-90 \rightarrow 0$ scan	0	0
Case 3	45	$-90 \rightarrow 45$ scan	0	0
Monostatic	0	0	0	0

The system parameters used in the calculations are given in *Table 4-3*. For these calculations, it is assumed that the transmit lens and receiver lenses are identical, $\sigma_R = \sigma_T$. For the $1/e$ laser and LO intensity radii, the optimum monostatic truncation values of $0.707 \cdot \sigma_T$ and $0.707 \cdot \sigma_R$ are chosen for simplicity. These optimum values were determined using functional optimization techniques [32, 106]. In all of the test cases, the aerosol distribution model SF-1 is used.
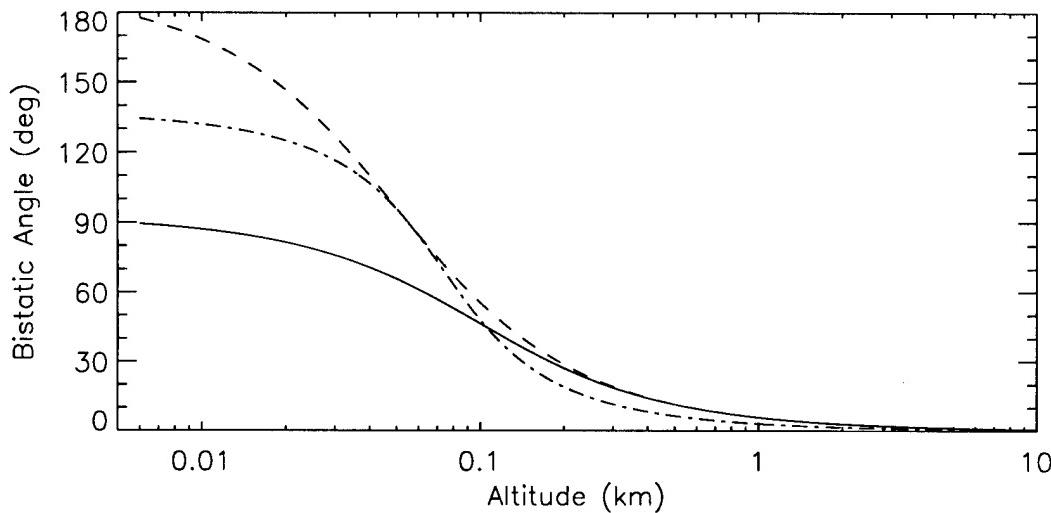
Figure 4-7: Bistatic angle as a function of altitude for the three cases outlined in text. Case 1 (solid); Case 2 (dashed); Case 3 (dash-dot).
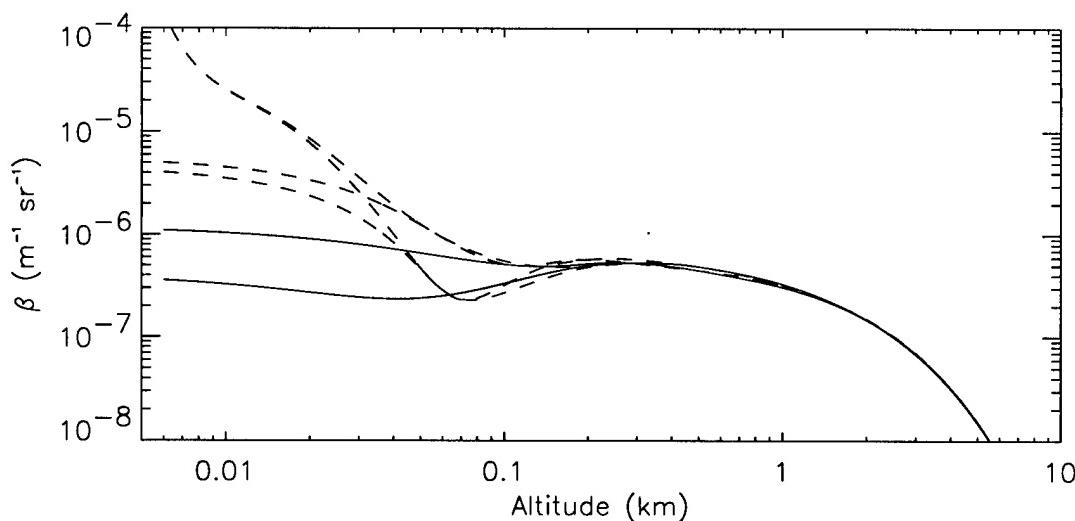
Figure 4-8: Volume scattering coefficient as a function of altitude for the three cases outlined in the text. The SF-1 aerosol distribution model is used to calculate β. Case 1 (solid); Case 2 (dashed); Case 3 (dash-dot). Both the s- and p-polarization are shown.

Table 4-3: System Parameters

Parameter	Symbol	Value
Baseline Separation	B	100 m
System Bandwidth	B_w	100 MHz
Wavelength	λ	1 μm
Quantum Efficiency	η_Q	0.5
CW Average Laser Power	P_L	5 W
1/e Pulse Width	σ_p	250 ns
Pulse Laser Energy	U_L	1 J
1/e Laser Intensity Radius	σ_L	$0.707\,\sigma_T$
1/e LO Intensity Radius	σ_{LO}	$0.707\,\sigma_R$
Aerosol Density @ Ground	N_o	5000 cm^{-3}
Index Structure Constant	$C_n{}^2(h{=}1\text{m})$	10^{-12} m$^{-2/3}$
Transmitter Focus	F_{TE}	∞
Receiver Focus	F_{RE}	∞

4.4.1 Case 1

The first case examined is for the transmit beam pointed directly vertical and the receiver optics scanned along the beam. This configuration, in conjunction with two other receivers, could be used to sense the 3-dimensional velocity vector along the transmit beam. An example of this multistatic system is shown in *Figure 4-9*. In this configuration, each receiver senses a Doppler shift that is proportional to the velocity along the bisector of the respective bistatic angle. If these Doppler sensitive directions have components in all three directions, the velocity vector can be determined.

View from above
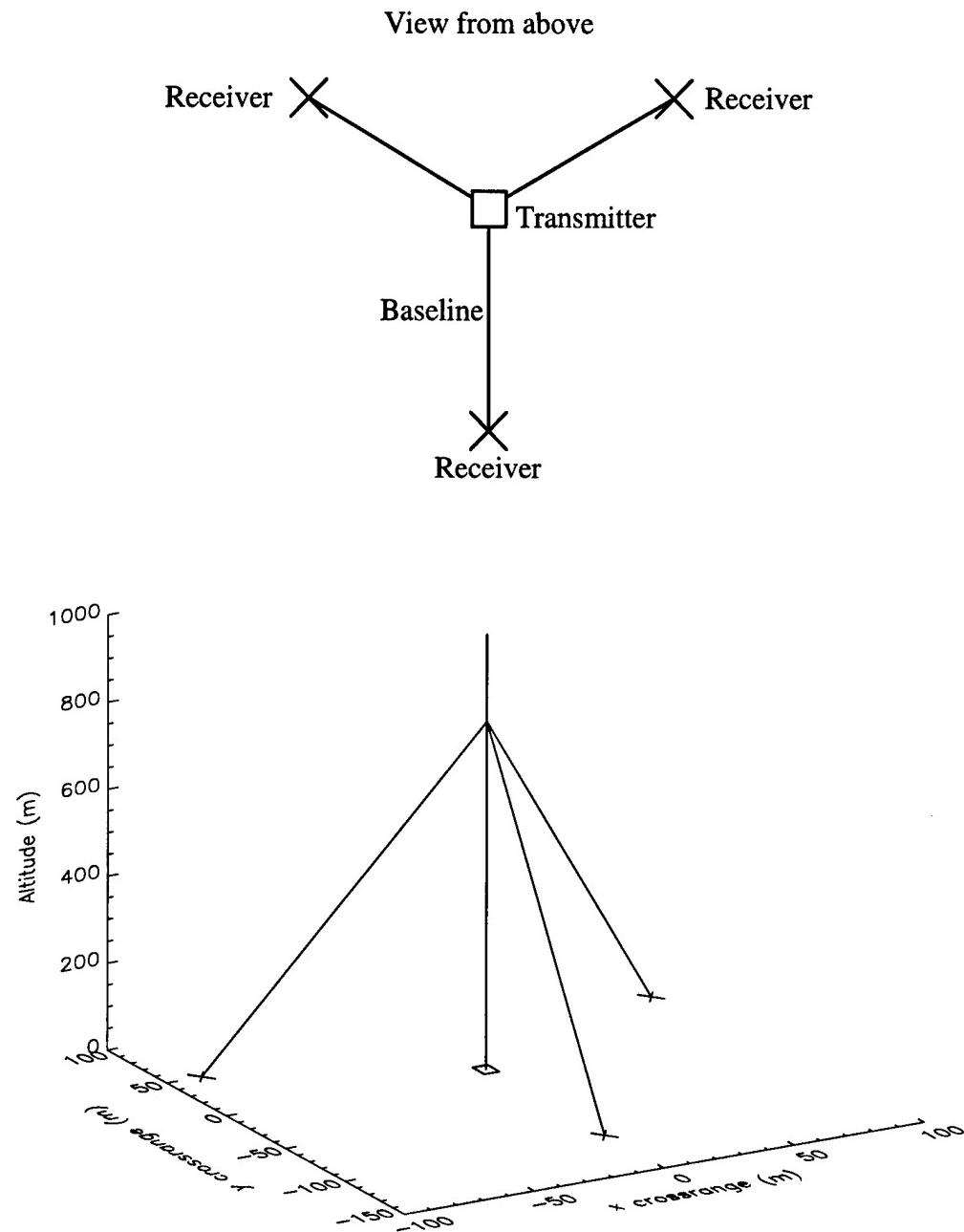
Figure 4-9: Case 1 multistatic geometry for sensing 3-dimensional vector winds along a vertical line from the transmitter. The box marks the location of the transmitter and the X's mark the locations of the receivers. The intersection of the lines is the center of the scattering volume. The baseline separation is 100 m.

Plots of the CW SNR for this geometry and a single transmitter/receiver pair are shown in *Figure 4-10* and *Figure 4-11*. Plots of the pulsed SNR case are shown in *Figure 4-12* and *Figure 4-13*. Note that the CW SNR is much lower than that of the pulsed SNR for typical CW average power. Also note that there is an optimum aperture size for each range.

The optimum aperture size can be determined by differentiating the expression for SNR with respect to $\sigma_R = \sigma_T$. Inserting the parameters given in *Table 4-3*, the SNR can be expressed as

$$\text{SNR} \propto \left(\frac{2\sigma_T^2}{3} + \frac{3B^2}{k^2\sigma_R^2} + \frac{6R_T^2}{k^2\sigma_R^2} \right)^{-1/2}, \tag{4.48}$$

and $R_R^2 = R_T^2 + B^2$ for Case 1 geometry. Minimizing this function with respect to σ_R yields

$$\sigma_R^{\text{opt}} = \left[\frac{9\left(2R_T^2 + B^2\right)}{2k^2} \right]^{1/4}$$

$$= 1.4565 \left[\frac{2R_T^2 + B^2}{k^2} \right]^{1/4}, \tag{4.49}$$

for the geometry of case 1. In the near field limit ($R_T \to 0$), the optimum aperture size approaches 5.8 mm for $B = 100$ m and $\lambda = 1$ μm. Optimizing the aperture size for the pulse case is accomplished by a closer examination of σ_{eff}^2. Rewrite Eq. (4.25) as

$$\sigma_{\text{eff}}^2 = \tau_p c \sin\theta_s \left[\left(\sigma_{BR}^2 + \sigma_{BT}^2 \right)(1 + \Delta) \right]^{1/2}, \tag{4.50}$$
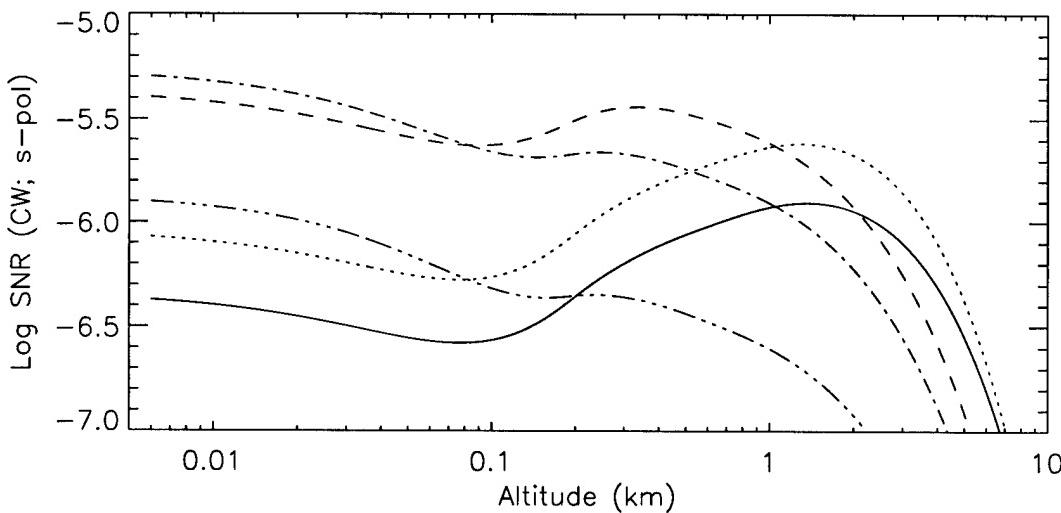
Figure 4-10: Case 1 CW SNR (p-polarization) plots for various aperture sizes. Refractive turbulence effects are not included. $\sigma_R = 100$ mm (solid); $\sigma_R = 50$ mm (dotted); $\sigma_R = 10$ mm (dashed); $\sigma_R = 5$ mm (dash-dot); $\sigma_R = 1$ mm (dash-triple dot).
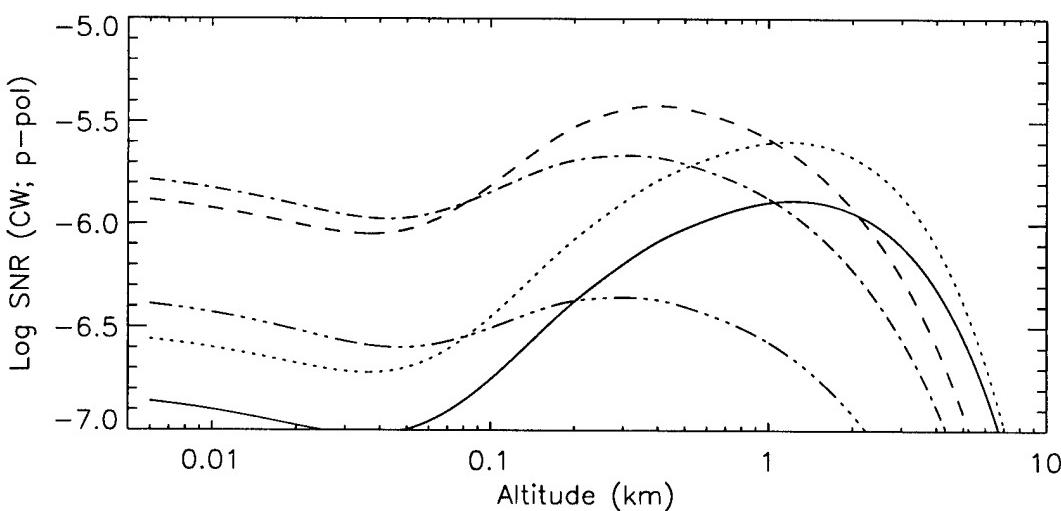
Figure 4-11: Case 1 CW SNR (s-polarization) plots for various aperture sizes. Refractive turbulence effects are not included. $\sigma_R = 100$ mm (solid); $\sigma_R = 50$ mm (dotted); $\sigma_R = 10$ mm (dashed); $\sigma_R = 5$ mm (dash-dot); $\sigma_R = 1$ mm (dash-triple dot).
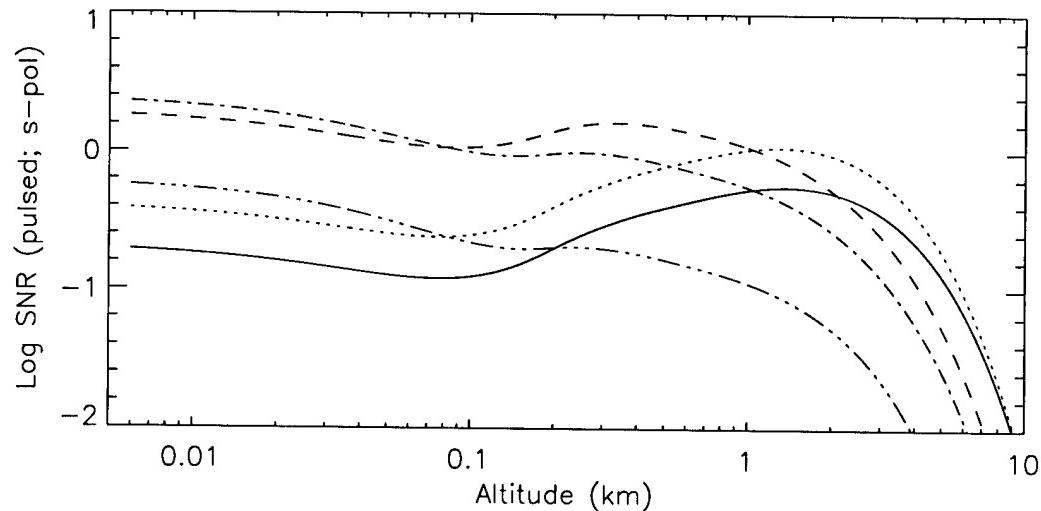
Figure 4-12: Case 1 pulsed SNR (p-polarization) plots for various aperture sizes. Refractive turbulence effects are not included. $\sigma_R = 100$ mm (solid); $\sigma_R = 50$ mm (dotted); $\sigma_R = 10$ mm (dashed); $\sigma_R = 5$ mm (dash-dot); $\sigma_R = 1$ mm (dash-triple dot).
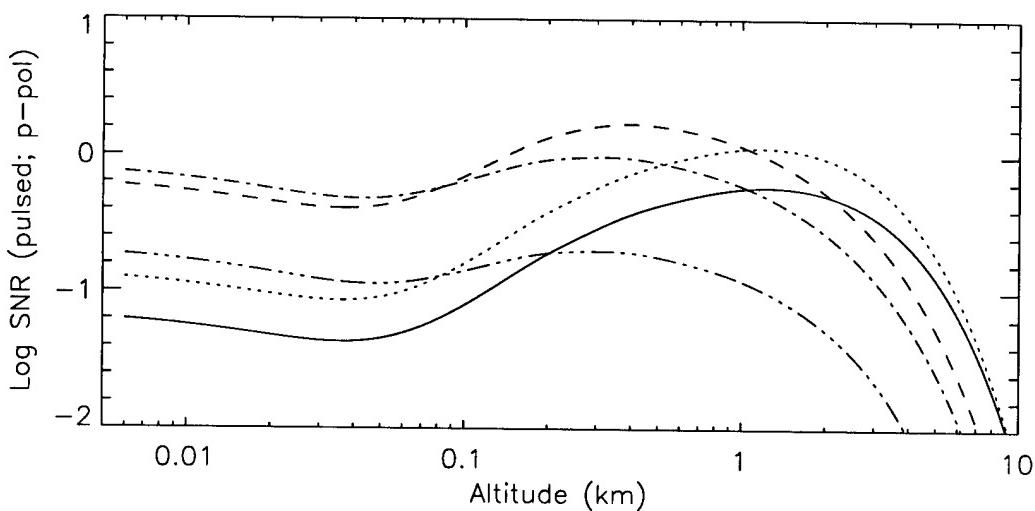
*Figure 4-13*: Case 1 pulsed SNR (s-polarization) for various aperture sizes. Refractive turbulence effects are not included. $\sigma_R = 100$ mm (solid); $\sigma_R = 50$ mm (dotted); $\sigma_R = 10$ mm (dashed); $\sigma_R = 5$ mm (dash-dot); $\sigma_R = 1$ mm (dash-triple dot).

where

$$\Delta = \frac{\sigma_{BR}^2(R_R) + \sigma_{BT}^2(R_T)\cos^2\theta_s}{\tau_p^2 c^2 \sin^2\theta_s}.$$ (4.51)

The parameter Δ is plotted in *Figure 4-14* for various apertures sizes. From this plot, it is evident that Δ is essentially zero, especially in the near field and

$$\sigma_{eff}^2 \approx \tau_p c \sin\theta_s \left(\sigma_{BR}^2 + \sigma_{BT}^2\right)^{1/2}.$$ (4.52)

Because $\Delta \approx 0$, the optimization of the pulsed SNR is identical to that of the CW SNR.

The coherent responsivity shows the same trend in terms of the effects of aperture size. A plot of the coherent responsivity for Case 1 is shown in *Figure 4-15*. As can be seen, the coherent responsivity is optimized in the near field for an aperture size of about 5 mm.

This optimization indicates that the transmit and LO beam sizes can also be small. Recall that $\sigma_{LO} = 0.707 \cdot \sigma_R$ and $\sigma_L = 0.707 \cdot \sigma_T$. Since small beam sizes can be used, the analysis can be simplified somewhat by assuming that the transmitter and receiver lenses are large compared to the beam sizes. At these beam sizes (~4 mm) the lenses only need to be about 25 mm before truncation effects can be ignored. In this case, the lens aperture sizes can be set to infinity and Eqs. (4.18) and (4.19) can be expressed as

$$\sigma_{BT}^2(z_p, R_T) = \sigma_L^2 + \frac{R_T^2}{k^2\sigma_L^2} + \frac{2R_T^2}{k^2\rho_o^2(R_T)},$$

$$\sigma_{BR}^2(x_p, z_p, R_R) = \sigma_{LO}^2 + \frac{R_R^2}{k^2\sigma_{LO}^2} + \frac{2R_R^2}{k^2\rho_o^2(R_R)}.$$ (4.53)
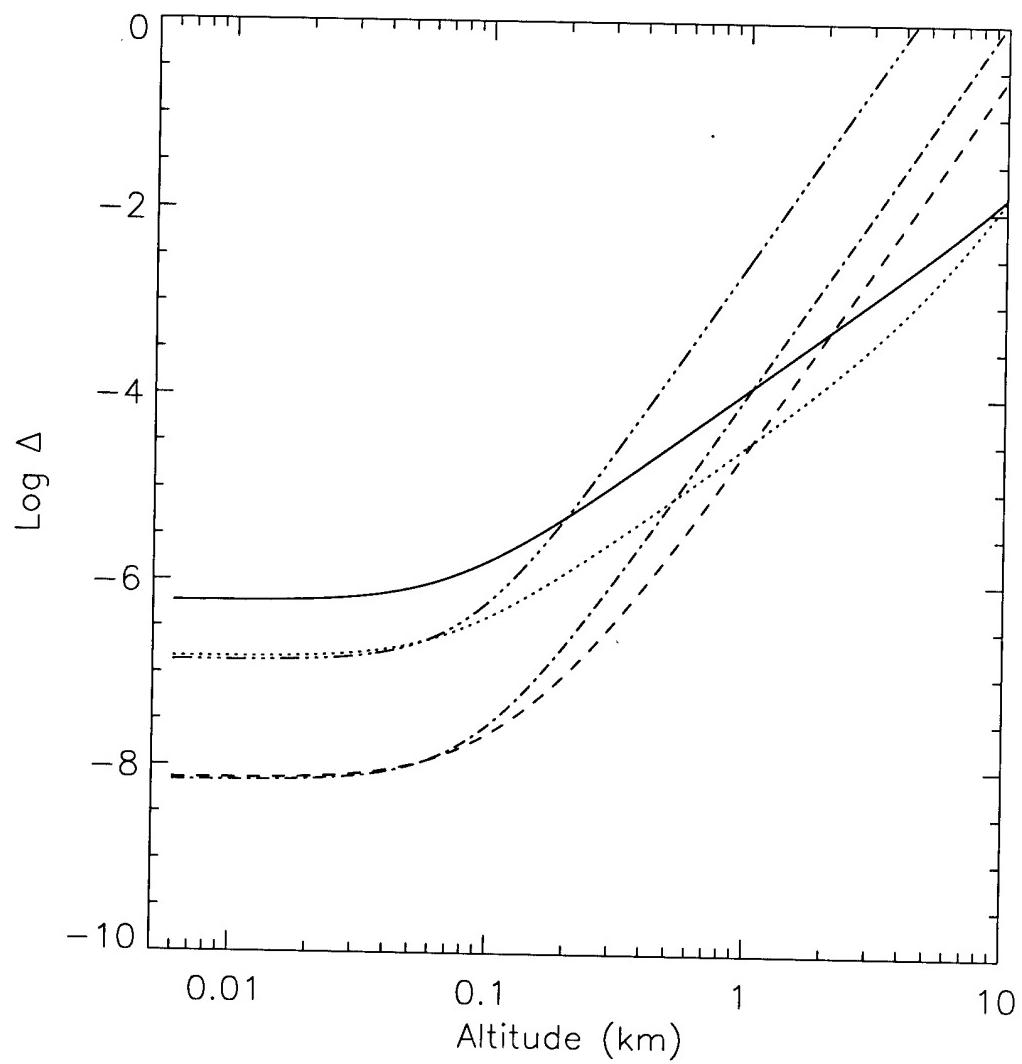
Figure 4-14: The parameter Δ from Eq. (4.51) for various apertures and Case 1 geometry. $\sigma_R = 100$ mm (solid); $\sigma_R = 50$ mm (dotted); $\sigma_R = 10$ mm (dashed); $\sigma_R = 5$ mm (dash-dot); $\sigma_R = 1$ mm (dash-triple dot).
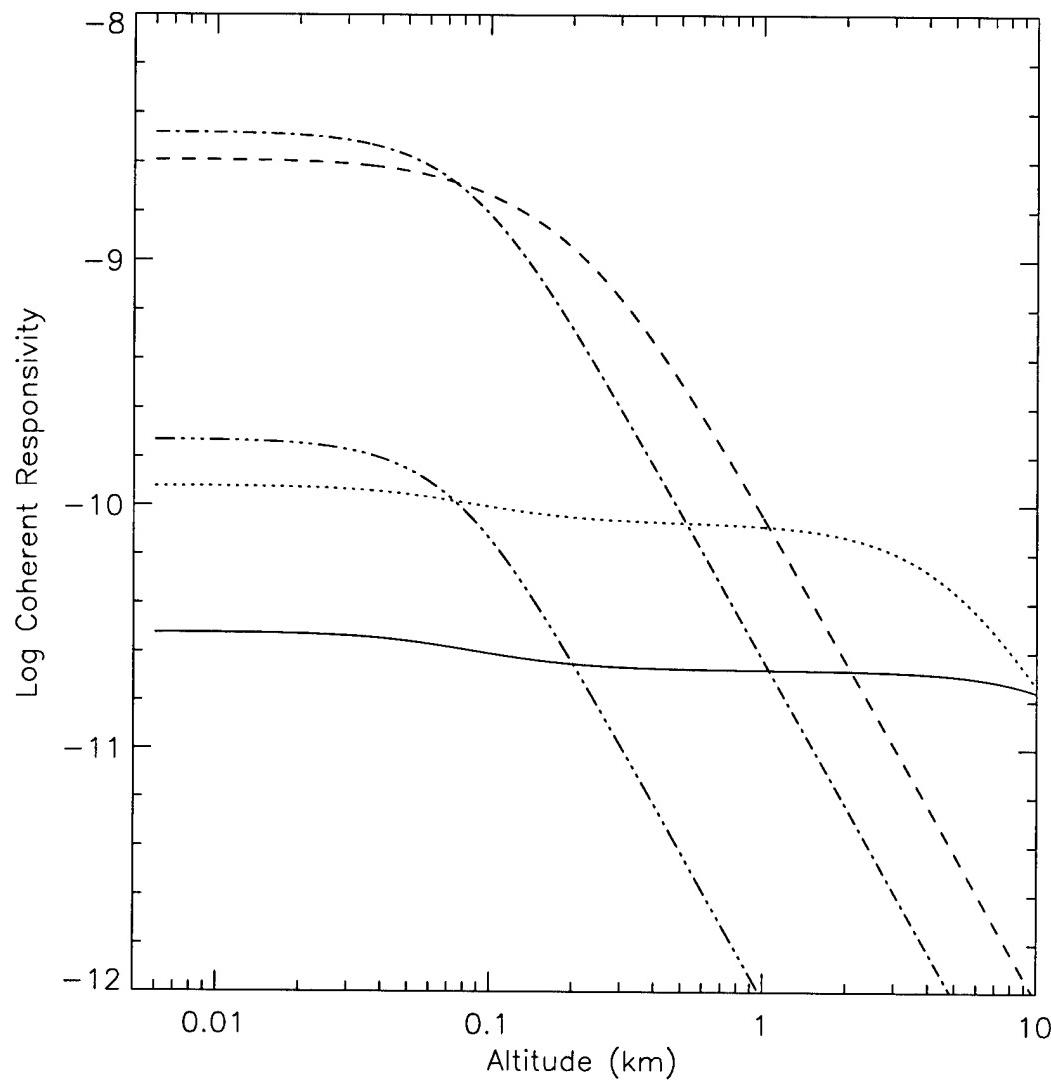
Figure 4-15: Case 1 coherent responsivity for various aperture sizes. $\sigma_R = 100$ mm (solid); $\sigma_R = 50$ mm (dotted); $\sigma_R = 10$ mm (dashed); $\sigma_R = 5$ mm (dash-dot); $\sigma_R = 1$ mm (dash-triple dot).

For infinite apertures, the transmitter and reciprocal receiver truncation ratios become unity. Assuming matched transmit and LO beams ($\sigma_L = \sigma_{LO}$), the SNR (assuming infinite apertures) can be maximized by noting that

$$\text{SNR} \propto \left(2\sigma_L^2 + \frac{B^2}{\sigma_L^2 k^2} + \frac{2R_T^2}{\sigma_L^2 k^2} \right)^{-1/2} . \tag{4.54}$$

Performing this optimization yields

$$\sigma_L^{\text{opt}} = \left[\frac{2R_T^2 + B^2}{2k^2} \right]$$

$$= 0.841 \left[\frac{2R_T^2 + B^2}{k^2} \right]. \tag{4.55}$$

In the near field limit ($R_T \to 0$), the optimum beam size approaches 3.3 mm for $B = 100$ m and $\lambda = 1$ μm, which in turn implies that the lens sizes need only be about 20 mm before the truncation effects can be neglected.

Plots of the CW SNR for this geometry and "infinite" aperture are shown in *Figure 4-16* and *Figure 4-17*. The pulsed case is shown in *Figure 4-18* and *Figure 4-19*. As can be seen in these plots, the SNR is improved. This is because there are no power truncation effects due to the lens apertures [see Eq. (4.15)]. The remainder of the calculations will be performed with the assumption that the aperture sizes are large compared to the transmit and LO beams.

From Eq. (4.55), it is evident that the optimum beam size increases with range, R_T. This trend can also be seen in the plots of SNR and especially coherent responsivity. Because the geometry in this type of system limits the accuracy of sensing horizontal winds at high altitudes, optimizing the "near field" SNR is desired.
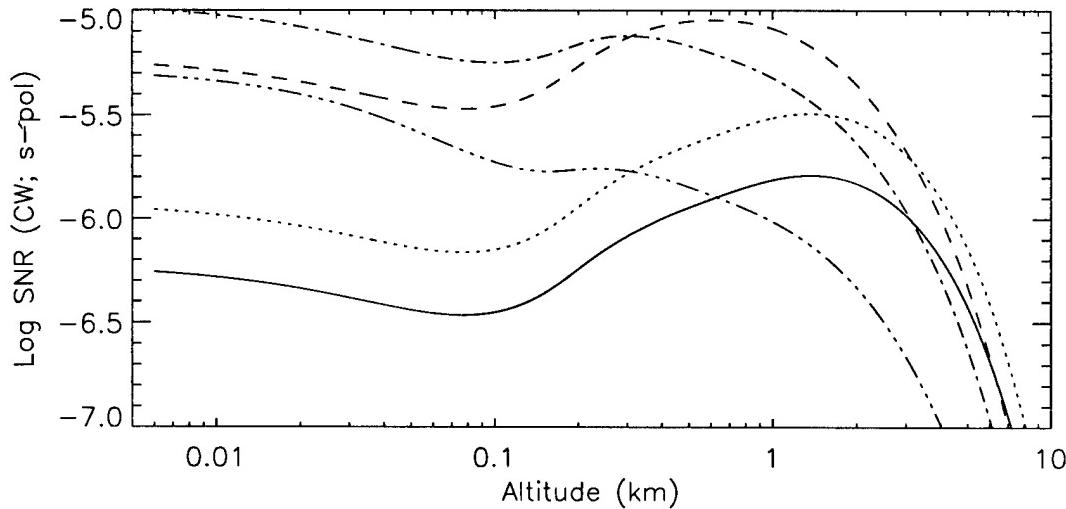
Figure 4-16: Case 1 CW SNR (p-polarization) plots for various beam sizes ("infinite" apertures). Refractive turbulence effects are not included. $\sigma_L = 100$ mm (solid); $\sigma_L = 50$ mm (dotted); $\sigma_L = 10$ mm (dashed); $\sigma_L = 5$ mm (dash-dot); $\sigma_L = 1$ mm (dash-triple dot).
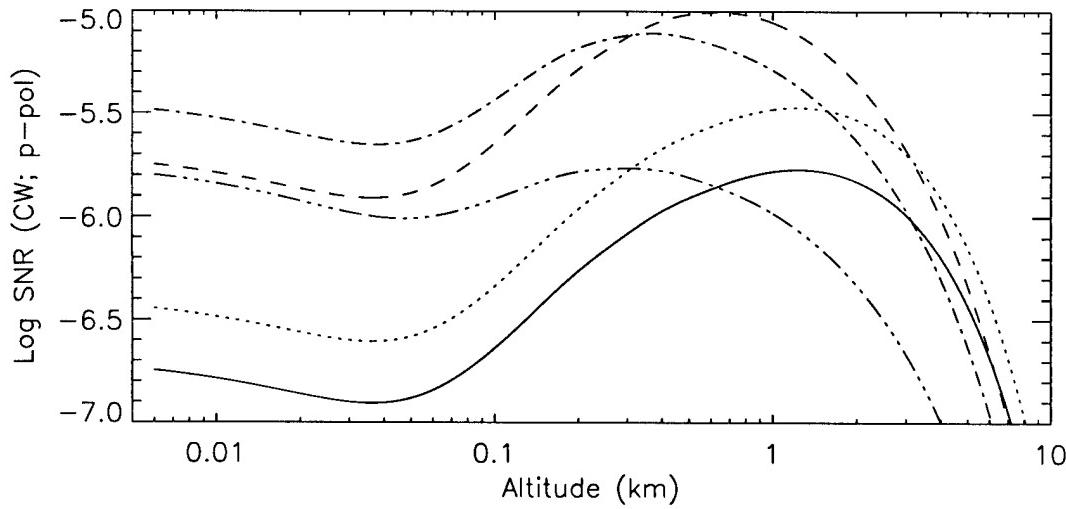
Figure 4-17: Case 1 CW SNR (s-polarization) plots for various beam sizes ("infinite" apertures). Refractive turbulence effects are not included. $\sigma_L = 100$ mm (solid); $\sigma_L = 50$ mm (dotted); $\sigma_L = 10$ mm (dashed); $\sigma_L = 5$ mm (dash-dot); $\sigma_L = 1$ mm (dash-triple dot).
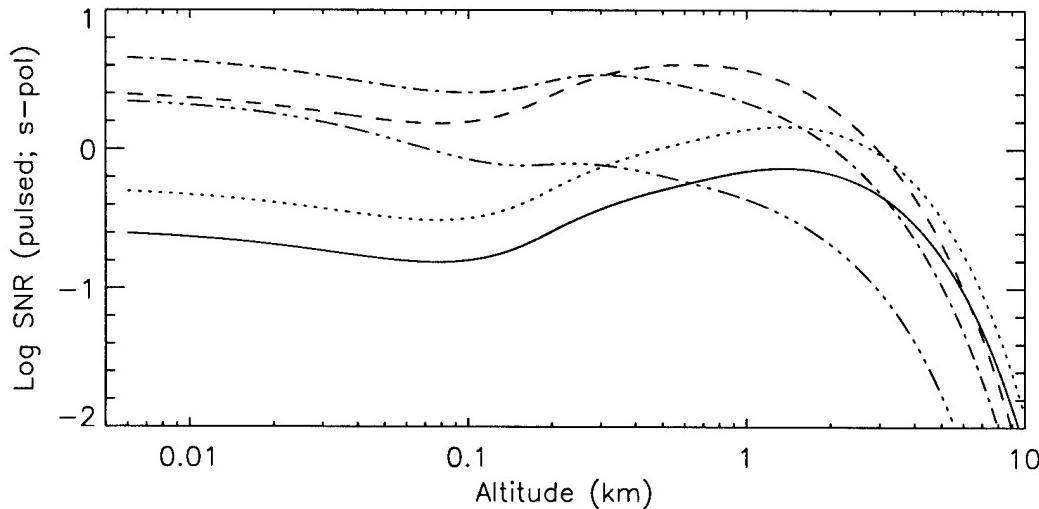
Figure 4-18: Case 1 pulsed SNR (p-polarization) plots for various beam sizes ("infinite" apertures). Refractive turbulence effects are not included. $\sigma_L = 100$ mm (solid); $\sigma_L = 50$ mm (dotted); $\sigma_L = 10$ mm (dashed); $\sigma_L = 5$ mm (dash-dot); $\sigma_L = 1$ mm (dash-triple dot).
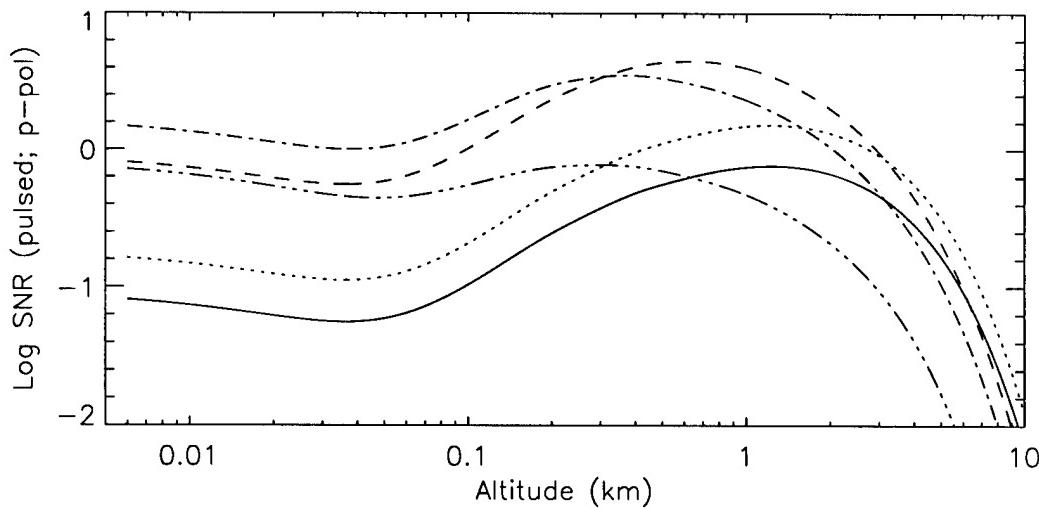
Figure 4-19: Case 1 pulsed SNR (s-polarization) plots for various beam sizes ("infinite" apertures). Refractive turbulence effects are not included. $\sigma_L = 100$ mm (solid); $\sigma_L = 50$ mm (dotted); $\sigma_L = 10$ mm (dashed); $\sigma_L = 5$ mm (dash-dot); $\sigma_L = 1$ mm (dash-triple dot).

An advantage of the small beam sizes, other than the obvious design advantages, is the spatial resolution achievable, at least in the near field. Recall that for this system, the spatial resolution, both in range and in the transverse direction, is determined by the overlap of the transmitted laser and the imagined BPLO. The approximate scattering volume is determined by finding the transverse scattering area (in the x_p-y_p plane) and multiplying by the extent in the z_p-direction. The transverse area is set by the transmit beam and the z_p extent is set by the BPLO beam at $x_p = y_p = 0$. The approximate volume is then given by

$$V \approx \int\limits_{-\infty}^{\infty}\int\limits_{-\infty}^{\infty}\int\limits_{-\infty}^{\infty} \exp\left[-\frac{x_p^2 + y_p^2}{\sigma_{BT}^2}\right]$$
$$\times \exp\left[-\frac{z_p^2 \sin^2\theta_S}{\sigma_{BR}^2}\right] dx_p dy_p dz_p$$
$$= \frac{\sqrt{\pi^3}\sigma_{BR}\sigma_{BT}^2}{\sin\theta_S}. \tag{4.56}$$

This integration is the same as the integration shown in Appendix A for the SNR. A plot of the scattering volume for various beam sizes is shown in *Figure 4-20*. From this plot it can be seen that for altitudes less than 1 km, the scattering volume is less than 100 cm^3 for the 5 mm beam.

Another advantage of the small beam sizes is the reduced effect of refractive turbulence. The reduction in SNR due to refractive turbulence is quantified with the SNR reduction factor, F [see Eqs. (4.45) and (4.46)]. By the same argument given for deriving Eq. (4.52), we can argue that, in the near field, the SNR reduction will be the same for the CW and pulsed systems. *Figure 4-21* and *Figure 4-22* show the SNR reduction factor for
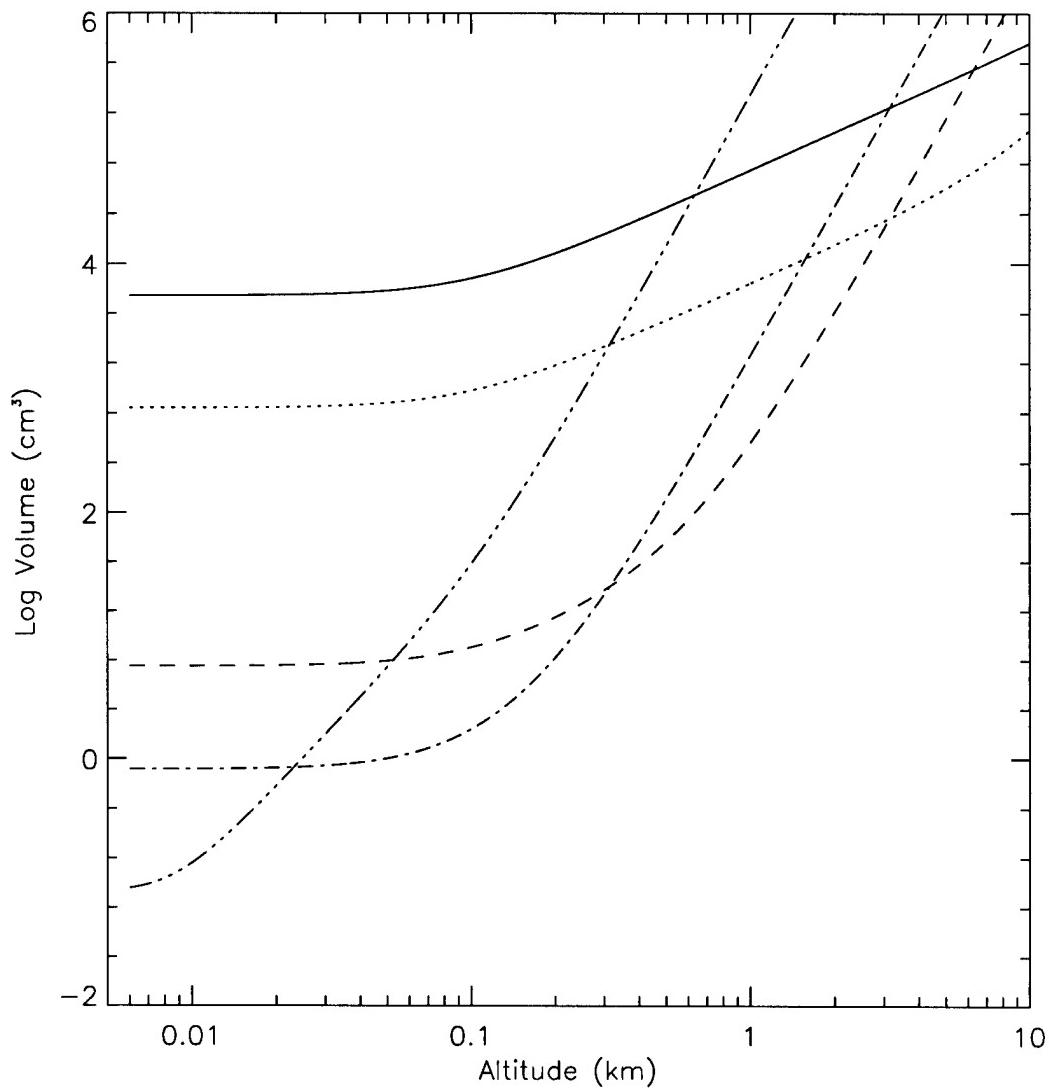
Figure 4-20: Case 1 scattering volume for various beam sizes. $\sigma_L = 100$ mm (solid); $\sigma_L = 50$ mm (dotted); $\sigma_L = 10$ mm (dashed); $\sigma_L = 5$ mm (dash-dot); $\sigma_L = 1$ mm (dash-triple dot).
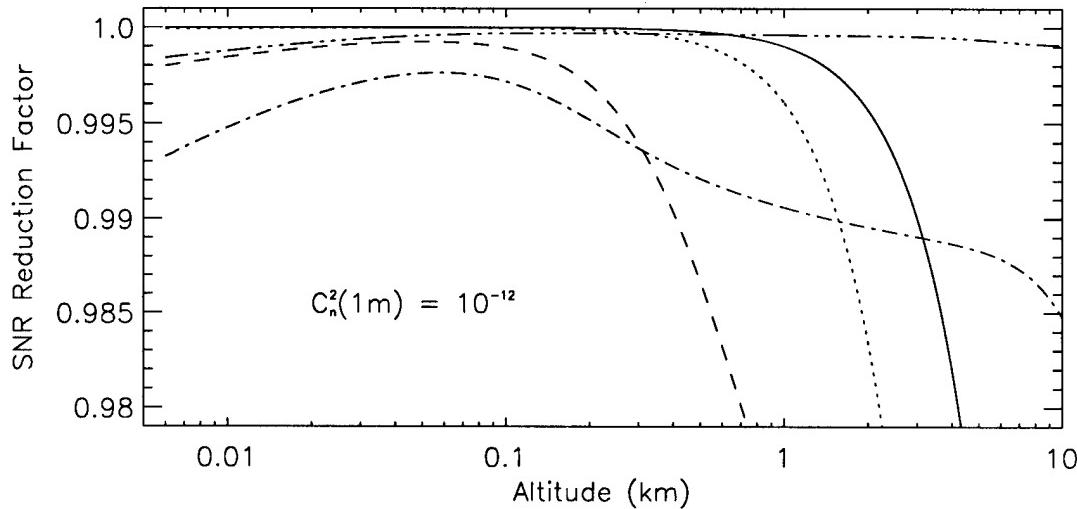
Figure 4-21: Case 1 SNR reduction for various beam sizes. $\sigma_L = 100$ mm (solid); $\sigma_L = 50$ mm (dotted); $\sigma_L = 10$ mm (dashed); $\sigma_L = 5$ mm (dash-dot); $\sigma_L = 1$ mm (dash-triple dot).
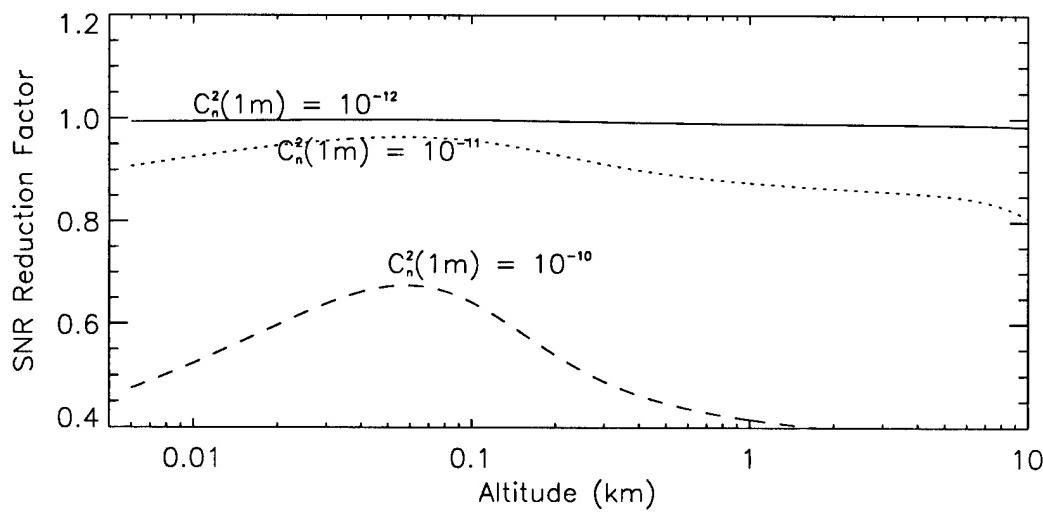

Figure 4-22: Case 1 SNR reduction for a fixed beam size ($\sigma_L = 5$ mm) and various turbulence strengths.

Case 1 geometry and various aperture sizes and for $\sigma_L = 5$ mm with various index structure constants at ground level. From the figure it is evident that the refractive turbulence has minimal effect on the SNR for typical turbulence strengths. Adverse effects are not present until the turbulence strength at the ground approaches 10^{-10} ($m^{2/3}$), which is considered to be very strong refractive turbulence.

4.4.2 Case 2

The second case examined is for a bistatic configuration with the transmitter and receiver scanned along a vertical line bisecting the baseline. *Figure 4-23* shows a diagram of this geometry. This configuration could be used to sense the vertical velocity vector along the bisector of the baseline separation.
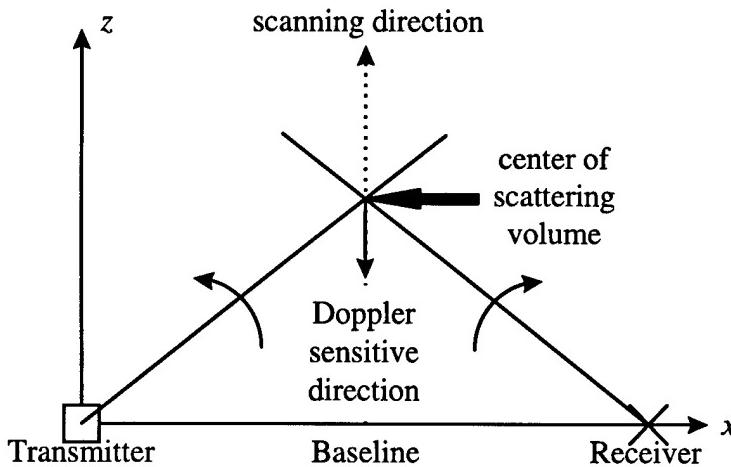
Figure 4-23: Case 2 geometry for sensing vertical velocity.

For this geometry, the optimum beam size is expressed as

$$\sigma_L^{opt} = \left[\frac{\left(B^2 + 4R^2\right)}{4k^2} \right]^{1/4}$$

$$= 0.707 \left[\frac{B^2 + 4R^2}{k^2} \right]^{1/4}, \tag{4.57}$$

where R is the altitude. In the near field limit ($R \to 0$), the optimum beam size

approaches 2.82 mm for $B = 100$ m and $\lambda = 1$ μm. Plots of the SNR for this case and a

beam size of 3.0 mm are shown in *Figure 4-24*. Also evident in SNR plots for Case 2 is

the strong forward scattering at low altitudes, as expected. The enhancement in β for

near-forward scatter is also shown in *Figure 4-7*.

The coherent responsivity for this geometry and a beam size of 3.0 mm is shown

in *Figure 4-25*, and the scattering volume is shown in *Figure 4-26*. The coherent

responsivity shows a slight increase at approximately 50 m. Looking at Eq. (4.20) we see

that since all of the terms in the denominator are positive, the coherent responsivity peaks

when $\theta_S = 90°$. For Case 2 geometry, when the center of the sensing volume is at an

altitude of 50 m, $\theta_S = 90°$.

The scattering volume for the 3 mm beam is less than 100 cm^3 out to about 1 km

and the minimum volume is at 50 m where $\theta_S = 90°$. The refractive turbulence effects are

shown in *Figure 4-27*. Again, the effects are minimal for all regions of interest.
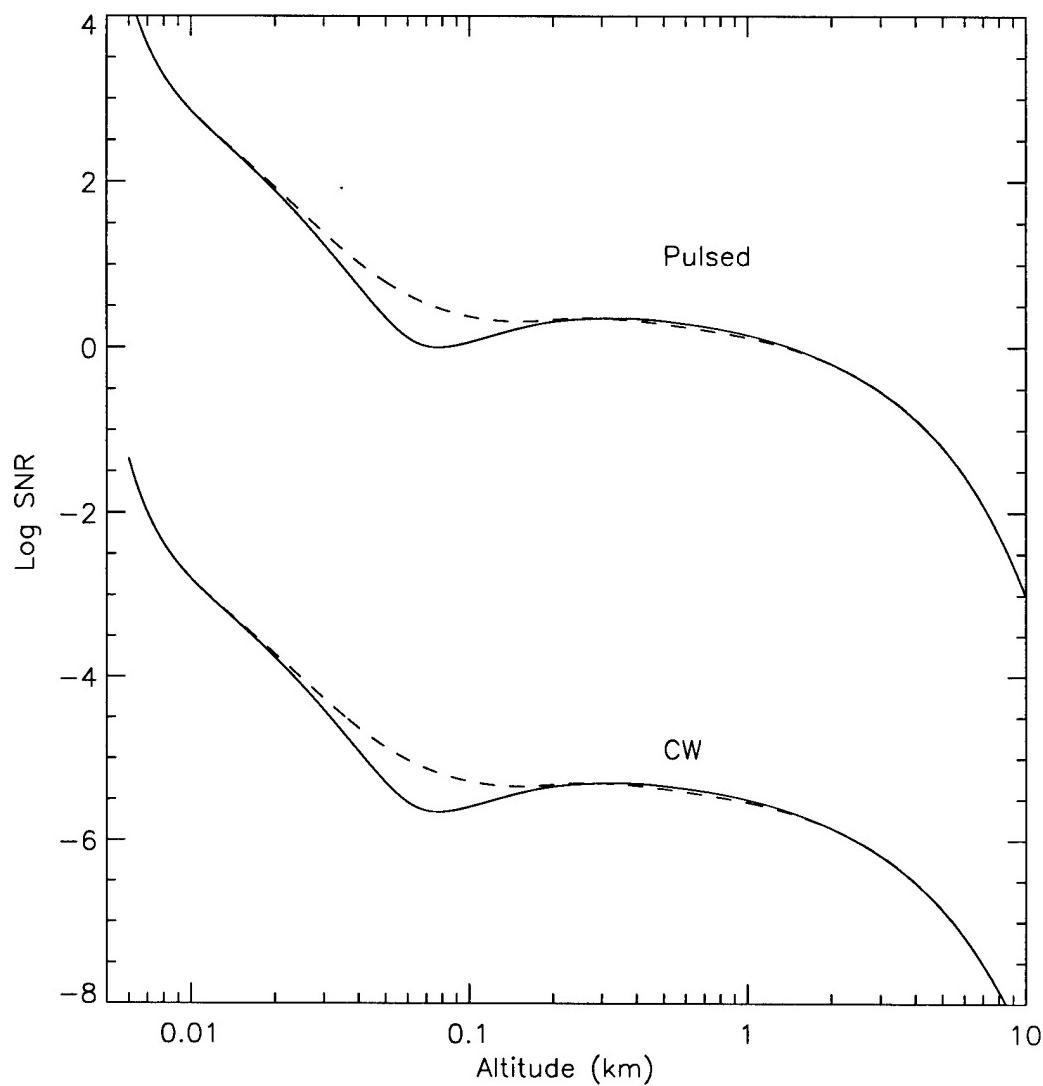
Figure 4-24: Case 2 SNR plots for $\sigma_L = 3$ mm. Refractive turbulence effects are not included. Both CW and pulsed cases are shown. Solid line is p-polarization and dashed line is s-polarization.
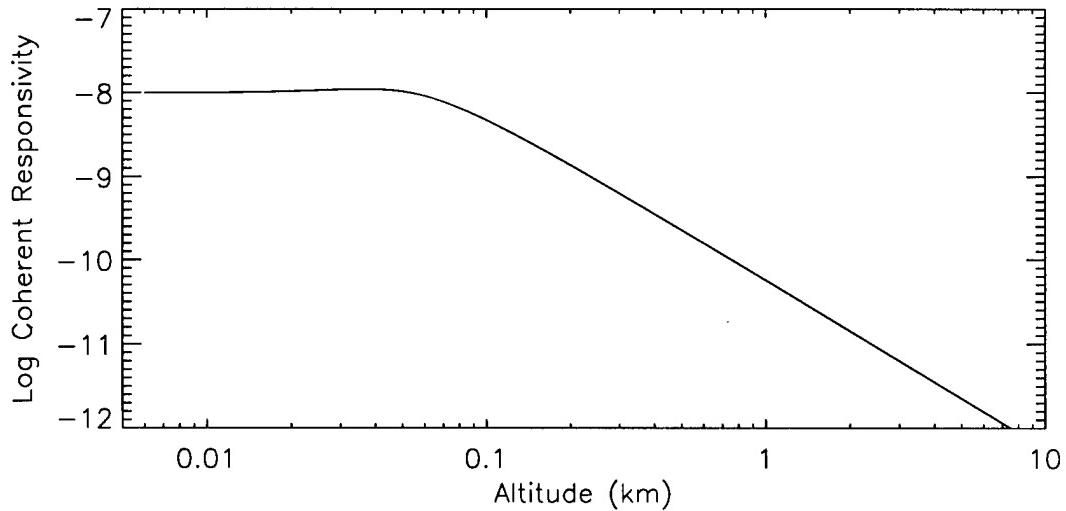
Figure 4-25: Case 2 coherent responsivity for $\sigma_L = 3$ mm.
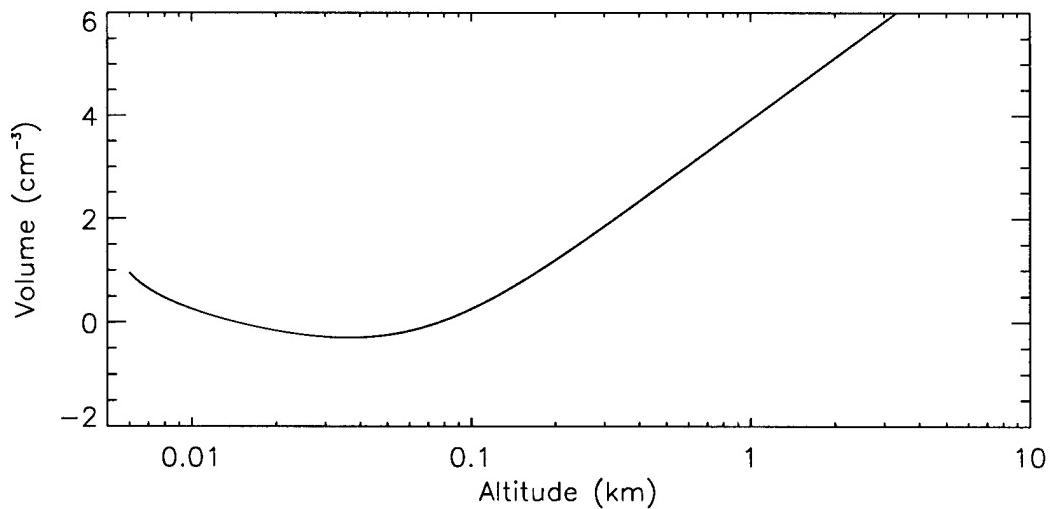
Figure 4-26: Case 2 scattering volume $\sigma_L = 3$ mm.
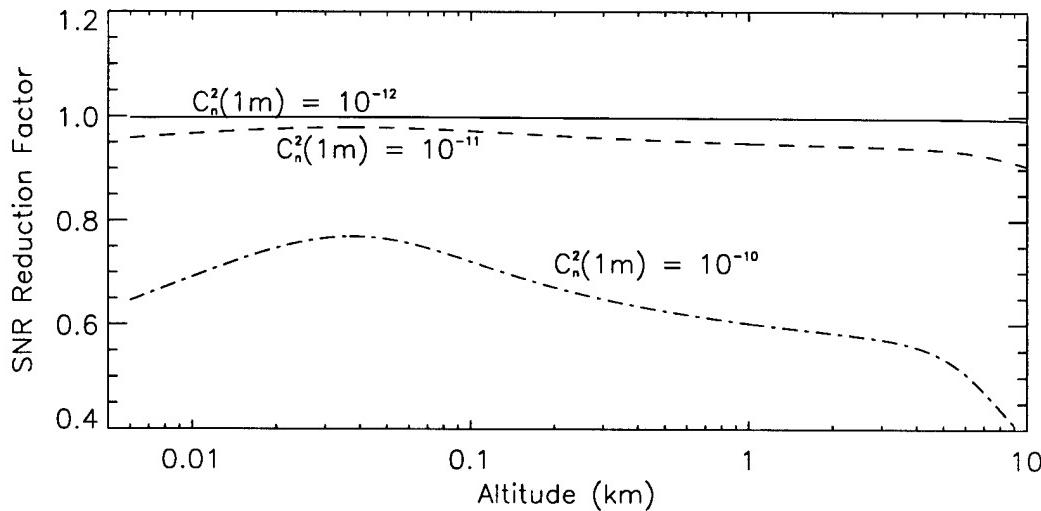
Figure 4-27: Case 2 SNR reduction for $\sigma_L = 3$ mm and various turbulence strengths.

4.4.3 Case 3

The third case examined is for the transmit beam pointed at 45° and the receiver optics scanned along the beam. A diagram of the geometry is shown in *Figure 4-28*. This configuration is included to show the effects of increased horizontal propagation on performance.

For this geometry, the optimum beam size is given by

$$\sigma_L^{opt} = \left[\frac{\left(B^2 - 2BR + 4R^2\right)}{2k^2} \right]^{1/4}$$

$$= 0.841 \left[\frac{(B-R)^2 + 3R^2}{k^2} \right]^{1/4}, \tag{4.58}$$
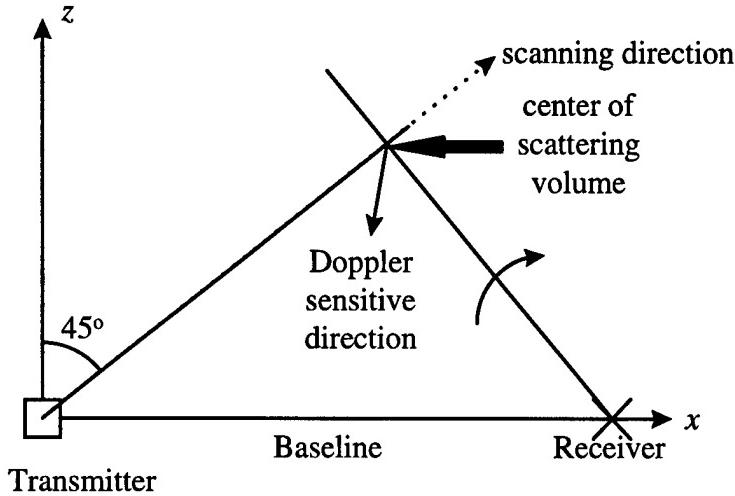
Figure 4-28: Diagram of Case 3 geometry.

where R is the altitude. In the near field limit ($R_T \rightarrow 0$), the optimum beam size

approaches 3.35 mm for B = 100 m and λ = 1 µm. The plots of SNR, coherent

responsivity, volume, and refractive turbulence effects for this geometry and σ_L = 3 mm

are shown in *Figure 4-29* through *Figure 4-32* respectively. Evident in *Figure 4-30* is the

enhancement in coherent responsivity at an altitude of about 50 km, where the bistatic

angle, θ_S = 90°. The refractive turbulence effects are more detrimental in this case, as

shown in *Figure 4-32*, due to the increased horizontal propagation. However, the effects

are still small for the problem space of interest—low altitudes and small apertures.
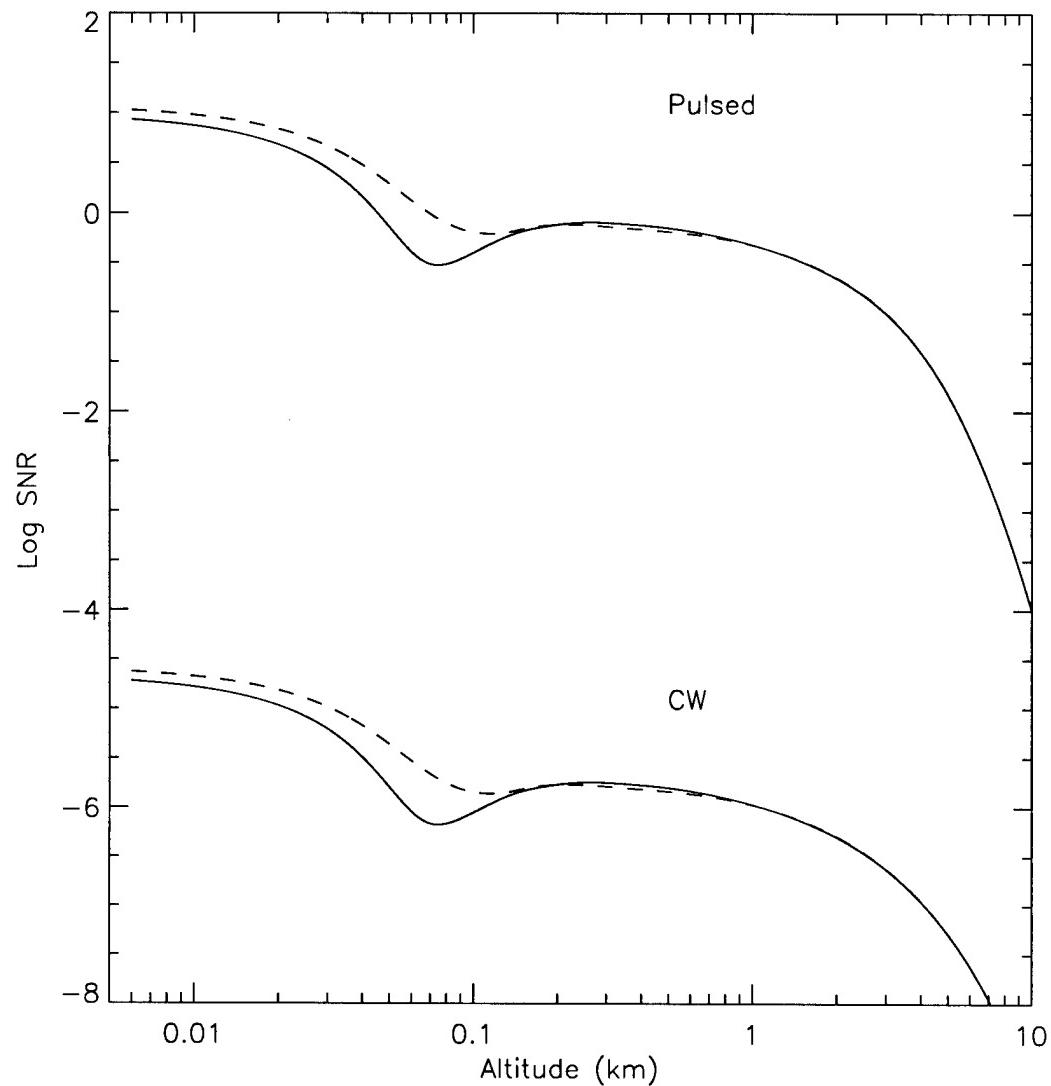
Figure 4-29: Case 3 SNR plots for $\sigma_L = 3$ mm. Refractive turbulence effects are not included. Both CW and pulsed cases are shown. Solid line is p-polarization and dashed line is s-polarization.
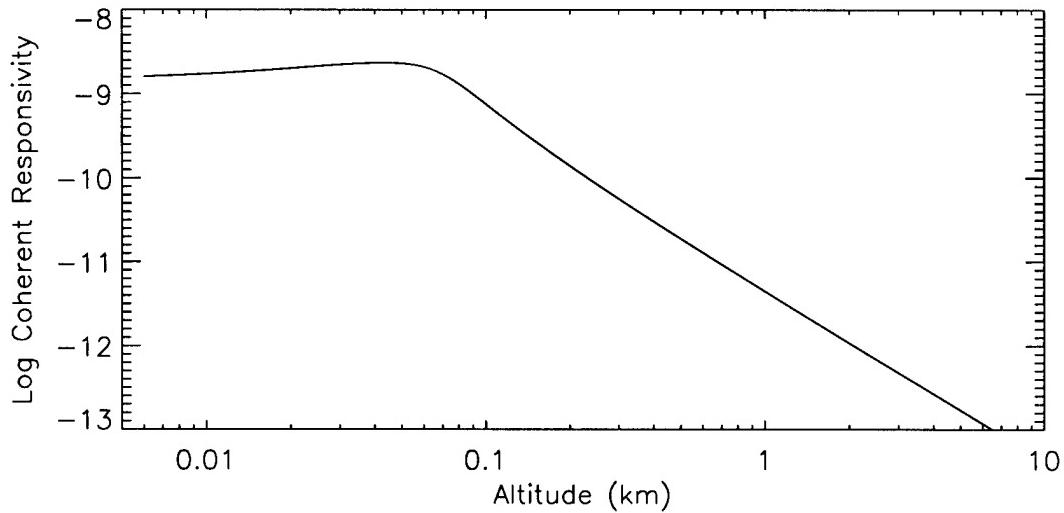
Figure 4-30: Case 3 coherent responsivity for $\sigma_L = 3$ mm.
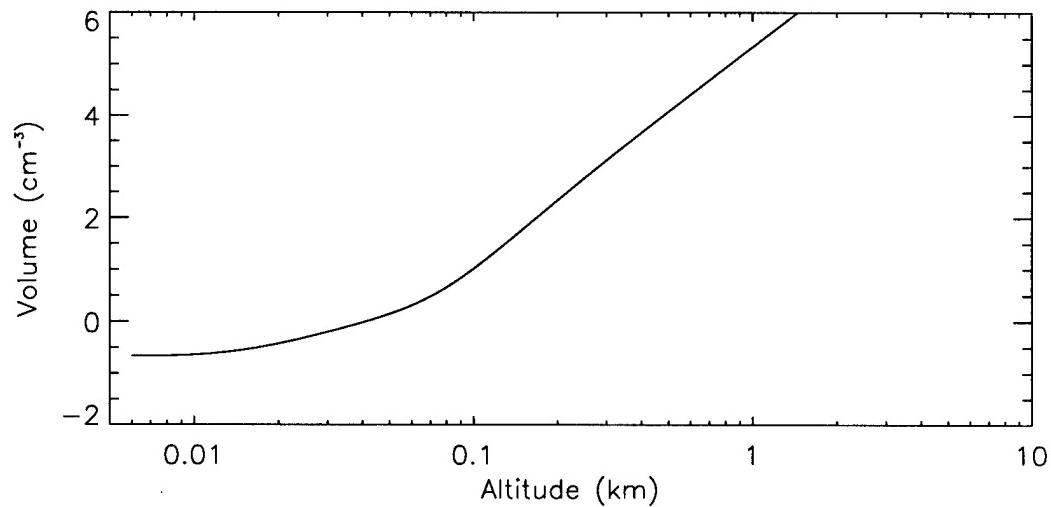
Figure 4-31: Case 3 scattering volume for $\sigma_L = 3$ mm.
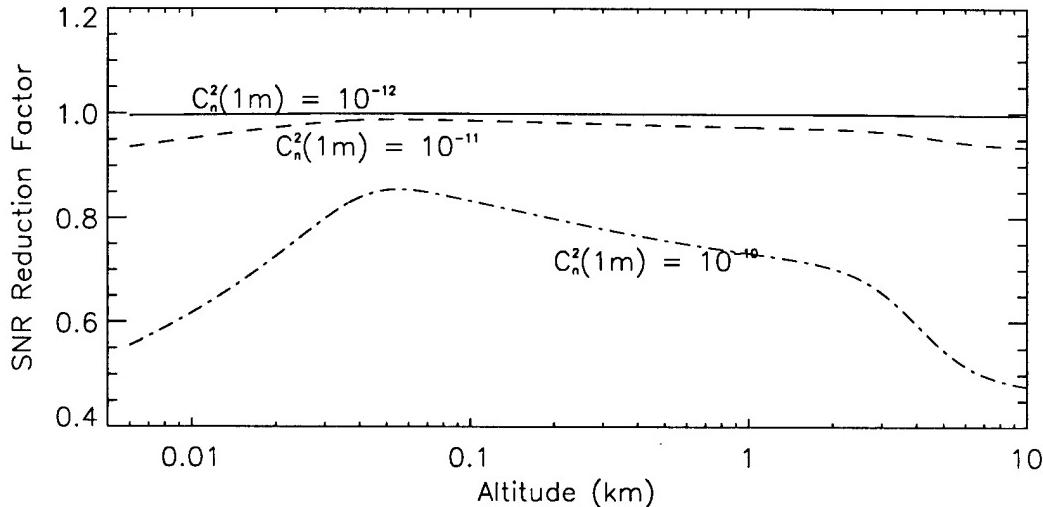
Figure 4-32: Case 3 SNR reduction for $\sigma_L = 3$ mm and various turbulence strengths.

4.4.4 Monostatic Configuration

This configuration is added as a test case to verify the accuracy of the equations derived above. The SNR for this case is shown in *Figure 4-33*. Because the volume backscatter coefficient, β, is different for our application, (Frehlich assumes a constant β as a function of altitude [32]), the SNR does not compare directly. However, since the coherent responsivity does not depend on such system parameters, a direct comparison can be made. The coherent responsivity and the heterodyne efficiency for the monostatic case are shown in *Figure 4-34* and *Figure 4-35*. These plots agree with the results of Frehlich for the 10 cm aperture, collimated case [32].
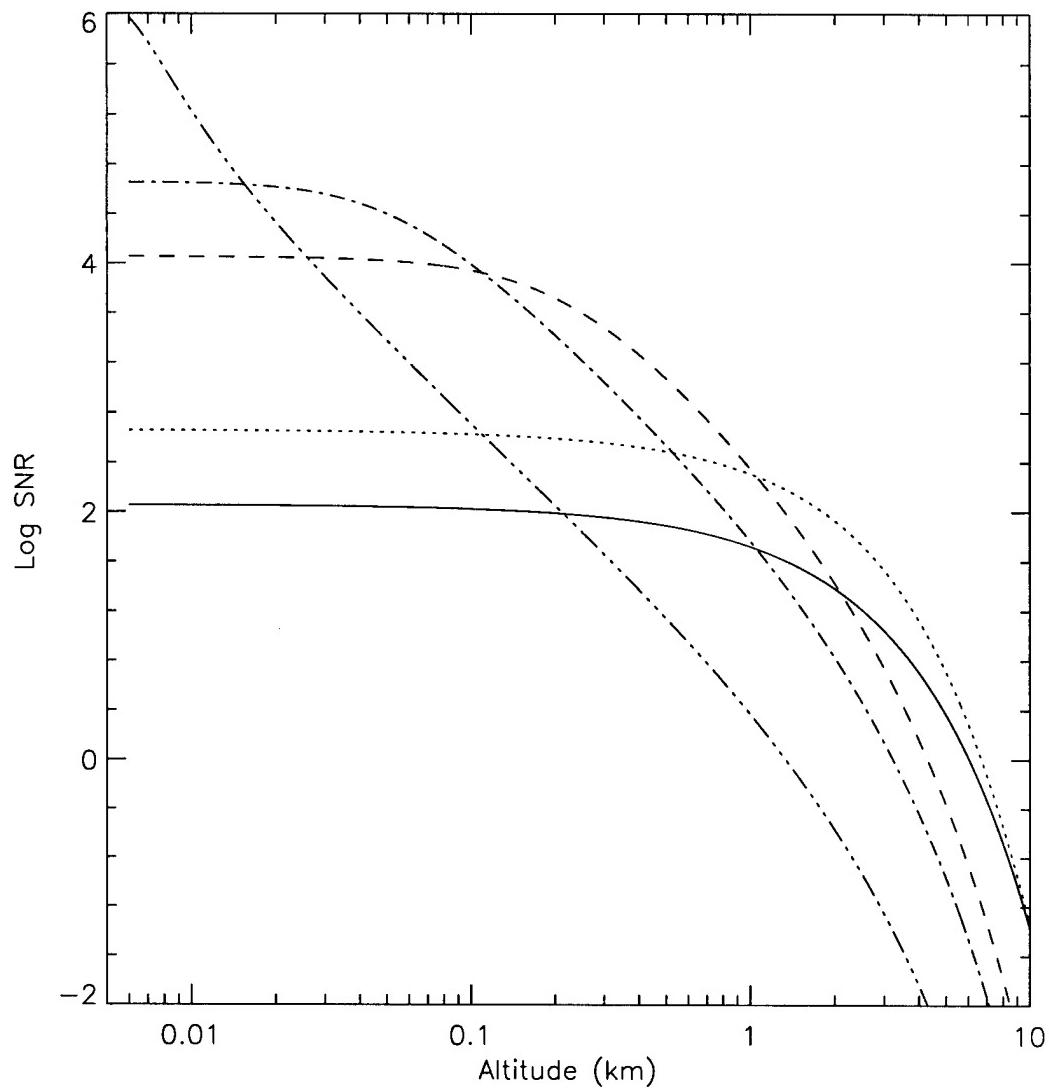
Figure 4-33: Monostatic SNR for a pulsed coherent lidar system for various apertures. $\sigma_R = 100$ mm (solid); $\sigma_R = 50$ mm (dotted); $\sigma_R = 10$ mm (dashed); $\sigma_R = 5$ mm (dash-dot); $\sigma_R = 1$ mm (dash-triple dot).
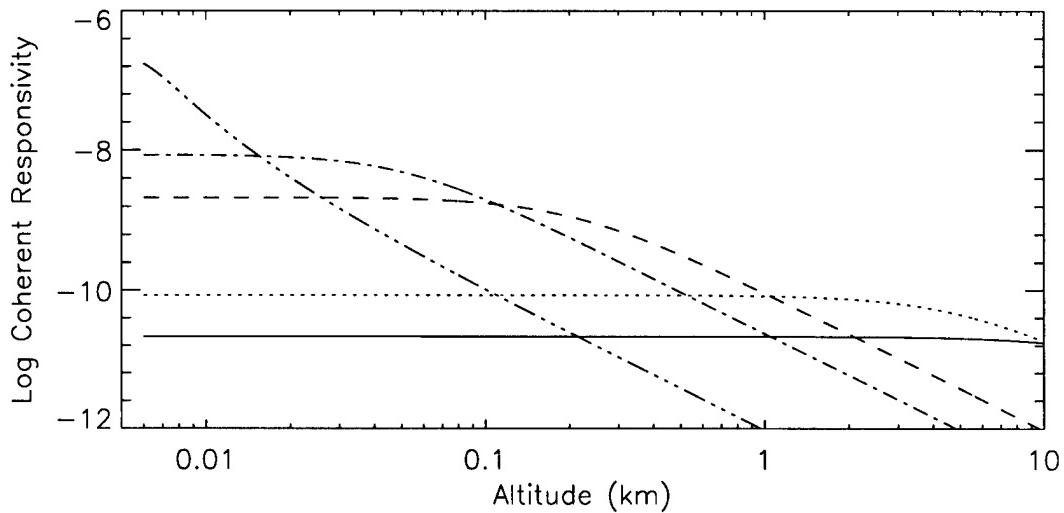
Figure 4-34: Coherent responsivity for the monostatic case and various apertures.
$\sigma_R = 100$ mm (solid); $\sigma_R = 50$ mm (dotted); $\sigma_R = 10$ mm (dashed); $\sigma_R = 5$ mm (dash-dot);
$\sigma_R = 1$ mm (dash-triple dot).
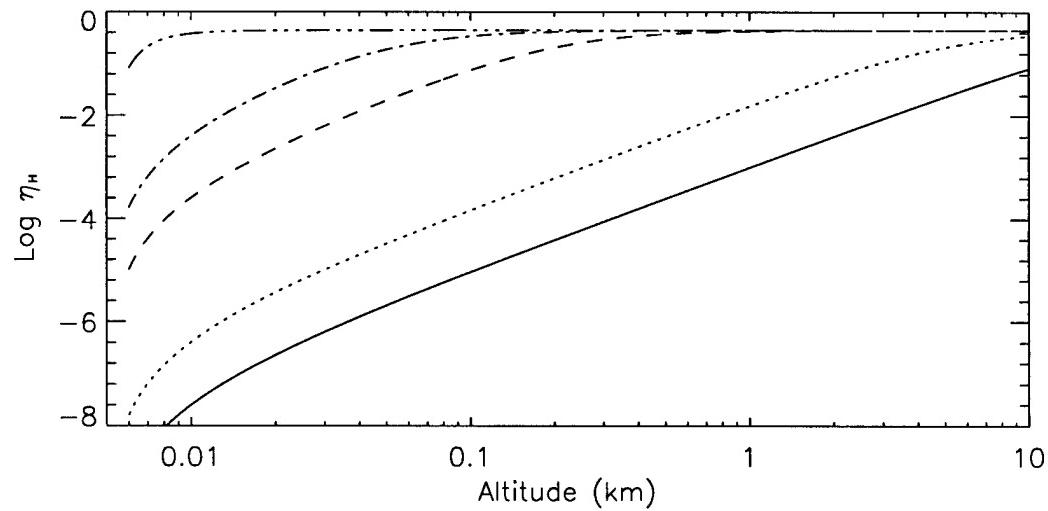
Figure 4-35: Heterodyne efficiency for the monostatic case and various apertures.
$\sigma_R = 100$ mm (solid); $\sigma_R = 50$ mm (dotted); $\sigma_R = 10$ mm (dashed); $\sigma_R = 5$ mm (dash-dot);
$\sigma_R = 1$ mm (dash-triple dot).

It is interesting to compare the scattering volume for the monostatic configuration

to that of the bistatic configuration. In the monostatic case, the z_p extent is determined by

the pulse length. In this case, the scattering volume is given as

$$V = \frac{\pi \sigma_{BT}^2 c \, \Delta t}{2}$$
$$= \pi \sigma_{BT}^2 c \tau_p \sqrt{\ln 2}, \tag{4.59}$$

where $\Delta t = 2(\ln 2)^{\frac{1}{2}} \cdot \tau_p$ is the effective pulse length for the pulse profile given in Eq.

(4.22). A plot of the scattering volume is shown in *Figure 4-36*. As can be seen, the

monostatic scattering volumes for this pulse length are much larger than the scattering

volumes in the multistatic case.

As evident in all of the plots presented in this section, there is not a great deal of

difference in performance between the three cases. All three cases exhibit the same

characteristics in terms of an optimum aperture size and minimal effects of refractive

turbulence. Aside from the strong forward scattering evident in Case 2, the only

difference between the SNR of the three cases is (approximately) a scale factor. Also

evident in these plots is the poor CW SNR performance (as compared to the pulsed SNR)

for the system parameters used in this analysis.

4.5 Detection and Estimation

Now that the SNR has been determined, the CRLB for the estimation of the mean

frequency can be addressed. Only the pulsed case is considered in this analysis because,

as can be seen from the SNR plots, the pulsed case has much higher SNR. First, the
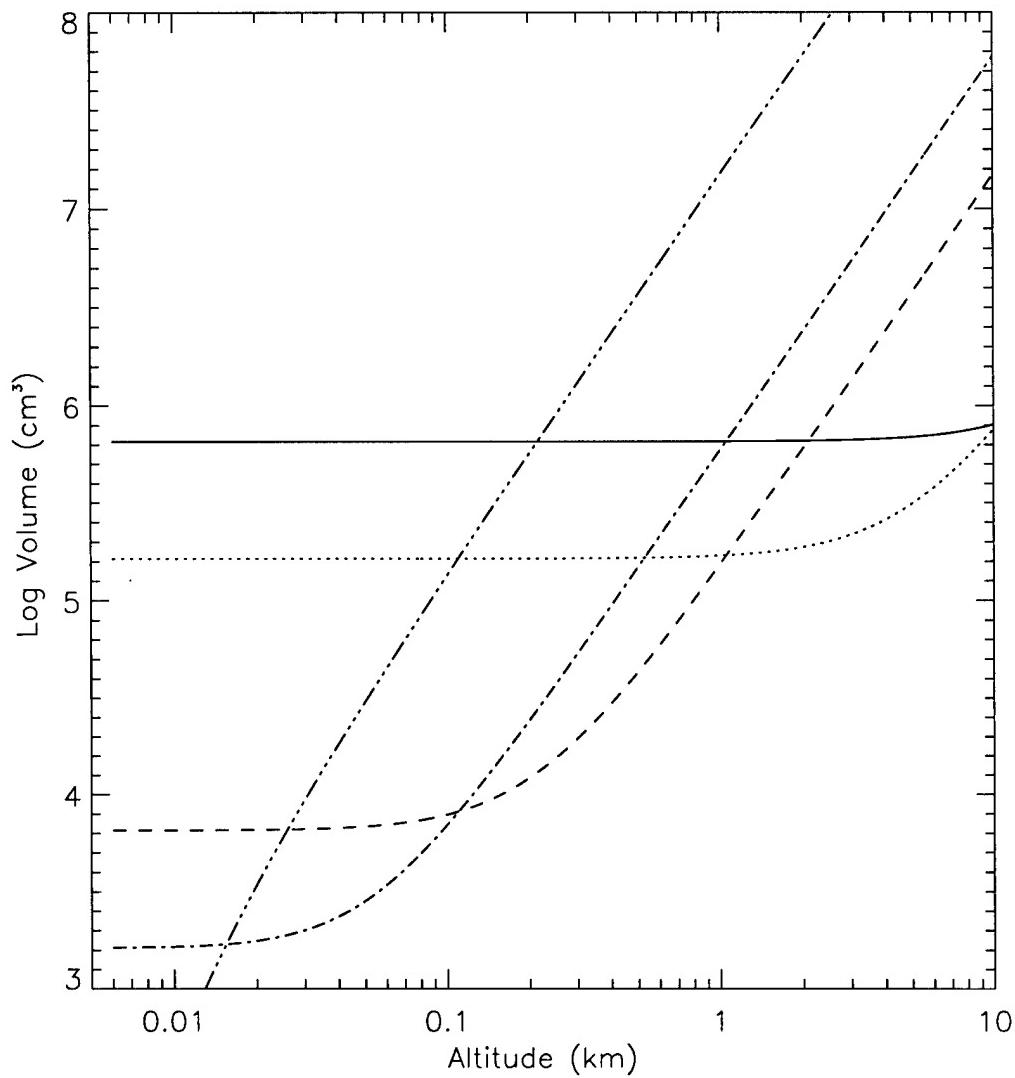
Figure 4-36: Effective scattering volume for the monostatic configuration and various apertures. The 1/*e* pulse width is 250 ns. σ_R = 100 mm (solid); σ_R = 50 mm (dotted); σ_R = 10 mm (dashed); σ_R = 5 mm (dash-dot); σ_R = 1 mm (dash-triple dot).

number of coherent photoelectrons must be determined. From Eqs. (3.57) and (4.24), for

a pulsed system we see that

$$g(t) = \exp\left[-\frac{(t-\tau)^2}{\tau_p}(1-\varepsilon)\right],$$ (4.60)

and

$$\mathrm{SNR}_{max} = \frac{U_L \eta_Q K^2(R_T, R_R)\beta(R_T, \theta_s)\lambda^3 T_T T_R}{\pi h B_w \sigma_{eff}^2(R_T, R_R)},$$ (4.61)

where the functional dependence of ε on R_T and R_R has been omitted for brevity.

Inserting Eq. (4.60) into (3.58) the effective observation interval becomes

$$T_g = \int_{-\infty}^{\infty} \exp\left[-\frac{(t-\tau)^2}{\tau_p}(1-\varepsilon)\right] dt$$

$$= \tau_p \sqrt{\frac{\pi}{1-\varepsilon}}.$$ (4.62)

Then the average number of coherent photoelectrons is given by

$$\Phi = \frac{U_L \eta_Q K^2(R_T, R_R)\beta(R_T, \theta_s)\lambda^3 T_T T_R \tau_p}{\sqrt{\pi(1-\varepsilon)} h \sigma_{eff}^2(R_T, R_R)}.$$ (4.63)

Note that Φ is simply a scaled version of the maximum SNR,

$$\Phi = \mathrm{SNR}_{max} B_w \tau_p \sqrt{\frac{\pi}{1-\varepsilon}} \approx 44.3 \times \mathrm{SNR}_{max},$$ (4.64)

where the systems parameters from *Table 4-3* have been inserted and ε is assumed to be

zero, which will be shown to be a valid assumption. The number of coherent

photoelectrons for the pulsed system and all three geometries (s-polarization only) are

shown in *Figure 4-37*. From this plot it can be seen that for Cases 2 and 3 the number of
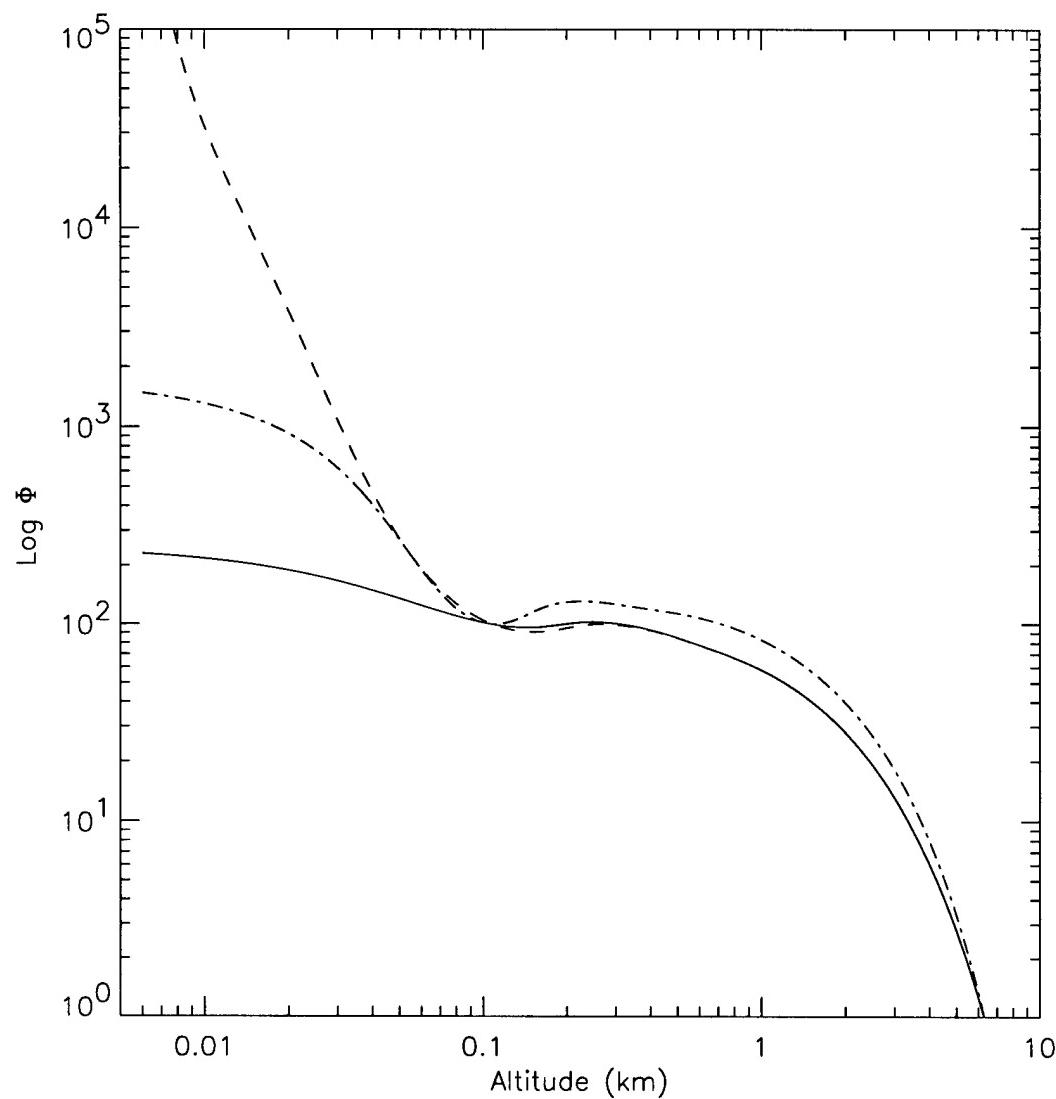
Figure 4-37: Case 1 (solid), Case 2 (dashed), and Case 3 (dash-dot) coherent photoelectrons (s-pol only) for pulsed system and $\sigma_L = 3$ mm (solid).

coherent photoelectrons is very high in the near field. This is due to the forward

scattering in these geometries.

The next step in the determination of the CRLB is to calculate $\tilde{f}(t)$ from the

signal model of Eqs. (3.24) and (3.25) and the pulse profile of Eq. (4.22). From the

expression for the SNR, we see that the effective pulse profile is given by $g(t)$ which is

proportional to $\left|\tilde{f}(t)\right|^2$. Therefore, finding the complex envelope is accomplished by

normalizing the function $g(t)$, or

$$\left|\tilde{f}(t)\right|^2 = \frac{g(t)}{T_g} = \left(\frac{1-\varepsilon}{\pi\tau_p^2}\right)^{1/2} \exp\left[-\frac{(t-\tau)^2}{\tau_p}(1-\varepsilon)\right],$$

and

$$\tilde{f}(t) = \left(\frac{1-\varepsilon}{\pi\tau_p^2}\right)^{1/2} \exp\left[-\frac{(t-\tau)^2}{2\tau_p}(1-\varepsilon)\right], \tag{4.65}$$

which, as expected, is entirely real. Then from Eq. (3.45), the mean-square duration of

the complex envelope is

$$\overline{t^2} = \left(\frac{1-\varepsilon}{\pi\tau_p^2}\right)^{1/2} \int_{-\infty}^{\infty} u^2 \exp\left[-\frac{u^2}{\tau_p^2}(1-\varepsilon)\right] dt$$

$$= \frac{\tau_p^2}{2(1-\varepsilon)}. \tag{4.66}$$

Inserting Eq. (4.66) into Eq.(3.62), the CRLB for estimating ω is

$$\sigma_\omega^2 \geq \left(\frac{\Phi+1}{\Phi^2}\right)\left(\frac{1-\varepsilon}{\tau_p^2}\right). \tag{4.67}$$

From this equation, it can be seen that the longer the pulse width, the lower the CRLB.

This makes sense, since lengthening the pulse is equivalent to narrowing the transmitted

spectrum. This will be true to the extent that the effective observation interval T_g does not get longer than the correlation time due to the rearrangement of aerosol particles within the scattering volume. When this occurs, the Rayleigh target model of Eq. (3.24) is no longer valid because of the temporal speckle caused by the random motion of the aerosols [see *Figure 2-2*].

In Section 4.4.1 it was shown that the term Δ could be ignored because it was much less than 1 for the lower altitudes. The equation for ε [Eq. (4.26)] can be written in terms of Δ as

$$\varepsilon = \frac{\Delta}{1+\Delta}, \tag{4.68}$$

and since Δ is always greater than 1, ε will always be less than Δ and it too can be ignored. A plot of ε is shown in *Figure 4-38*. As can be seen in this plot and from Eqs. (4.26) and (4.68), ε has a peak value of 1 for large ranges. The parameters ε and Δ will be assumed zero for the remaining analysis. Under this assumption, the CRLB becomes

$$\sigma_\omega^2 \geq \left(\frac{\Phi+1}{\Phi^2}\right)\left(\frac{1}{\tau_p^2}\right). \tag{4.69}$$

Each receiver transmitter pair will detect a Doppler shift that is proportional to the component of velocity in the direction of the bisector of the bistatic angle. Designate this velocity as v_p^b, where the b designates velocity along the bisector. Then the Doppler shift at a single detector can be written as

$$\omega = k\, v_p^b, \tag{4.70}$$
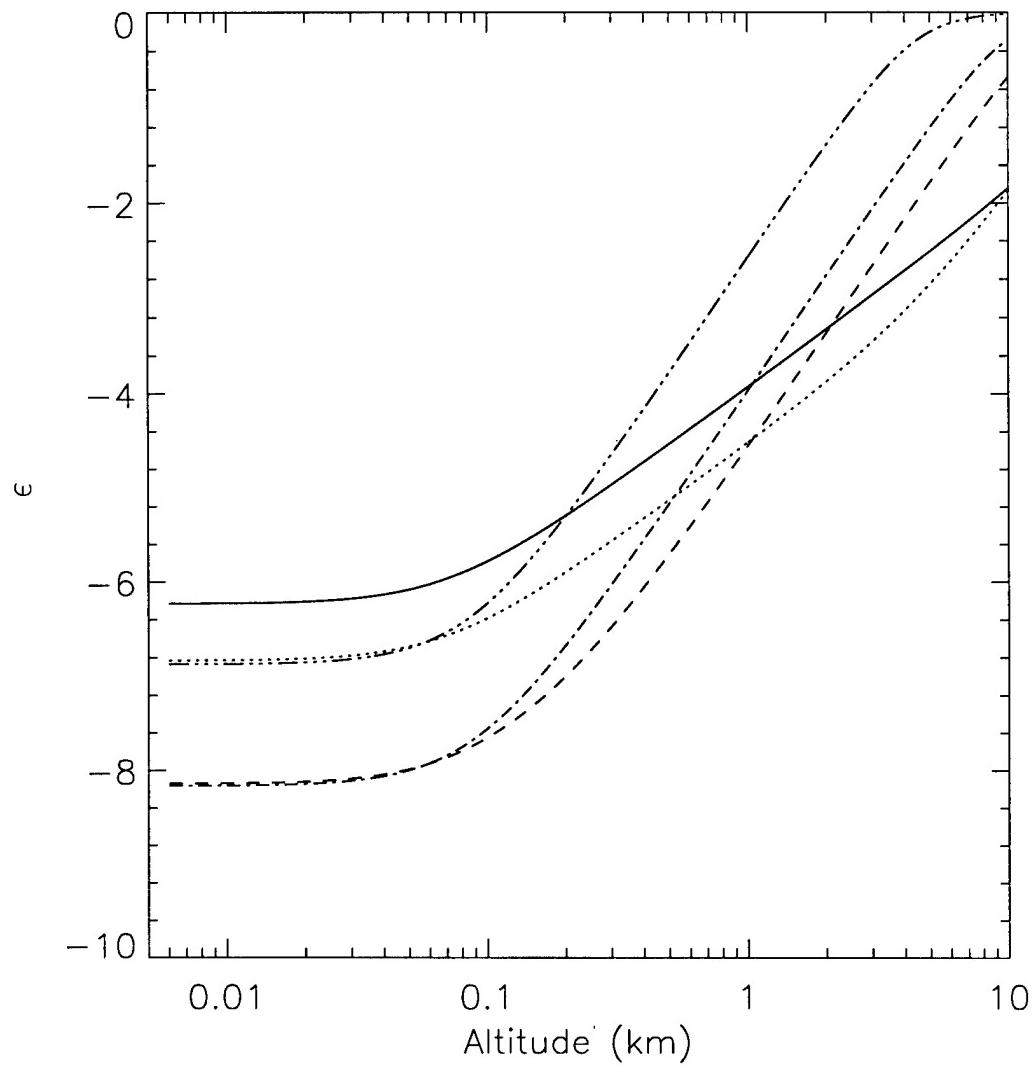
Figure 4-38: The parameter ε from Eq. (4.26) for various apertures and Case 1 geometry. $\sigma_R = 100$ mm (solid); $\sigma_R = 50$ mm (dotted); $\sigma_R = 10$ mm (dashed); $\sigma_R = 5$ mm (dash-dot); $\sigma_R = 1$ mm (dash-triple dot).

and the lower bound on the estimation error variance of the velocity estimate is

$$
\sigma_{v_p^b}^2 \geq \frac{1}{k^2} \sigma_\omega^2
$$
$$
= \left(\frac{\Phi + 1}{\Phi^2} \right) \left(\frac{1}{k^2 \tau_p^2} \right), \tag{4.71}
$$

where k is the wavenumber. This bound on the velocity estimation error is plotted in *Figure 4-39*. This plot indicates the CRLB on the standard deviation of the velocity estimate is less than 1 m/sec for a single shot at altitudes less than 1 km. For the optimum beam size, the CRLB is less than 10 cm/sec for altitudes less than 1 km. It should be noted that this is a lower bound on performance and is not necessarily the actual performance. It has, however, been shown that for this signal model, if Φ is greater than 10, the CRLB can be reached using ML estimation in as few as 10 shots [73, Chap. 10].

To include the effects of the inversion error on estimation [Eqs. (3.18)], a specific geometry must be assumed. Looking at the Case 1 geometry with three detectors, as illustrated in *Figure 4-9*, the SNR will be identical in all three detectors if the transmit beam is circularly polarized. This polarization state insures that there will always be energy in both the p- and s-polarization states. In this case the error in each measurement is independent and identically distributed (i.i.d.) and the estimation error covariance matrix can be written as

$$
\underline{\Lambda}_\varepsilon = \sigma_\omega^2 \underline{I} \tag{4.72}
$$

where $\underline{I}$ is the identity matrix. Inserting Eq. (4.72) in to Eq. (3.18), the velocity error covariance matrix can be expressed as
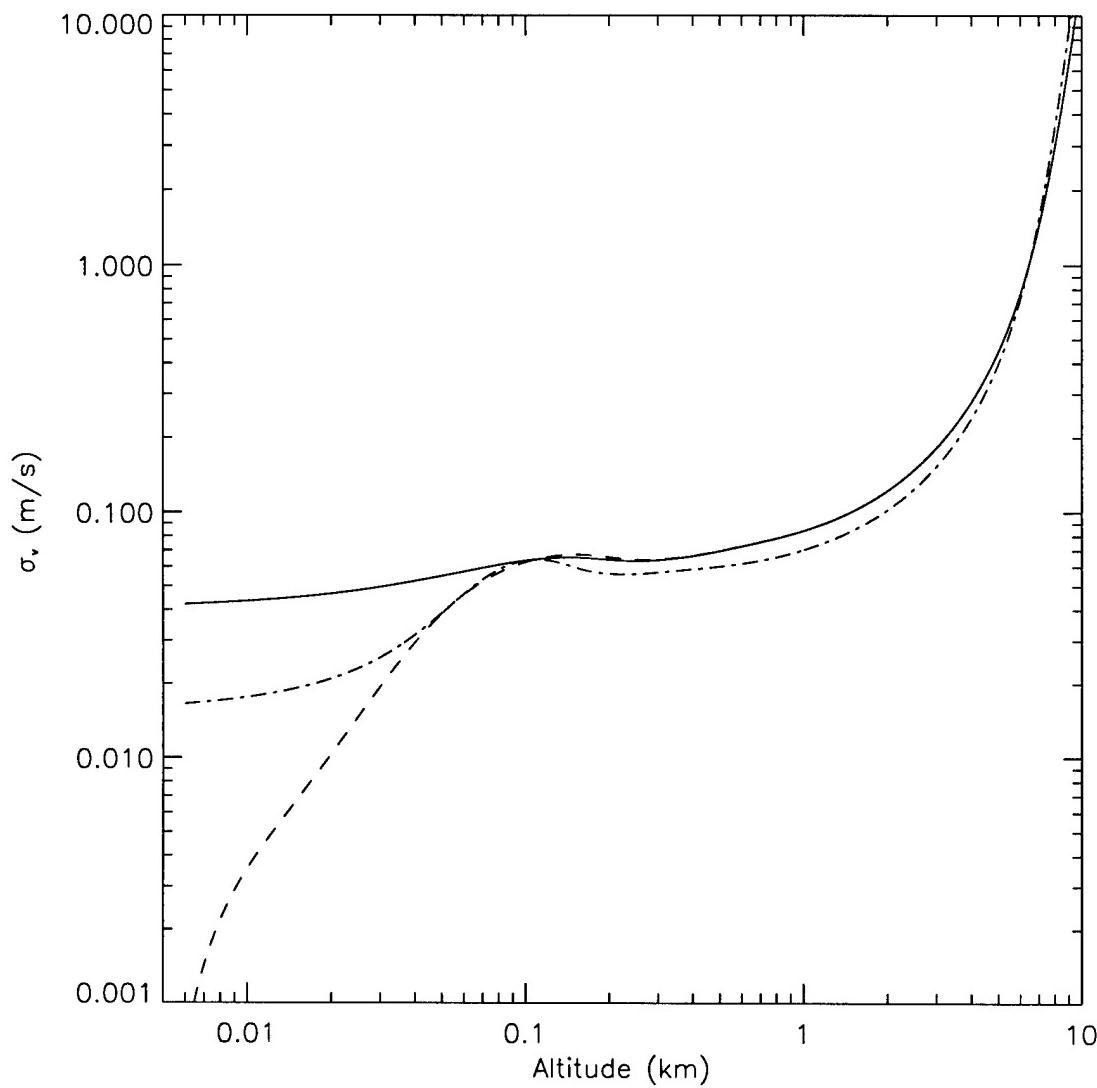
Figure 4-39: Case 1 (solid), Case 2 (dashed), and Case 3 (dash-dot) lower bound on the standard deviation of the velocity (in the Doppler sensitive direction) estimation error for $\sigma_L = 3$ mm and pulsed system (s-polarization).

$$\underline{\Lambda}_{v_p} = \frac{\sigma_\omega^2}{k^2}\left(A^T A\right)^{-1} \tag{4.73}$$

where σ_ω^2 (rad$^2 \cdot$sec^{-2}) is the variance of the frequency estimation error,

$$A = \frac{1}{\sqrt{R_T^2 + B^2}}\begin{bmatrix} 0 & -B & 0 \\ \sqrt{3}\,B/2 & B/2 & 0 \\ -\sqrt{3}\,B/2 & B/2 & 0 \end{bmatrix}$$

$$-\frac{R_T + \sqrt{R_T^2 + B^2}}{R_T\sqrt{R_T^2 + B^2}}\begin{bmatrix} 1 \\ 1 \\ 1 \end{bmatrix}\begin{bmatrix} 0 & 0 & R_T \end{bmatrix}$$

$$= \frac{1}{\sqrt{R_T^2 + B^2}}\begin{bmatrix} 0 & -B & -\left(R_T + \sqrt{R_T^2 + B^2}\right) \\ \sqrt{3}\,B/2 & B/2 & -\left(R_T + \sqrt{R_T^2 + B^2}\right) \\ -\sqrt{3}\,B/2 & B/2 & -\left(R_T + \sqrt{R_T^2 + B^2}\right) \end{bmatrix}, \tag{4.74}$$

and

$$\left(A^T A\right)^{-1} = \left(R_T^2 + B^2\right)\begin{bmatrix} 2/3B^2 & 0 & 0 \\ 0 & 2/3B^2 & 0 \\ 0 & 0 & \frac{1}{3}\left[R_T + \sqrt{R_T^2 + B^2}\right]^{-2} \end{bmatrix}. \tag{4.75}$$

The square root of the diagonals of this matrix represent the error (standard deviation) multiplication introduced by inverting Eq. (3.13). The diagonals are plotted in *Figure 4-40* for the system parameters of *Table 4-3*. As expected, the ability of the system to sense the transverse velocity at high altitudes is poor.

Including the effects of geometry, the velocity error variances for each velocity component are given by

$$\sigma_{v_p^z}^2 = \frac{2\left(R_T^2 + B^2\right)}{3B^2}\frac{\sigma_\omega^2}{k^2} = \frac{2}{3}\frac{\sigma_\omega^2}{k^2 \sin^2\theta_S}, \tag{4.76}$$

$$\sigma_{v_p^y}^2 = \frac{2\left(R_T^2 + B^2\right)}{3B^2}\frac{\sigma_\omega^2}{k^2} = \frac{2}{3}\frac{\sigma_\omega^2}{k^2\sin^2\theta_S},$$ (4.77)

and

$$\sigma_{v_p^z}^2 = \frac{\left(R_T^2 + B^2\right)}{3\left(R_T + \sqrt{R_T^2 + B^2}\right)^2}\frac{\sigma_\omega^2}{k^2}$$

$$= \frac{1}{3}\frac{\sigma_\omega^2}{k^2(1 + \cos^2\theta_S + 2\cos\theta_S)}.$$ (4.78)

The lower bound on the standard deviation of the estimation errors are plotted in *Figure 4-41* for the system parameters in *Table 4-3* and Case 1 geometry. The x- and y-components of the single shot velocity estimation error bounds are less than 1 m/s for altitudes less than 1 km and the optimum beam size. As can be seen from the figure, the x- and y-component error bounds grow very rapidly with altitudes greater than about 1 km. In this region, not only is the SNR decreasing, but the geometry limits the ability of the system to sense the transverse velocity components. For the z-components, the single shot estimation error bound is less than 10 cm/sec for the optimum beam size. In this case, the geometry helps the sensitivity to the z-direction because, even at the low altitude, the system can sense the vertical velocity [see Eq. (4.78)].

This same analysis can be completed for the Case 2 geometry when estimating the vertical velocity. In this case, **A** is a scalar given by

$$\mathbf{A} = -2\cos\frac{\theta_S}{2}.$$ (4.79)
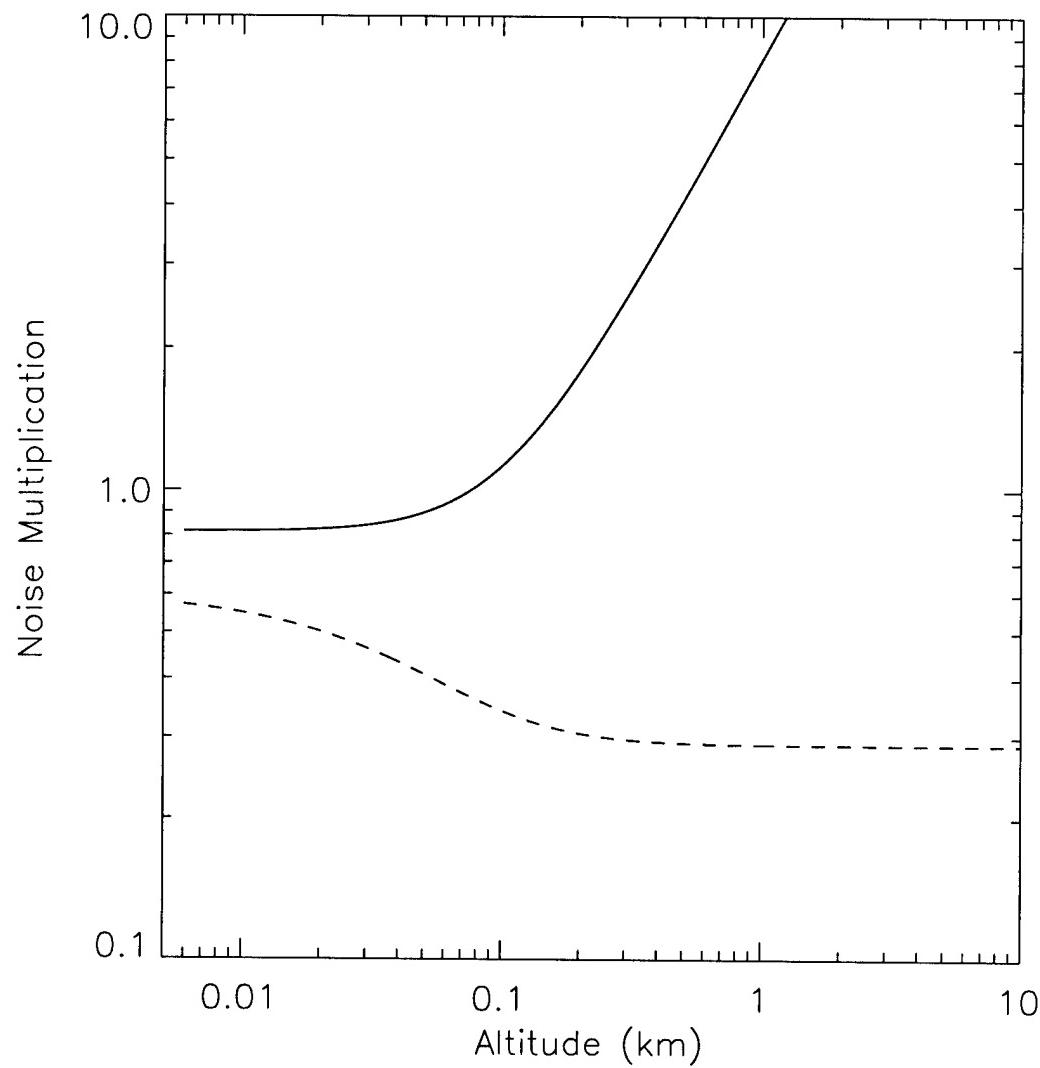
Figure 4-40: Case 1 error multiplication for *x*- and *y*-components (solid) and *z*-component (dashed).
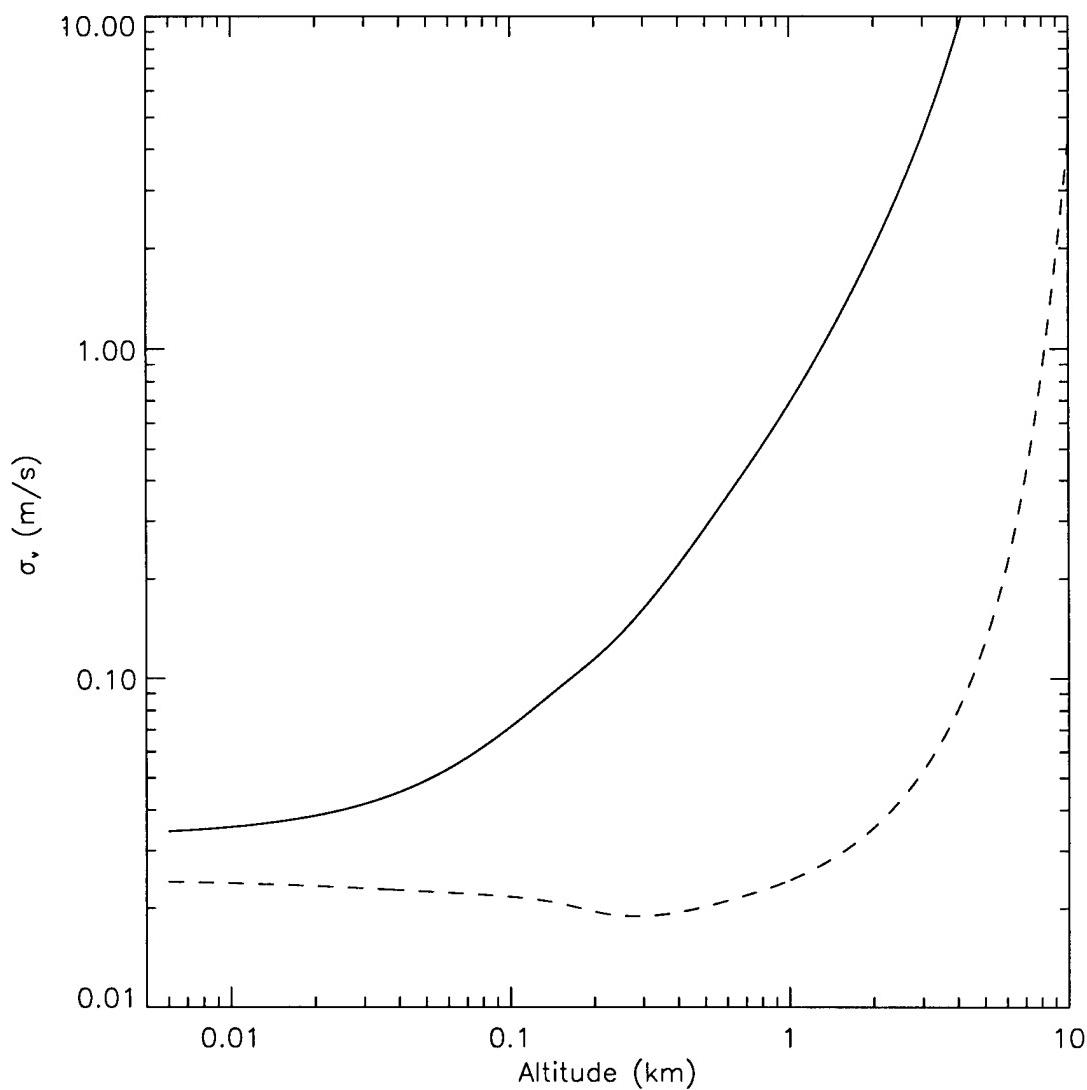
Figure 4-41: Case 1 (s-pol) standard deviation of velocity estimation errors for
$\sigma_L = 3$ mm. Solid line is x- and y-components, dashed line is z-component.

The lower bound on the estimation variance of the vertical velocity is then given by

$$\sigma_{v_p^z}^2 = \frac{\sigma_\omega^2}{2k^2 \cos^2 \frac{\theta_s}{2}}.$$

(4.80)

The lower bound on the standard deviation of the vertical velocity estimation error for Case 2 is plotted in *Figure 4-42*. From this figure, the vertical velocity estimation error is less than 10 cm·sec^{-1} out to 1 km. Even though the noise multiplication for this case [see Eq. (4.79)] is large at low altitudes, the SNR is very high in this region due to forward scattering. This gives a lower bound of estimation error that is less than 1 cm·sec^{-1} at low altitudes.

As stated at the beginning of the chapter, Case 3 was included to see the effects of increased horizontal propagation. Therefore, the velocity estimation bound is not evaluated for this case. The SNR expressions from this case would be used if a system such as that defined in Case 1 was used in a scanning configuration.
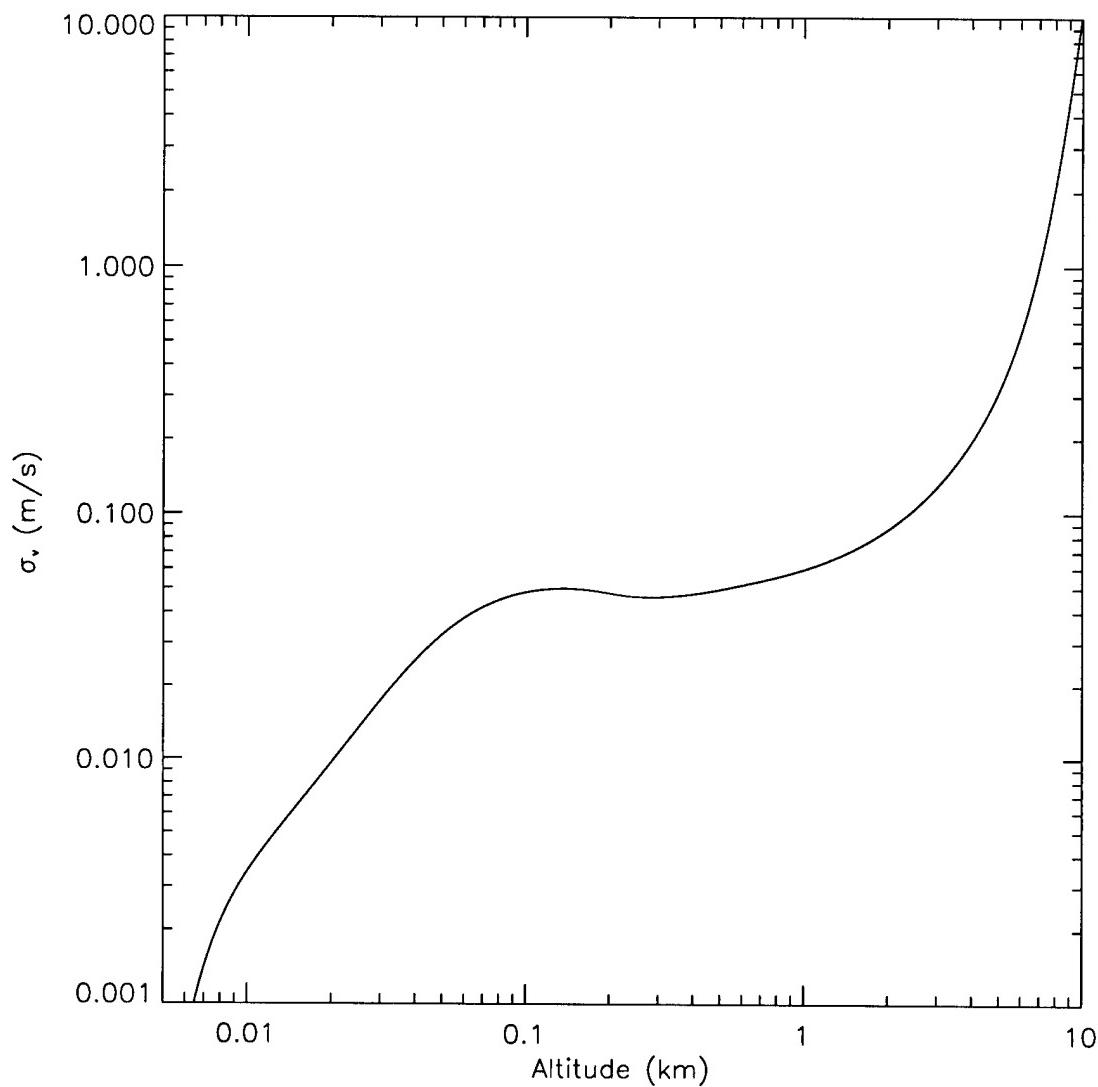
Figure 4-42: Case 2 (s-pol) standard deviation of vertical velocity estimation errors for $\sigma_L = 3$ mm.

Chapter 5

DISCUSSION AND CONCLUSIONS

This research has developed the tools required to start the design of a multistatic Doppler lidar system. The expressions derived are valid for any multistatic system, pulsed or CW, with independent propagation paths. The application of these general expressions to specific configurations indicates favorable operation for a pulsed system. There is, however, a considerable amount of research required before a multistatic system should be fielded. Applications of a multistatic coherent Doppler lidar include operational systems at airport locations, scientific investigations, system test support, and model validations.

The feasibility of a multistatic pulsed coherent Doppler lidar system for measuring winds within the boundary layer has been presented. This system will be capable of detecting high spatial resolution wind profiles for all three components of the wind velocity within the boundary layer. The multistatic configuration also decouples the vertical resolution and frequency estimation accuracy. It has also been shown that the transmitter and receiver optics are small for useful operation. In fact, the performance is improved with the use of smaller apertures. This enables the design of a compact system.

5.1 Discussion of SNR Performance

As indicated in the figures of Chapter 4, the CW SNR is orders of magnitude less than that of the pulsed SNR for the system parameters used. For this reason, the CW case does not appear feasible for the observation times desired. The pulsed case, on the other hand, has adequate SNR for frequency estimation in a single shot. In fact, the SNR is high enough that the question of whether it is better to use a system that has high peak power and low pulse repetition frequency (PRF) or lower peak power and higher PRF. This question was posed by Rye and Hardesty [40] and addressed by Frehlich and Yadlowski [54]. It turns out that in the high SNR regime, it is better to transmit many low-energy pulses instead of one pulse with the same energy. This fact should be taken in to account when designing the system.

The results also show that there is an optimum aperture size as a function of target range. The optimum aperture size for the cases evaluated is on the order of 5 mm, much smaller than might be expected. Because the apertures sizes, and thus the transmit and local oscillator beams, are small for this system, performance can be improved by making the lenses much larger than the beam sizes. If the lenses are designed to be 5 to 6 times larger than the beam sizes, the effects of truncation can be ignored and the lens sizes can be assumed infinite in extent. The effective aperture sizes are then set by the transmit and local oscillator beam sizes. The optimum beam sizes are on the order of 3 mm for all three cases. This translates to lenses that must be larger than 15 mm in order to ignore any truncation effects. The advantages of a smaller effective aperture are compact design, small scattering volume (in the near field), and minimal refractive turbulence effects.

In all of the cases examined, the effects of refractive turbulence on the SNR have been shown to be negligible for typical turbulence strengths. Only in very strong turbulence is the SNR degraded. The effects of refractive turbulence are minimized by the small effective apertures. This is because the transverse field coherence diameter of the scattered radiation due to refractive turbulence will typically be larger than the effective aperture diameter. This implies that the spatial coherence of the scattered fields will be maintained over the small effective aperture of the receiver.

A big advantage of the multistatic configuration is the high spatial resolution. Typical Doppler lidar systems are scanned to obtain information about the wind direction. This is done at the sacrifice of spatial resolution. Even when detecting only the vertical wind profile with a monostatic system, the range resolution can only be improved by using shorter pulses. This is at the expense of estimation accuracy. In the multistatic configuration, the spatial resolution is determined by an overlap volume and not tied to the pulse length of the transmit laser. For the optimum apertures, the scattering volume is less than 100 cm^3 out to an altitude of 1 km. Compare this to scattering volumes on the order of 10^5 cm^3 for the pulse length used in this analysis (250 ns). The small effective aperture sizes that can be used also contribute to reducing the scattering volume in the near field.

Comparison of theoretical SNR calculations to actual measured SNR is very difficult due to several factors: lack of well calibrated scattering targets; sensitivity to alignment of scattered and local oscillator fields; effects of speckle; and the losses due to transmission and aberrations in the receiver optics [107]. Typically the theoretical SNR

exceeds that of the measured SNR by 5–10 dB [107, 108]. Even if the pulsed SNR

values from Chapter 4 are reduced by a factor of 3–10, the results are still promising (Φ

will still be on the order of 20 coherent photoelectrons per shot).

5.2 Discussion of Frequency Estimation

The mean frequency estimation problem is greatly simplified for the multistatic

configuration. In the pulsed multistatic configuration, the return signal is due to the pulse

moving through the overlap volume. If the overlap volume is small enough, the

atmosphere will effectively be "frozen" and the return signal can be modeled as a

Rayleigh phasor. This also assumes that the spectral width of the heterodyne signal due

to the moving pulse is greater than the Doppler spread induced by velocity turbulence.

With this signal model, the first order frequency estimation problem is reduced to

detecting an M-ary signal sent over a Rayleigh channel, where M is the number of

frequency bins. In this case, maximum likelihood estimation is simplified to minimizing

the mean squared error between the return signal and the signal model.

The Cramér-Rao bound for this signal model is given in Chapter 3 and applied to

the specific cases in Chapter 4. This analysis shows that, for the cases examined, the

standard deviation of the velocity estimates is less than 1.0 m/s for all regions of interest.

This bound on performance can be realized with as few as 10 shots at an energy-to-noise

ratio (Φ) of about 10.

The reason this system is not feasible for higher altitudes becomes evident when the effects of geometry are included in the frequency estimation error. The error multiplication due to geometry becomes large for the transverse velocity at high altitudes. This is due to the fact that at high altitudes the receivers are not sensitive to the transverse velocity. In other words, at high altitudes, the multistatic configuration approaches the monostatic configuration.

As stated in Section 2.2.3, single shot estimation errors are typically on the order of 1 m·sec^{-1} when compared to anemometers, and systematic errors are on the order of 4 cm·sec^{-1}. The single shot lower bound reported in this thesis is as low as 1 cm·sec^{-1} in some cases. Certainly the system proposed in this thesis will not be able to do better than the systematic errors inherent in a coherent Doppler lidar. The lower bound on the estimation errors presented assumes a perfect system with only additive white noise corrupting the measurements. When performance bounds of this proposed system are compared to typical numbers quoted in the literature (and summarized in Chapter 2), one can see that the strength of this system is not necessarily improved velocity estimation. The strength of this design is the improved spatial resolution and ability to measure 3-demensional velocities with a single measurement.

5.3 Applications

There are several applications for remote wind profiling with lidar. The high spatial and temporal resolution wind measurements are important in describing the

evolution of mesoscale circulations associated with various atmospheric phenomena. Such phenomena include, but are not limited to, convection, density currents, and gravity wave activity. The data acquired from such measurements could be used for model validation and numerical weather forecasting. Other applications of these measurements are detection of wind shear, microbursts, and turbulence, which pose severe safety hazards to aircraft. The high resolution of this system can also be used to map wind fields over selected regions within the boundary layer and greatly enhance the visualization of flow fields, most likely in real time. These wind field maps could also be used to validate fine mesh mesoscale models.

The multistatic system could be implemented in a scanning configuration at an airport for detection of wind shear and microbursts during takeoff and landing. The same system could be used to determine the takeoff and landing intervals for large jets by sensing the wake turbulence. A bistatic configuration, set up as specified in Section 4.4.2, could be used to profile vertical wind velocities. High resolution vertical wind measurements would permit studies of turbulent motion and the evolution of convective cells in the boundary layer.

5.4 Future Research

There is still a lot of research that needs to be conducted before the system outlined in this thesis should be implemented. A more detailed analysis of the detection and estimation needs to be addressed. Specific algorithm performance as well as the

effects of using longer pulses, in which case the spectral width of the return signal is no longer determined by only the transmitted pulse temporal profile. In either case, the signal model presented in Chapter 3 would no longer be valid. Under these conditions, an evaluation of the signal covariance should be conducted. This has been done for the monostatic case [109] and should be modified for the multistatic case.

This thesis does not address the detailed design issues involved with building the system. Some issues that need to be addressed in this area are: getting the LO beam to the receivers; optical design of the transmitter and receiver; alignment; and numerical effort for real time estimates. The LO beam could be routed to the receiver via single mode optical fiber links, but frequency stability may be an issue for large baselines. The most difficult problem in the design stage may be the alignment and scanning, especially for coherent detection. The optimum location of the transmitter and receivers also needs to be addressed. Since this is an application specific optimization, it is not addressed in this research.

Other future research topics include experimental verification of the SNR expressions, simulation of the overall performance, performance of a focused system, and a closer examination of the CW case. The detailed covariance function of the scattered signal may give insight into how the CW case can be improved. Also note, that in the CW case, the statistics of the return signal are determined by the statistics of the aerosol motions within the scattering volume, which is not addressed in this thesis.

BIBLIOGRAPHY

[1]   R. M. Huffaker, A. V. Jelalian, and J. A. L. Thomson, "Laser-Doppler system for detection of aircraft trailing vortices," *Proc. IEEE*, vol. 58, pp. 322-326, 1970.

[2]   J. G. Hawley, et al., "Coherent launch-site atmospheric wind sounder: theory and experiment," *Appl. Opt.*, vol. 32, pp. 4557-4568, 1993.

[3]   S. F. Clifford, J. C. Kaimal, R. J. Lataitis, and R. G. Strauch, "Ground-based remote profiling in atmospheric studies: an overview," *Proc. IEEE*, vol. 82, pp. 313-355, 1994.

[4]   A. V. Jelalian, *Laser Radar Systems*. Norwood, MA: Artech House, 1992.

[5]   V. J. Abreu, T. L. Killeen, and P. B. Hays, "Tristatic high resolution Doppler lidar to study winds and turbulence in the troposphere," *Appl. Opt.*, vol. 20, pp. 2196-2202, 1981.

[6]   M. C. Jackson, "The geometry of bistatic radar systems," *IEE Proceedings*, vol. 133, Pt. F, pp. 604-612, 1986.

[7]   N. J. Willis, *Bistatic Radar*. Boston: Artech House, 1991.

[8]   J. Wurman, M. Randall, C. L. Frush, E. Loew, and C. L. Holloway, "Design of a bistatic dual-Doppler radar for retrieving vector winds using one transmitter and a remote low-gain passive receiver," *Proc. IEEE*, vol. 82, pp. 1861-1871, 1994.

[9]   S. Twomey, *Introduction to the Mathematics of Inversion in Remote Sensing and Indirect Measurements*. Amsterdam: North-Holland, 1977.

[10]   S. W. Henderson, C. P. Hale, J. R. Magee, M. J. Kavaya, and A. V. Huffaker, "Eye-safe coherent laser radar system at 2.1 µm using Tm,Ho:YAG lasers," *Opt. Letters*, vol. 16, pp. 773-775, 1991.

[11]   J. W. Caspers, "Bistatic and Multistatic Radar," in *Radar Handbook*, M. I. Skolnik, Ed., 1st ed. New York: McGraw-Hill, 1970, pp. 36-1-36-19.

[12]   T. D. Stevens, "Bistatic Lidar Measurements of Lower Tropospheric Aerosols," Ph.D. Thesis, Department of Electrical Engineering, The Pennsylvania State University, University Park, PA, 1996.

[13] R. M. Huffaker, "Laser Doppler detection systems for gas velocity measurement," *Appl. Opt.*, vol. 9, pp. 1026-1039, 1970.

[14] J. A. Reagan and B. M. Herman, "Bistatic lidar investigations of atmospheric aerosols," , *Proceedings of the Conference on Radar Meteorology*, vol. 14, pp. 275, 1970.

[15] R. T. Menzies, M. J. Kavaya, P. H. Flamant, and D. A. Haner, "Atmospheric aerosol backscatter measurements using a tunable coherent CO_2 lidar," *Appl. Opt.*, vol. 23, pp. 2510-2517, 1984.

[16] K. Parameswaran, K. D. Rose, and B. V. K. Murthy, "Aerosol characteristics from bistatic lidar observations," *J. Geophys. Res.*, vol. 89, pp. 2541-2552, 1984.

[17] P. C. S. Devara and P. E. Raj, "Remote sounding of aerosols in the lower atmosphere using a bistatic cw helium–neon lidar," *J. Aerosol Sci.*, vol. 20, pp. 37-44, 1989.

[18] P. C. S. Devara and P. E. Raj, "Study of atmospheric aerosols in a terrain-induced nocturnal boundary layer using bistatic lidar," *Atmos. Environ.*, vol. 25A, pp. 655-660, 1991.

[19] B. M. Welsh and C. S. Gardner, "Bistatic imaging lidar technique for upper atmospheric studies," *Appl. Opt.*, vol. 28, pp. 82-88, 1989.

[20] K. Meki, et al., "Range-resolved bistatic imaging lidar for the measurement of the lower atmosphere," *Opt. Letters*, vol. 21, pp. 1318-1320, 1996.

[21] R. T. Menzies and R. M. Hardesty, "Coherent Doppler lidar for measurements of wind fields," *Proc. IEEE*, vol. 77, pp. 449-462, 1989.

[22] J. W. Bilbro, "Atmospheric laser Doppler velocimetry: an overview," *Opt. Eng.*, vol. 19, pp. 533-542, 1980.

[23] D. L. Fried, "Optical heterodyne detection of an atmospherically distorted signal wave front," *Proc. IEEE*, vol. 55, pp. 57-67, 1967.

[24] R. F. Lutomirski and H. T. Yura, "Propagation of a finite optical beam in an inhomogeneous medium," *Appl. Opt.*, vol. 10, pp. 1652-1658, 1971.

[25] H. T. Yura, "Signal-to-noise ratio of heterodyne lidar systems in the presence of atmospheric turbulence," *Opt. Acta*, vol. 26, pp. 627-644, 1979.

[26] J. Y. Wang, "Heterodyne laser radar SNR from a diffuse target containing multiple glints," *Appl. Opt.*, vol. 21, pp. 464-476, 1982.

[27] R. Murty, "Refractive turbulence effects on truncated Gaussian beam heterodyne lidar," *Appl. Opt.*, vol. 23, pp. 2498-2502, 1984.

[28] M. S. Belen'kii, "Effect of atmospheric turbulence on heterodyne lidar performance," *Appl. Opt.*, vol. 32, pp. 5368-5372, 1993.

[29] V. A. Banakh and V. L. Mironov, "Phase approximation of the Huygens–Kirchoff method in problems of laser-beam propagation in the turbulent atmosphere," *Opt. Letters*, vol. 1, pp. 172-174, 1977.

[30] S. F. Clifford and S. M. Wandzura, "Monostatic heterodyne lidar performance: the effect of the turbulent atmosphere," *Appl. Opt.*, vol. 20, pp. 514-516, 1981.

[31] J. H. Shapiro, B. A. Capron, and R. C. Harney, "Imaging and target detection with a heterodyne-reception optical radar," *Appl. Opt.*, vol. 20, pp. 3292-3313, 1981.

[32] R. G. Frehlich and M. J. Kavaya, "Coherent laser radar performance for general atmospheric refractive turbulence," *Appl. Opt.*, vol. 30, pp. 5325-5352, 1991.

[33] R. G. Frehlich, "Effects of refractive turbulence on coherent laser radar," *Appl. Opt.*, vol. 32, pp. 2122-2139, 1993.

[34] T. R. Lawrence, et al., "A laser velocimeter for remote wind sensing," *Rev. Sci. Instr.*, vol. 43, pp. 512-518, 1972.

[35] M. J. Kavaya and P. J. M. Suni, "Continuous wave coherent laser radar: calculation of measurement location and volume," *Appl. Opt.*, vol. 30, pp. 2634-2642, 1991.

[36] J. H. Churnside and H. T. Yura, "Laser vector velocimetry: a 3-D measurement technique," *Appl. Opt.*, vol. 21, pp. 845-850, 1982.

[37] S. L. Marple, Jr., *Digital Spectral Analysis with Applications*. Englewood Cliffs, NJ: Prentice-Hall, 1987.

[38] M. H. Hayes, *Statistical Digital Signal Processing and Modeling*. New York: Wiley, 1996.

[39] B. J. Rye and R. M. Hardesty, "Discrete spectral peak estimation in incoherent backscatter heterodyne lidar. I: spectral accumulation and the Cramer-Rao lower bound," *IEEE Trans. Geosci. Rem. Sens.*, vol. 31, pp. 16-27, 1993.

[40] B. J. Rye and R. M. Hardesty, "Discrete spectral peak estimation in incoherent backscatter heterodyne lidar. II: correlogram accumulation," *IEEE Trans. Geosci. Rem. Sens.*, vol. 31, pp. 28-35, 1993.

[41] H. L. van Trees, *Detection, Estimation, and Modulation Theory, Part I.* New York: Wiley, 1968.

[42] C. W. Helstrom, *Elements of Signal Detection and Estimation.* Englewood Cliffs, NJ: Prentice-Hall, 1995.

[43] D. S. Zrnic, "Mean power estimation with a recursive filter," *IEEE Trans. Aero. Elec. Sys.*, vol. AES-13, pp. 281-289, 1977.

[44] R. G. Frehlich, "Cramer-Rao bound for Gaussian random processes and applications to radar processing of atmospheric signals," *IEEE Trans. Geosci. Rem. Sens.*, vol. 31, pp. 1123-1131, 1993.

[45] S. W. Henderson, et al., "Coherent laser radar at 2 μm using solid-state lasers," *IEEE Trans. Geosci. Rem. Sens.*, vol. 31, pp. 4-15, 1993.

[46] S. D. Mayor, et al., "Validation of NCAR 10.6-μm CO_2 Doppler lidar radial velocity measurements and comparison with a 915-Mhz profiler," *J. Atmos. Oceanic Technol.*, vol. 14, pp. 1110-1126, 1997.

[47] F. Köpp, R. L. Schwiesow, and C. Werner, "Remote measurements of boundary-layer wind profiles using a cw Doppler lidar," *J. Climate Appl. Meteorol.*, vol. 23, pp. 148-154, 1984.

[48] R. G. Frehlich, "Performance of a 2-μm coherent Doppler lidar for wind measurements," *J. Atmos. Oceanic Technol.*, vol. 11, pp. 1517-1528, 1994.

[49] P. R. Mahapatra and D. S. Zrnic, "Practical algorithms for mean velocity estimation in pulse doppler weather radars using a small number of samples," *IEEE Trans. Geosci. Rem. Sens.*, vol. GE-21, pp. 491-501, 1983.

[50] D. S. Zrnic, "Estimation of spectral moments for weather echoes," *IEEE Trans. Geosci. Electron.*, vol. GE-17, pp. 113-128, 1979.

[51] S. S. Abeysekera, "Performance of pulse-pair method of Doppler estimation," *IEEE Trans. Aero. Elec. Sys.*, vol. 34, pp. 520-531, 1998.

[52] K. S. Miller and M. M. Rochwarger, "A covariance approach to spectral moment estimation," *IEEE Trans. Info. Theory*, vol. 18, pp. 588-596, 1972.

[53] R. M. Hardesty, "Performance of discrete spectral peak frequency estimator for Doppler wind velocity measurements," *IEEE Trans. Geosci. Rem. Sens.*, vol. GE-24, pp. 777-783, 1986.

[54] R. G. Frehlich and M. J. Yadlowsky, "Performance of mean-frequency estimators for Doppler radar and lidar," *J. Atmos. Oceanic Technol.*, vol. 11, pp. 1217-1230, 1994.

[55] S. M. Kay and S. L. Marple, Jr., "Spectrum analysis–a modern perspective," *Proc. IEEE*, vol. 69, pp. 1380-1419, 1981.

[56] M. J. Levin, "Power spectrum parameter estimation," *IEEE Trans. Info. Theory*, vol. 11, pp. 100-107, 1965.

[57] P. T. May and R. G. Strauch, "An examination of wind profiler signal processing algorithms," *J. Atmos. Oceanic Technol.*, vol. 6, pp. 731-735, 1989.

[58] H. J. Landau, "Maximum entropy and maximum likelihood in spectral estimation," *IEEE Trans. Info. Theory*, vol. 44, pp. 1332-1336, 1998.

[59] B. T. Lottman and R. G. Frehlich, "Evaluation of coherent Doppler lidar velocity estimators in nonstationary regimes," *Appl. Opt.*, vol. 36, pp. 7906, 1997.

[60] B. T. Lottman and R. G. Frehlich, "Evaluation of Doppler radar velocity estimators," *Radio Sci.*, vol. 32, pp. 677-686, 1997.

[61] B. J. Rye and R. M. Hardesty, "Spectral matched filters in coherent laser radar," *J. Modern Opt.*, vol. 41, pp. 2131-2144, 1994.

[62] C. L. Korb, B. M. Gentry, and C. Y. Weng, "Edge technique: theory and application to the lidar measurement of atmospheric wind," *Appl. Opt.*, vol. 31, pp. 4202-4213, 1992.

[63] G. Benedetti-Michelangelli, F. Congeduti, and G. Fiocco, "Measurement of aerosol motion and wind velocity in the lower troposphere by Doppler optical radar," *J. Atmos. Sci.*, vol. 29, pp. 906-910, 1972.

[64] M. L. Chanin, A. Garnier, A. Hauchecorne, and J. Porteneuve, "A Doppler lidar for measuring winds in the middle atmosphere," *Geophys. Res. Lett.*, vol. 16, pp. 1273-1276, 1989.

[65] D. Rees and I. S. McDermid, "Doppler lidar atmospheric wind sensor: reevaluation of a 355-nm incoherent Doppler lidar," *Appl. Opt.*, vol. 29, pp. 4133-4144, 1990.

[66] M. Born and E. Wolf, *Principle of Optics*, 4th ed. New York: Pergamon Press, 1970.

[67] V. J. Abreu, J. E. Barnes, and P. B. Hays, "Observations of winds with an incoherent lidar detector," *Appl. Opt.*, vol. 31, pp. 4509-4514, 1992.

[68] K. W. Fischer, et al., "Visible wavelength Doppler lidar for measurement of wind and aerosol profiles during day and night," *Opt. Eng.*, vol. 34, pp. 499-511, 1995.

[69] M. J. McGill, W. R. Skinner, and T. D. Irgang, "Analysis techniques for the recovery of winds and backscatter coefficients from a multiple-channel incoherent Doppler lidar," *Appl. Opt.*, vol. 36, pp. 1253-1268, 1997.

[70] M. J. McGill, W. R. Skinner, and T. D. Irgang, "Validation of wind profiles measured with incoherent Doppler lidar," *Appl. Opt.*, vol. 36, pp. 1928-1939, 1997.

[71] M. J. McGill and W. R. Skinner, "Multiple Fabry–Perot interferometers in an incoherent Doppler lidar," *Opt. Eng.*, vol. 36, pp. 139-145, 1997.

[72] M. Fogiel, Ed., *Handbook of Mathematical, Scientific, and Engineering Formulas, Tables, Functions, Graphs, Transforms*. Piscataway, NJ: Research & Education Association, 1994.

[73] H. L. van Trees, *Detection, Estimation, and Modulation Theory, Part III*. New York: Wiley, 1971.

[74] A. Papoulis, *Probability, Random Variables, and Stochastic Processes*, 3rd ed. New York: McGraw-Hill, 1991.

[75] R. T. Menzies, "Doppler lidar atmospheric wind sensors: a comparative performance evaluation for global measurement applications from earth orbit," *Appl. Opt.*, vol. 25, pp. 2546-2553, 1986.

[76] K. M. van Vliet, "Noise limitations in solid state detectors," *Appl. Opt.*, vol. 6, pp. 1145-1169, 1967.

[77] J. Y. Wang, "Detection efficiency of coherent optical radar," *Appl. Opt.*, vol. 23, pp. 3421-3427, 1984.

[78] S. C. Cohen, "Heterodyne detection: phase front alignment, beam spot size, and detector uniformity," *Appl. Opt.*, vol. 14, pp. 1953-1959, 1975.

[79] F. G. Stremler, *Introduction to Communication Systems*, 3rd ed. New York: Addison-Wesley, 1990.

[80] A. E. Siegman, "The antenna properties of optical heterodyne receivers," *Appl. Opt.*, vol. 5, pp. 1588-1594, 1966.

[81] B. J. Rye, "Antenna parameters for incoherent backscatter heterodyne lidar," *Appl. Opt.*, vol. 18, pp. 1390-1398, 1979.

[82]   B. J. Rye, "Refractive-turbulence contribution to incoherent backscatter heterodyne lidar returns," *J. Opt. Soc. Am.*, vol. 71, pp. 687-691, 1981.

[83]   B. J. Rye, "Primary aberration contribution to incoherent backscatter heterodyne lidar returns," *Appl. Opt.*, vol. 21, pp. 839-844, 1982.

[84]   V. A. Banakh and V. L. Mironov, *Lidar in a Turbulent Atmosphere*. Dedham, MA: Artech House, 1987.

[85]   J. H. Shapiro, "Reciprocity of the turbulent atmosphere," *J. Opt. Soc. Am.*, vol. 61, pp. 492-495, 1971.

[86]   K. P. Chan, D. K. Killinger, and N. Sugimoto, "Heterodyne Doppler 1-μm lidar measurement of reduced effective telescope aperture due to atmospheric turbulence," *Appl. Opt.*, vol. 30, pp. 2617-2627, 1991.

[87]   J. L. Codona, D. B. Creamer, S. M. Flatté, R. G. Frehlich, and F. S. Henyey, "Solution for the fourth moment of waves propagating in a random media," *Radio Sci.*, vol. 21, pp. 929-948, 1986.

[88]   R. G. Frehlich, "Space-time fourth moments of waves propagating in random media," *Radio Sci.*, vol. 22, pp. 481-490, 1987.

[89]   V. I. Tatarski, "The effects of the turbulent atmosphere on wave propagation," in *ISPT Catalog 5319*. Springfield, VA: NTIS, 1972.

[90]   R. G. Frehlich, "Intensity covariance of a point source in a random medium with a Kolmogorov spectrum and an inner scale of turbulence," *J. Opt. Soc. Am. A*, vol. 73, pp. 360-366, 1987.

[91]   S. M. Wandzura, "Meaning of quadratic structure functions," *J. Opt. Soc. Am.*, vol. 70, pp. 745-747, 1980.

[92]   L. D. Dickson, "Characteristics of a propagating Gaussian beam," *Appl. Opt.*, vol. 9, pp. 1854-1861, 1970.

[93]   H. C. van de Hulst, *Light Scattering by Small Particles*. New York: Wiley, 1957.

[94]   C. F. Bohren and D. R. Huffman, *Absorption and Scattering of Light by Small Particles*. New York: Wiley, 1983.

[95]   P. Koepke and M. Hess, "Scattering functions of tropospheric aerosols: the effects of nonspherical particles," *Appl. Opt.*, vol. 27, pp. 2422-2430, 1988.

[96]   A. Ishimaru, *Electromagnetic Wave propagation, Radiation, and Scattering*. Englewood Cliffs, NJ: Prentice-Hall, 1991.

[97] I. S. Gradshteyn and I. M. Ryzhik, *Table of Integrals, Series, and Products*, 5th ed. San Diego: Academic Press, 1994.

[98] M. Abramowitz and I. A. Stegun, Eds., *Handbook of Mathematical Functions*. New York: Dover, 1970.

[99] W. J. Wiscombe, "Mie Scattering Calculations: Advances in Technique and Fast, Vector-Speed Computer Codes," Technical Note Rep. NCAR/TN-140+STR (ftp://climate.gsfc.nasa.gov/pub/wiscombe/Single_Scatt/Mie_Code/), NCAR, Boulder, CO, 1979.

[100] W. J. Wiscombe, "Improved Mie scattering algorithms," *Appl. Opt.*, vol. 19, pp. 1505-1509, 1980.

[101] E. P. Shettle and R. W. Fenn, "Models for the Aerosols of the Lower Atmosphere and the Effects of Humidity Variations on their Optical Properties," Technical Report Rep. AFGL-TR-79-0214, Air Force Geophysics Laboratory, Hanscom AFB, MA, 1979.

[102] R. M. Measures, *Laser Remote Sensing: Fundamentals and Applications*. New York: Wiley, 1984.

[103] V. Srivastava, M. A. Jarzembski, and D. A. Bowdle, "Comparison of calculated aerosol backscatter at 9.1- and 2.1-μm wavelengths," *Appl. Opt.*, vol. 31, pp. 1904-1906, 1992.

[104] E. J. McCartney, *Optics of the Atmosphere, Scattering by Molecules and Particles*. New York: Wiley, 1976.

[105] J. W. Goodman, *Statistical Optics*. New York: Wiley, 1985.

[106] R. G. Frehlich, "Conditions for optimal performance of monostatic coherent laser radar," *Opt. Letters*, vol. 15, pp. 643-645, 1990.

[107] R. Foord, R. Jones, J. M. Vaughan, and D. V. Willetts, "Precise comparison of experimental and theoretical SNRs in CO_2 laser heterodyne systems," *Appl. Opt.*, vol. 22, pp. 3787-3795, 1983.

[108] J. H. Shapiro, "Precise comparison of experimental and theoretical SNRs in CO2 laser heterodyne systems: comments," *Appl. Opt.*, vol. 24, pp. 1245-1247, 1985.

[109] R. G. Frehlich, "Coherent Doppler lidar signal covariance including wind shear and wind turbulence," *Appl. Opt.*, vol. 33, pp. 6472-6481, 1994.

Appendix A

DERIVATION OF COHERENT RESPONSIVITY AND SIGNAL-TO-NOISE RATIO

This appendix shows the detailed integration involved in deriving the expressions for coherent responsivity [Eq. (4.20)] and signal-to-noise ratio (SNR) [Eq. (4.24)]. The coherent responsivity density is given by [see Eq. (3.99)]

$$c(\mathbf{p}, z_t, z_r) = \lambda^2 \langle j_T(\mathbf{p}, z_t) \rangle \langle j_{BPLO}(\mathbf{p}, z_r) \rangle, \tag{A.1}$$

where we have assumed independent paths and no spatial variation with respect to time in e_T and e_{BPLO}. Transforming all coordinates to the target referenced coordinate system using

$$
\begin{aligned}
x_t &= x_p & x_r &= x_p \cos\theta_S + z_p \sin\theta_S \\
y_t &= y_p & y_r &= y_p \\
z_t &= z_p + R_T & z_r &= -x_p \sin\theta_S + z_p \cos\theta_S + R_R,
\end{aligned}
\tag{A.2}
$$

Eq. (A.1) becomes

$$
\begin{aligned}
c(x_p, y_p, z_p) = \lambda^2 \Big\langle & j_T(x_p, y_p, z_p + R_T) \Big\rangle \\
& \times \Big\langle j_{BPLO}(x_p \cos\theta_S + z_p \sin\theta_S, y_p, -x_p \sin\theta_S + z_p \cos\theta_S + R_R) \Big\rangle.
\end{aligned}
\tag{A.3}
$$

From Eqs. (3.81), (3.93), and (3.100), with the assumptions of deterministic transmitter and LO fields and infinite uniform detector, the random irradiance profile of the normalized transmitter field at the target becomes

$$\langle j_T(\mathbf{p}, R_T)\rangle = \int\limits_{-\infty}^{\infty}\int\limits_{-\infty}^{\infty} e_T(\mathbf{u}_1,0)e_T^*(\mathbf{u}_2,0)\langle G(\mathbf{p};\mathbf{u}_1,R_T)G^*(\mathbf{p};\mathbf{u}_2,R_T)\rangle d^2\mathbf{u}_1 d^2\mathbf{u}_2 . \quad \text{(A.4)}$$

Using the second moment of the Green's function given in Eqs. (3.115) and (3.117), the second moment Green's function in Eq. (A.4) can be written as

$$\langle G(\mathbf{p};\mathbf{u}_1,R_T)G^*(\mathbf{p};\mathbf{u}_2,R_T)\rangle = \frac{k^2}{(2\pi R_T)^2}\exp\left\{\frac{ik}{2R_T}\left[(\mathbf{p}-\mathbf{u}_1)^2-(\mathbf{p}-\mathbf{u}_2)^2\right]\right\}$$
$$\times\exp\left[-\frac{1}{2}\left(\frac{\mathbf{u}_1-\mathbf{u}_2}{\rho_o(R_T)}\right)^2\right], \quad \text{(A.5)}$$

where a square law structure function is assumed and ρ_o is defined in Eq. (3.118). Using the Gaussian field definitions of Chapter 4 and Eq. (A.5), Eq. (A.4) becomes

$$\langle j_T(\mathbf{p}, R_T)\rangle = \frac{k^2}{(2\pi R_T)^2\pi\sigma_L^2}\int\limits_{-\infty}^{\infty}\int\limits_{-\infty}^{\infty}\exp\left[-\frac{u_1^2}{2\sigma_{TE}^2}-\frac{iku_1^2}{2F_{TE}}\right]$$
$$\times\ \exp\left[-\frac{u_2^2}{2\sigma_{TE}^2}-\frac{iku_2^2}{2F_{TE}}\right]$$
$$\times\ \exp\left\{\frac{ik}{2R_T}\left[(\mathbf{p}-\mathbf{u}_1)^2-(\mathbf{p}-\mathbf{u}_2)^2\right]\right\}$$
$$\times\ \exp\left[-\frac{1}{2}\left(\frac{\mathbf{u}_1-\mathbf{u}_2}{\rho_o(R_T)}\right)\right]d^2\mathbf{u}_1 d^2\mathbf{u}_2. \quad \text{(A.6)}$$

Some algebra and a substitution to sum and difference coordinates, i.e.

$$\mu = \frac{\mathbf{u}_1+\mathbf{u}_2}{2} \qquad \beta = \mathbf{u}_1-\mathbf{u}_2 , \quad \text{(A.7)}$$

gives

$$\left\langle j_T(\mathbf{p}, R_T) \right\rangle = \frac{k^2}{(2\pi R_T)^2 \pi \sigma_L^2} \int\limits_{-\infty}^{\infty}\int\limits_{-\infty}^{\infty} \exp\left[-\frac{1}{\sigma_{TE}^2}\mu^2 + i\left(\frac{k}{R_T} - \frac{k}{F_{TE}}\right)\beta\cdot\mu \right]d^2\mu$$

$$\times \quad \exp\left[\left(-\frac{1}{4\sigma_{TE}^2} - \frac{1}{2\rho_o^2(R_T)}\right)\beta^2 - \frac{ik}{R_T}\mathbf{p}\cdot\beta \right]d^2\beta. \tag{A.8}$$

Now,

$$\int\limits_{-\infty}^{\infty} \exp\left[-ax^2 + i\,\mathbf{b}\cdot\mathbf{x}\right]d^2\mathbf{x} = \frac{\pi}{a}\exp\left[-\frac{b^2}{4a}\right], \tag{A.9}$$

which gives

$$\left\langle j_T(\mathbf{p}, R_T) \right\rangle = \frac{k^2\sigma_{TE}^2}{(2\pi R_T)^2 \sigma_L^2}\int\limits_{-\infty}^{\infty}\exp\left\{ \left[\frac{k^2\sigma_{TE}^2}{4}\left(\frac{1}{R_T}-\frac{1}{F_{TE}}\right)^2 \right.\right.$$

$$\left.\left. + \frac{1}{4\sigma_{TE}^2} + \frac{1}{2\rho_o^2(R_T)}\right]\beta^2 - \frac{ik}{R_T}\mathbf{p}\cdot\beta\right\}d^2\beta$$

$$= \frac{\sigma_{TE}^2}{\pi\sigma_L^2}\left[\sigma_{TE}^2\left(1-\frac{R_T}{F_{TE}}\right)^2 + \frac{R_T^2}{\sigma_{TE}^2 k^2} + \frac{2R_T^2}{k^2\rho_o^2(R_T)}\right]^{-1}$$

$$\times \exp\left\{ -\frac{p^2}{\left[\sigma_{TE}^2\left(1-\frac{R_T}{F_{TE}}\right)^2 + \frac{R_T^2}{\sigma_{TE}^2 k^2} + \frac{2R_T^2}{k^2\rho_o^2(R_T)}\right]}\right\}, \tag{A.10}$$

and Eq. (4.16) results. The expression for the normalized irradiance of the imagined BPLO field is obtained in a similar manner and is not included here.

Again, transforming to target referenced coordinates yields

$$j_T(x_p, y_p, z_p + R_T) = \left| e_T(x_p, y_p, z_p + R_T)\right|^2, \tag{A.11}$$

and

$$\left\langle j_{BPLO}(x_p \cos\theta_S + z_p \sin\theta_S, y_p, -x_p \sin\theta_S + z_p \cos\theta_S + R_R)\right\rangle$$

$$= \frac{T_R}{\pi\sigma_{BR}^2(x_p, z_p, R_R)} \exp\left[-\frac{\left(x_p \cos\theta_S + z_p \sin\theta_S\right)^2 + y_p^2}{\sigma_{BR}^2(x_p, z_p, R_R)}\right], \qquad (A.12)$$

where

$$\sigma_{BT}^2[z_p + R_T] = \sigma_{TE}^2\left(1 - \frac{z_p + R_T}{F_{TE}}\right)^2 + \frac{\left(z_p + R_T\right)^2}{k^2\sigma_{TE}^2}, \qquad (A.13)$$

and

$$\sigma_{BR}^2(x_p, z_p, R_R) = \sigma_{RE}^2\left(1 - \frac{-x_p \sin\theta_S + z_p \cos\theta_S + R_R}{F_{RE}}\right)^2$$

$$+ \frac{\left(-x_p \sin\theta_S + z_p \cos\theta_S + R_R\right)^2}{k^2\sigma_{RE}^2}, \qquad (A.14)$$

and we have ignored the turbulence effects as they will not change the analytic

expressions of this appendix.

The coherent responsivity is obtained by integrating Eq. (A.3) over **p**,

$$C(z_p, R_R, R_T) = \int_{-\infty}^{\infty} c(x_p, y_p, z_p) dx_p dy_p . \qquad (A.15)$$

The limits of integration are extended to infinity because we are using untruncated

Gaussian functions to describe the average normalized transmitter and imagined BPLO

irradiances. Substituting Eqs. (A.11) – (A.13) into Eq. (A.15), and using the zero order

approximation for σ_{BT} and σ_{BR}, the coherent responsivity becomes

$$C(z_p, R_R, R_T) = \frac{\lambda^2 T_T T_R}{\pi^2 \sigma_{BTo}^2 \sigma_{BRo}^2} \int\limits_{-\infty}^{\infty}\int\limits_{-\infty}^{\infty} \exp\left[-\frac{x_p^2 + y_p^2}{\sigma_{BTo}^2}\right]$$

$$\times \exp\left[-\frac{\left(x_p \cos\theta_S + y_p \sin\theta_S\right)^2 + y_p^2}{\sigma_{BRo}^2}\right] dx_p dy_p$$

$$= \frac{\lambda^2 T_T T_R}{\pi^2 \sigma_{BTo}^2 \sigma_{BRo}^2} \exp\left[-z_p^2 \frac{\sin^2\theta_S}{\sigma_{BRo}^2}\right] \int\limits_{-\infty}^{\infty} \exp\left[-y_p^2\left(\frac{1}{\sigma_{BT0}^2} + \frac{1}{\sigma_{BRo}^2}\right)\right] dy_p$$

$$\times \int\limits_{-\infty}^{\infty} \exp\left[-x_p^2\left(\frac{1}{\sigma_{BTo}^2} + \frac{\cos^2\theta_S}{\sigma_{BRo}^2}\right) - x_p\left(\frac{2z_p \cos\theta_S \sin\theta_S}{\sigma_{BRo}^2}\right)\right] dx_p, \qquad \text{(A.16)}$$

where the dependence of σ_{BTo} and σ_{BRo} on R_T and R_R, respectively, is understood. These integrals can be found in the integral tables [see ref. 97, page 355], repeated here for convenience

$$\int\limits_{-\infty}^{\infty} \exp[-p^2 x^2 \pm qx] dx = \exp\left[\frac{q^2}{4p^2}\right]\frac{\sqrt{\pi}}{|p|}. \qquad \text{(A.17)}$$

Performing the integration yields

$$C(z_p, R_R, R_T) = \frac{\lambda^2 T_T T_R \sqrt{\pi}}{\pi^2 \sigma_{BTo} \sigma_{BRo} \sqrt{\sigma_{BRo}^2 + \sigma_{BTo}^2}} \exp\left[-z_p^2 \frac{\sin^2\theta_S}{\sigma_{BRo}^2}\right]$$

$$\times \int\limits_{-\infty}^{\infty} \exp\left[-x_p^2\left(\frac{1}{\sigma_{BTo}^2} + \frac{\cos^2\theta_S}{\sigma_{BRo}^2}\right) - x_p\left(\frac{2z_p \cos\theta_S \sin\theta_S}{\sigma_{BRo}^2}\right)\right] dx_p$$

$$= \frac{\lambda^2 T_T T_R}{\pi\sqrt{\left[\sigma_{BRo}^2 + \sigma_{BTo}^2\right]\left[\sigma_{BRo}^2 + \sigma_{BTo}^2 \cos^2\theta_S\right]}} \exp\left[-z_p^2 \frac{\sin^2\theta_S}{\sigma_{BRo}^2}\right]$$

$$\times \exp\left[\frac{z_p^2 \cos^2\theta_S \sin^2\theta_S}{\sigma_{BR0}^4} \frac{\sigma_{BTo}^2 \sigma_{BRo}^2}{\sigma_{BRo}^2 + \sigma_{BTo}^2 \cos^2\theta_S}\right]$$

$$= \frac{\lambda^2 T_T T_R}{\pi \sqrt{\left[\sigma_{BRo}^2 + \sigma_{BTo}^2\right]\left[\sigma_{BRo}^2 + \sigma_{BTo}^2 \cos^2 \theta_S\right]}}$$

$$\times \exp\left[-z_p^2 \left(\frac{\sin^2 \theta_S}{\sigma_{BRo}^2} - \frac{\sigma_{BTo}^2 \cos^2 \theta_S \sin^2 \theta_S}{\sigma_{BRo}^2 \left(\sigma_{BRo}^2 + \sigma_{BTo}^2 \cos^2 \theta_S\right)}\right)\right]$$

$$= \frac{\lambda^2 T_T T_R}{\pi \sqrt{\left[\sigma_{BRo}^2 + \sigma_{BTo}^2\right]\left[\sigma_{BRo}^2 + \sigma_{BTo}^2 \cos^2 \theta_S\right]}}$$

$$\times \exp\left[-z_p^2 \left(\frac{\sin^2 \theta_S}{\sigma_{BRo}^2 + \sigma_{BTo}^2 \cos^2 \theta_S}\right)\right]. \tag{A.18}$$

Inserting Eq. (A.18) into (3.108), and assuming a Gaussian temporal profile as in

Eq. (4.22), the SNR becomes

$$\mathrm{SNR}(t) = \frac{U_L \eta_Q K^2 \beta(R_T, \theta_S)}{h\nu B_w \tau_p \sqrt{\pi}} \frac{\lambda^2 T_T T_R}{\pi \sqrt{\left[\sigma_{BRo}^2 + \sigma_{BTo}^2\right]\left[\sigma_{BRo}^2 + \sigma_{BTo}^2 \cos^2 \theta_S\right]}}$$

$$\times \int_{-R_T}^{\infty} \exp\left[-\frac{\left(t - \frac{z_p + R_T}{c}\right)^2}{\tau_p^2}\right] \exp\left[-z_p^2 \left(\frac{\sin^2 \theta_S}{\sigma_{BRo}^2 + \sigma_{BTo}^2 \cos^2 \theta_S}\right)\right] dz_p$$

$$= \frac{U_L \eta_Q K^2 \lambda^2 T_T T_R \beta(R_T, \theta_S) \exp\left[-\frac{\left(t - R_T/c\right)^2}{\tau_p^2}\right]}{h\nu B_w \tau_p \pi \sqrt{\pi \left[\sigma_{BRo}^2 + \sigma_{BTo}^2\right]\left[\sigma_{BRo}^2 + \sigma_{BTo}^2 \cos^2 \theta_S\right]}}$$

$$\times \int_{-R_T}^{\infty} \exp\left[-z_p^2 \left(\frac{\sin^2 \theta_S}{\sigma_{BRo}^2 + \sigma_{BTo}^2 \cos^2 \theta_S} + \frac{1}{\tau_p^2 c^2}\right)\right]$$

$$\times \exp\left[z_p \frac{2}{\tau_p^2 c}\left(t - \frac{R_T}{c}\right)\right] dz_p, \tag{A.19}$$

where we have assumed that K and β do not change over the scattering volume. If we

assume that R_T is large enough such that the extent of the scattering volume in the

z_p-direction is small compared to R_T, we can extend the lower limit of Eq. (A.19) to $-\infty$

with very little error. Using Eq. (A.17) the SNR becomes

$$
\text{SNR}(t) = \frac{U_L \eta_Q K^2 \lambda^2 T_T T_R \beta(R_T, \theta_S) \exp\left[-\dfrac{(t - R_T/c)^2}{\tau_p^2}\right]}{\pi h \nu B_w \tau_p \sqrt{\left[\sigma_{BRo}^2 + \sigma_{BTo}^2\right]\left[\sigma_{BRo}^2 + \sigma_{BTo}^2 \cos^2\theta_S\right]}}
$$

$$
\times \left[\frac{\sin^2\theta_S}{\sigma_{BRo}^2 + \sigma_{BTo}^2 \cos^2\theta_S} + \frac{1}{\tau_p^2 c^2}\right]^{-\frac{1}{2}}
$$

$$
\times \exp\left[\frac{\dfrac{4}{\tau_p^4 c^2}\left(t - \dfrac{R_T}{c}\right)^2}{4\left(\dfrac{\sin^2\theta_S}{\sigma_{BRo}^2 + \sigma_{BTo}^2 \cos^2\theta_S} + \dfrac{1}{\tau_p^2 c^2}\right)}\right]
$$

$$
= \frac{U_L \eta_Q K^2 \lambda^2 T_T T_R \beta(R_T, \theta_S)}{\pi h \nu B_w \tau_p \sqrt{\left[\sigma_{BRo}^2 + \sigma_{BTo}^2\right]\left[\sigma_{BRo}^2 + \sigma_{BTo}^2 \cos^2\theta_S\right]}}
$$

$$
\times \exp\left[-\frac{(t - R_T/c)^2}{\tau_p^2}\left(1 - \frac{\sigma_{BRo}^2 + \sigma_{BTo}^2 \cos^2\theta_S}{\tau_p^2 c^2 \sin^2\theta_S + \sigma_{BRo}^2 + \sigma_{BTo}^2 \cos^2\theta_S}\right)\right]
$$

$$
\times \left[\frac{\tau_p^2 c^2 \sin^2\theta_S + \sigma_{BRo}^2 + \sigma_{BTo}^2 \cos^2\theta_S}{\tau_p^2 c^2\left(\sigma_{BRo}^2 + \sigma_{BTo}^2 \cos^2\theta_S\right)}\right]^{-\frac{1}{2}}
$$

$$
= \frac{U_L \eta_Q K^2 \lambda^3 T_T T_R \beta(R_T, \theta_S)}{\pi h B_w \sqrt{\left[\sigma_{BRo}^2 + \sigma_{BTo}^2\right]\left[\tau_p^2 c^2 \sin^2\theta_S + \sigma_{BRo}^2 + \sigma_{BTo}^2 \cos^2\theta_S\right]}}
$$

$$
\times \exp\left[-\frac{(t - R_T/c)^2}{\tau_p^2}\left(1 - \frac{\sigma_{BRo}^2 + \sigma_{BTo}^2 \cos^2\theta_S}{\tau_p^2 c^2 \sin^2\theta_S + \sigma_{BRo}^2 + \sigma_{BTo}^2 \cos^2\theta_S}\right)\right], \quad \text{(A.20)}
$$

and Eq. (4.24) results.

Appendix B

LIST OF SYMBOLS

This appendix gives a list of the symbols used in the analysis portion of the thesis. In the case that a symbol is used for more than one parameter, the context in which it used will make the meaning obvious.

Symbol (units, if applicable)	Description
A	mapping between Doppler shift and velocity; estimanda
B (m)	baseline separation $= \sqrt{b_x^2 + b_y^2 + b_z^2}$
$B(\mathbf{q}_1, \mathbf{q}_2, \mathbf{p}_1, \mathbf{p}_2)$ $(\text{m}^{-4} \cdot \text{sr}^{-1})$	target scattering function
$B_n(\mathbf{r}, s, z)$	correlation of refractive index fluctuations
B_w (Hz)	system bandwidth
BPLO	back propagated local oscillator
$C(R, t)$	coherent responsivity
$C_n^2 (z)$ $(\text{m}^{-2/3})$	refractive index structure constant
CRLB	Cramer-Rao lower bound
$D(R, t)$	direct responsivity
$D'(\mathbf{x}, z)$ (m^{-1})	structure function density
$E_{BPLO,L,LO,T,S,R}$ $(\text{W}^{1/2} \cdot \text{m}^{-1})$	scalar field amplitude for BPLO, laser, local oscillator, transmitted backscattered and received field
$E_{r,t}$ (J)	received and transmitted signal energy
$F_{L,LO,R,R,RE,TE}$ (m)	focal length of laser, local oscillator, receiver lens, transmitter lens, effective receiver, effective transmitter
F	SNR reduction factor
$\tilde{F}(j\omega)$	Fourier transform of complex envelope

G_D	detector amplifier gain
$G(\mathbf{p}; \mathbf{u}, R)$ (m^{-2})	Green's function for propagation through random media
$G^f(\mathbf{p}; \mathbf{u}, R)$ (m^{-2})	Green's function for propagation through free space
$I(t)$ (A)	total detector current
$I_{dc,S}$ (A)	detector direct current and backscattered signal current
$\underline{\mathbf{J}}$	Fisher information matrix
J_{ij}	elements of the Fisher information matrix
$J_{T,\text{BPLO}}(\mathbf{p}, R)$ (W·m^{-1})	target irradiance of transmitter and BPLO
$K(R)$	one-way irradiance extinction
$\tilde{K}_{\tilde{w}}(t, u)$	covariance function of white noise process
L (m)	distance from receiver aperture to detector
$\tilde{L}(\tau, \omega)$	sufficient statistic for estimation of τ and ω
LO	local oscillator
M	samples in range gate
$M_{\text{BPLO,LO},S,T}(\mathbf{x}_1, \mathbf{x}_2, z, t)$ (W·m^{-2})	mutual coherence function for BPLO, LO, backscattered and transmitted fields
N (W)	total noise power $|n_k|^2 = B_w \cdot N_0$; number of detectors (unitless)
$N(r)$ (m^{-3})	number density of aerosols per unit volume
$N(\sigma_S; \mathbf{p}, R)$ (m^{-5}·sr)	number density of aerosols per unit volume per unit σ_S
N_0 (J)	spectral noise level
$N_z(z)$ (m^{-3})	vertical profile of number density of aerosols per unit volume
$P_{D,L,\text{LO},\text{LOD},T}$ (W)	power of direct detection, laser, LO, LO on the detector, and transmitter
$P_n^m(\mu)$	associated Legendre function
$R_{T,R}$ (m)	range from transmitter and receiver
R (m)	general range
S (W)	signal power $|s_k|^2$
$S_{1,2}(\mu)$	complex scattering amplitudes for s- and p-polarization
SNR	signal-to-noise ratio $S \div N$
T_g (sec)	measure of the time duration of the observation interval

T_S (sec)	sampling interval
$T_{T,R}$	power truncation of laser by transmitter aperture and of BPLO by receiver aperture
U_L (J)	pulse energy of laser
V (m^3)	effective scattering volume
$V(\mathbf{p}_1, \mathbf{q}_1)$ (m^{-2}·sr$^{-\frac{1}{2}}$)	target scattering coefficient
$W_{R,T}(\mathbf{x})$	field transmittance for receiver and transmitter aperture
$Y(\kappa)$ (m^2)	Fourier transform of the detector quantum efficiency $\eta_Q(\mathbf{w})$
a_n, b_n	complex Mie coefficients
$\tilde{b}$	complex amplitude of the return signal
(b_x, b_y, b_z)	coordinates of receiver with respect to fixed coordinate system (centered at transmitter)
c (m·sec^{-1})	speed of light
$c(\mathbf{p}, R, t)$ (m^{-2})	coherent responsivity density
$d(\mathbf{p}, R, t)$ (m^{-2})	direct responsivity density
$e = 1.602 \times 10^{-19}$ (C)	electronic charge
$e_{\mathrm{BPLO},L,LO,T}(\mathbf{x}, R, t)$ (m^{-2})	normalized fields for BPLO, laser, LO, and transmitter fields
$\tilde{f}(t)$ (sec$^{-\frac{1}{2}}$)	complex envelope of transmitted signal
$g(t)$	time dependence of SNR
$h = 6.626 \times 10^{-34}$ (J·sec)	Planck's constant
$h_n^{(1)}(\rho)$	spherical Hankel function
$i_{N,S}(t)$ (A)	noise and signal current fluctuations
$i_{\perp,\parallel}(\mu)$	scattered intensities per unit irradiance for s- and p-polarization
$j_n(\rho)$	spherical Bessel function
$j_{\mathrm{BPLO},R,T}(\mathbf{x}, R, t)$ (m^{-2})	irradiance of normalized fields for BPLO, incoherent receiver, and transmitter
k (rad·m^{-1})	wavenumber $= 2\pi/\lambda$
$\mathbf{k}_{L,sc}$ (rad·m^{-1})	laser and scattered wave propagation vector
m	particle complex index of refraction

$m_{\mathrm{BPLO},S,T}(\mathbf{x}_1, \mathbf{x}_2, z, t)$ (m^{-2})	mutual coherence function of normalized fields for the BPLO, backscattered field, and transmitter field
$n(t)$ (W$^{\frac{1}{2}}$)	noise signal
$\tilde{n}(t)$ (W$^{\frac{1}{2}}$)	complex amplitude of noise signal
$\tilde{n}(\tau,\omega)$ (J$^{\frac{1}{2}}$)	crosscorrelation of white noise and time shifted (by τ) version of the transmitted signal complex envelope
$n(\mathbf{x}, z)$	refractive index fluctuations
(p_x, p_y, p_z) (m)	coordinates of target with respect to fixed coordinate system (centered at transmitter)
$\mathbf{p}, \mathbf{q}$ (m)	target transverse coordinates
r (m)	particle radius
$r(t)$ (W$^{\frac{1}{2}}$)	return signal with noise
$\tilde{r}(t)$ (W$^{\frac{1}{2}}$)	complex amplitude of return signal with noise
$s_r(t)$ (W$^{\frac{1}{2}}$)	return signal without noise
$\tilde{s}(t)$ (W$^{\frac{1}{2}}$)	complex amplitude of return signal without noise
t (sec)	time
t_c (sec)	coherence (correlation) time
$\overline{t^2}$ (sec^2)	mean square duration of transmitted signal
$\mathbf{u}$ (m)	transmitter transverse coordinate
$\mathbf{v}$ (m)	receiver transverse coordinate
$\mathbf{v}_p$ (m·sec^{-1})	velocity vector of particle $= v_p^x \hat{x} + v_p^y \hat{y} + v_p^z \hat{z}$
$v_p^{x,y,z}$ (m·sec^{-1})	x-, y-, and z-component of particle velocity
w (Hz)	spectral width of return signal
$\tilde{w}(t)$ (W$^{\frac{1}{2}}$)	complex amplitude of white noise signal
$\mathbf{w}$ (m)	detector transverse coordinate
x	size parameter $= k \cdot r$
(x, y, z) (m)	point in fixed coordinate system centered at transmitter
(x', y', z') (m)	point in fixed coordinate system centered at receiver
$(x_{n,t,r,p}, y_{n,t,r,p}, z_{n,t,r,p})$ (m)	point in north, transmitter, receiver, and target referenced coordinate system

$\hat{x}, \hat{y}, \hat{z}$	unit vectors
$\mathbf{x}$ (m)	general transverse coordinate
z (m)	general propagation distance
Δ	parameter used to determine difference between pulsed and CW versions of σ^2_{eff}
ΔR (m)	range resolution
Δv (m·sec^{-1})	velocity resolution
$\Lambda(\tau, \omega)$	likelihood function for τ and ω
$\underline{\mathbf{\Lambda}}_{v_p, \varepsilon}$	covariance matrix of velocity estimate, estimation errors
Φ	coherent photoelectrons
$\Phi_n(\mathbf{\kappa}, \kappa_z)$ (m^3)	spatial spectrum of the refractive index fluctuations
$\Psi_{D,S,T}(\mathbf{x}, z, t)$ (W$^{1/2}$·m^{-1})	total detector field, backscattered field, and transmitted field
$\alpha(z)$ (m^{-1})	linear extinction coefficient
β (m^{-1}·sr^{-1})	aerosol scattering coefficient
$\delta(t)$	temporal delta function
$\delta(\mathbf{p})$ (m^{-2})	2-d vector delta function
ε	deviation of received temporal profile from transmitted temporal profile
$\eta_{Q,H}$	quantum and heterodyne efficiency
$\theta_{nt, nr}$	transmitter and receiver elevation angle measured clockwise with respect to north referenced coordinate system
$\theta_{t, r}$	transmitter and receiver spherical coordinate elevation angle
θ_S	bistatic angle $= \theta_{nt} - \theta_{nr}$
$\theta(\tau, \omega)$	squared magnitude of ambiguity function
$\mathbf{\kappa}$ (m^{-1})	spatial wavenumber vector
λ (m)	wavelength
μ	cosine of scattering angle
ν (Hz)	frequency of the optical field
$\xi_n(\rho), \psi_n(\rho)$	Riccati-Bessel functions
$\pi_n(\mu), \tau_n(\mu)$	angular eigenfunctions

$\rho_o(R)$ (m)	transverse field coherence length
σ^{opt} (m)	optimum aperture size
σ_b	standard deviation of $\tilde{b}$
$\sigma_{BR,BT,L,LO,R,RE,T,TE}$ (m)	Gaussian width of the BPLO beam, transmitter beam, laser, LO, receiver lens, effective receiver, transmitter lens, effective transmitter
$\sigma_{BRo,BTo}$ (m)	zero order term in Gaussian width of BPLO beam and transmitter beam
$\hat{\sigma}_{BR,BT}$ (m)	Gaussian width of the BPLO beam and transmitter beam without refractive turbulence effects
σ_{eff}^2 (m^2)	effective transverse scattering area
$\sigma_{f,\omega}$ (Hz, rad·sec^{-1})	standard deviation of frequency estimate
σ_S (m^2)	backscatter cross section for a point scatterer
$\sigma_{\tau,\omega}^2$ (sec^2, rad^2·sec^{-2})	lower bound on error variance of τ estimate and ω estimate
σ_v (m·sec^{-1})	standard deviation of velocity distribution
$\sigma_{v_{x,y,z}^p}^2$ (m^2·sec^{-2})	velocity error variance for the x-, y-, and z-components of particle velocity
τ (sec)	time delay
τ_p (sec)	pulse length
$\hat{\tau}$ (sec)	maximum likelihood estimate of τ
$\phi_{t,r}$	transmitter and receiver spherical coordinate azimuth angles
$\phi(\tau, \omega)$	ambiguity function
ω (rad·sec^{-1})	radian frequency
$\omega_{c,LO,D}$ (rad·sec^{-1})	radian frequency of carrier, LO, and Doppler shift
$\overline{\omega}$ (rad·sec^{-1})	mean frequency of transmitted complex envelope
$\overline{\omega^2}$ (rad^2·sec^{-2})	mean square bandwidth of transmitted signal
$\hat{\omega}$ (rad·sec^{-1})	maximum likelihood estimate of ω
$\overline{\omega t}$ (rad)	measure of frequency modulation of transmitted complex envelope

VITA

Eric Parker Magee, Capt. USAF, received a Bachelor of Science degree in Engineering from Grove City College, Grove City, Pennsylvania, in May 1987. Upon graduation, he was commissioned as a lieutenant in the United States Air Force. After being ordered to active duty in January 1988, he was assigned as an avionics engineer with the Avionics Engineering Directorate, Aeronautical Systems Division, Air Force Systems Command, Wright Patterson Base, Ohio. In March 1993 he received a Master of Science degree in Electrical Engineering at the Air Force Institute of Technology, Wright-Patterson Air Force Base, Ohio. He was then assigned to the Phillips Laboratory, Kirtland AFB, New Mexico where he was involved in laser remote sensing research. Capt. Magee was then selected to attend graduate school for a Doctor of Philosophy in Electrical Engineering. Upon graduation, he will be assigned as an Assistant Professor of Electrical Engineering at the Air Force Institute of Technology.

Captain Magee has publications in the areas of optical propagation through turbulent atmosphere, laser imaging of satellite objects, and remote sensing of wind velocities. He is a member of Eta Kappa Nu International Honor Society for Electrical Engineers, Tau Beta Pi National Engineering Honor Society and Phi Kappa Phi National Academic Honor Society.